Segmentation and 3D Reconstruction of Structures Represented in Images: Applications in Medical Images

Zhen Ma

July of 2012

Segmentation and 3D Reconstruction of Structures Represented in Images: Applications in Medical Images

Dissertation submitted in fulfillment of the requirements for the degree of Doctor in Biomedical Engineering by the Faculdade de Engenharia da Universidade do Porto

Zhen Ma

Master of Science from the Beihang University (2007)
Bachelor of Science from the Inner Mongolia University (2004)

Supervisor

João Manuel Ribeiro da Silva Tavares
Associate Professor of the Mechanical Engineering Department
Faculdade de Engenharia da Universidade do Porto

Co-supervisor

Renato Manuel Natal Jorge
Associate Professor of the Mechanical Engineering Department
Faculdade de Engenharia da Universidade do Porto

July of 2012

ACKNOWLEDGEMENT

A good PhD supervisor not only teaches you how to carry out researches, but also helps you to further discover your life; I am very lucky because my supervisors are the persons of this kind. I would like to thank Prof. João Manuel Tavares and Prof. Renato Natal Jorge for their precious guidance in the past years. Without them, my thesis cannot be accomplished, and I would not have had the wonderful experiences in Portugal. It is truly a pleasure to have them as my supervisors.

I want to show my appreciations to my parents Zuomin Ma and Luying Wang and my wife Huiying Ji. They are always encouraging me with whatever I decide to do and be at my side whenever I am facing challenges. They are the spirits in my life that have been supporting me to pursue this degree.

A word of thanks goes to all my colleagues and friends in FEUP, with whom I have shared my memorable times and from whom I got a lot of helps during my daily lives. I am pleased to meet them and have them as my friends.

SUMMARY

Pelvic floor disorders include a series of conditions related with the organs and muscles in the pelvic cavity. The high prevalence of these conditions has severely influenced the patients' social and physical lives and need to be treated urgently. With the modern imaging facilities, the dynamic responses of the pelvic structures can be visualized and measured, which helps to better understand the mechanism of pelvic cavity and establish an objective basis for the clinical diagnoses. However, as the images are acquired from the cross-sectional planes, the obtained information is neither continuous nor intuitive. In order to perform further analysis, such as biomechanical simulation and quantitative analysis, the images are required to be computational processed and analyzed properly; segmentation and 3D reconstruction are among the primary issues to be addressed.

This project focused on image processing and analysis algorithms, especially the segmentation and 3D reconstruction of structures on axial magnetic resonance images of female pelvic cavity. Hence, in the first step, the segmentation algorithms were reviewed and classified based on the segmentation clues; their applications to segment the pelvic structures were discussed. Given the complex anatomy and imaging backgrounds of the pelvic cavity, the deformable models were seen as promising techniques to be used for the segmentation due to their flexibility and low computational complexity. Hence, a coupling deformable model was proposed to segment three pelvic organs: bladder, vagina, and rectum, which are frequently involved in the pelvic conditions. The different imaging appearances of the organs and the shape estimates of the vagina and rectum are incorporated into a novel level set framework, so that the moving contours are coupled with each other, and the three organs can be segmented simultaneously.

Then, with the boundaries, i.e. the contours, of pelvic organs identified, a shape guided deformable model was proposed to segment the levator ani muscle. In the developed solution, an influence field is formed using the posterior parts of the rectum to mimic the forces from the organs to the levator ani muscles, and this field is incorporated into the Chan-Vese model to handle over expansions that can be caused by the partial volume effect.

As the diagnosis of many urological conditions needs measurements that are related with the bladder wall, two algorithms were proposed to segment the inner and

outer boundaries of this muscular layer. Given that the urine, bladder wall, and perivesical fat have distinct imaging appearances on the T2-weighted MR images, a modified geodesic active contour was proposed to segment the inner boundary of the bladder wall, which can handle the intensity variations inside the bladder lumen. Then, a vector field is formed and used to assist the segmentation of the outer bladder wall; the proposed field can prevent overlapping between the inner and outer boundaries and infer the shape of the boundary when the appearance of the bladder wall is blurred.

For the 3D reconstruction, a level set based algorithm was proposed to reconstruct the urinary bladder using the cross-sectional boundaries from multiple views. Influence of each boundary to the reconstruction is evaluated according to its reliability; and the surface is required to approach the positions defined by these boundaries following its weighted distances. The proposed algorithm provides a flexible method to solve the discrepancies from different view planes, and can obtain a reliable bladder surface with more geometric details than the one built from a single spatial view.

All the proposed algorithms were illustrated and tested using representative image data; and the results were analyzed both qualitatively and quantitatively. Case studies were performed to test the effectiveness of the developed algorithms and verify the aspects that should be improved.

Key words: Female pelvic cavity, Segmentation, 3D Reconstruction, Level set method, Prior shape knowledge, Pelvic organs, Levator ani muscle.

SUMÁRIO

Distúrbios do pavimento pélvico incluem várias patologias relacionadas com os órgãos e músculos da cavidade pélvica. A elevada prevalência destes distúrbios influencia severamente a qualidade de vida dos pacientes e devem ser tratados com toda a urgência. Com as facilidades modernas de imagiologia médica, as respostas dinâmicas das estruturas pélvicas podem ser visualizados e quantificadas, o que ajuda a perceber melhor os mecanismos envolvidos e estabelecer bases objetivas para diagnósticos clínicos mais eficientes. No entanto, como as imagens são adquiridas usualmente de acordo com planos de corte transversais, as informações obtidas nas mesmas não são contínuas nem intuitivas. Assim, para realizar análises mais rigorosas e robustas, por exemplo, por intermédio de simulações computacionais biomecânicas mais detalhadas e realistas e análises quantitativas mais precisas, as imagens adquiridas necessitam de ser adequadamente processadas e analisadas computacionalmente, com destaque para as operações de segmentação e reconstrução 3D das estruturas presentes nas mesmas imagens. Assim, este projeto centrou-se em algoritmos de processamento e análise de imagem médica, especialmente focado na segmentação e reconstrução 3D de estruturas em imagens de ressonância magnética axial da cavidade pélvica feminina.

Numa primeira etapa, os algoritmos de segmentação de imagem foram analisados e classificados de acordo com os seus princípios, e as suas aplicações no segmento de estruturas da cavidade pélvica feminina foram avaliadas e discutidas. Dada a complexidade da anatomia e do fundo das imagens tradicionalmente adquiridas da cavidade pélvica, os modelos deformáveis revelaram-se técnicas promissoras para utilizar na segmentação, essencialmente devido à sua flexibilidade e reduzida complexidade computacional.

Um método de segmentação baseado em três modelos deformáveis acoplados foi proposto para segmentar simultaneamente três dos órgãos pélvicos frequentemente considerados na análise de patologias pélvicas: bexiga, vagina, e reto. A aparência dos diferentes órgãos nas imagens e as formas previstas para a vagina e o reto foram integradas no método proposto, de modo que os contornos se deslocam acoplados de forma a segmentar os três órgãos em simultâneo.

Posteriorment, com os limites de órgãos pélvicos determinados, isto é, os seus contornos, um novo modelo deformável foi proposto para segmentar o músculo

Levator ani. Para guiar o modelo deformável proposto para a estrutura a segmentar, é criado um campo de influência usando as partes posteriores do reto para gerar forças de guiamento a partir dos órgãos previamente segmentados para o músculo *Levator ani*, sendo este campo incorporado no modelo de Chan-vese de modo que a expansão ao longo do processo de segmentação seja robusta ao efeito de volume parcial.

Como o diagnóstico de várias patologias urológicas é frequentemente baseado em medidas relacionadas com a parede da bexiga, dois algoritmos foram propostos para segmentar as fronteiras interior e exterior da mesma. Dado que a urina, a parede da bexiga, e a gordura perivesical têm aparências distintas nas imagens de ressonância magnética em T2, um contorno ativo geodésico modificado foi proposto para segmentar a fronteira interior da parede da bexiga, que é robusto às típicas variações de intensidade verificadas no interior do lúmen da bexiga. De seguida, um campo vetorial é formado e utilizado para auxiliar a segmentação da parede exterior da bexiga. Este campo evita a sobreposição entre as fronteiras interior e exterior, e infere a forma e a aparência da parede da bexiga mesmo quando esta está mal definida nas imagens em análise.

Relativamente à reconstrução 3D, foi desenvolvido um novo algoritmo que reconstrói tridimensionalmente a bexiga usando fronteiras transversais em diferentes direções. A influência de cada fronteira na reconstrução final é avaliada de acordo com a sua fiabilidade, e a superfície aproxima-se das fronteiras envolvidas em função das suas distâncias ponderadas pela respetiva fiabilidade. O algoritmo proposto possibilita um método flexível para resolver as discrepâncias entre imagens adquiridas segundo direções distintas, de forma a obter uma superfície para a bexiga confiável e com maior detalhe geométrico do que os métodos que constrói tais superfícies a partir de uma única direcção.

Todos os algoritmos propostos foram testados e avaliados usando dados de imagens representativos, e os resultados foram analisados, tanto qualitativamente como quantitativamente. Assim, foram considerados casos de estudos para atestar a eficácia dos algoritmos desenvolvidos e verificar os aspetos a melhorar.

Palavras-chave: Cavidade pélvica feminina, Segmentação, Reconstrução 3D, Método de *Level Set*, Conhecimento prévio, Órgãos pélvicos, Músculo *Levator ani*.

INDEX

Part A

Thesis Report

1. Introduction

Segmentation and three-dimensional (3D) reconstruction are routine procedures to perform image analysis. In the past few decades, many algorithms were proposed to fulfill these tasks; among them, the ones for medical image processing and analysis have been intensively studied due to the urgent needs and practical impacts in this area. Compared with the common image processing and analysis, medical image processing and analysis has its concrete application backgrounds, which implies that the information used by the algorithms is not only from the image data, but also from other aspects such as a prior knowledge about the anatomy of the involved structures, the imaging environment or clinical experiences.

In this PhD project, the segmentation and 3D reconstruction of structures in female pelvic cavity were focused. The motivation to study this delicate region comes from the high prevalence of pelvic floor dysfunction. The pelvic floor dysfunction refers to a group of conditions such as pelvic organ prolapse, urinary incontinence, faecal incontinence, and other sensory and emptying abnormalities of the lower urinary and gastrointestinal tracts. It was reported that from 30 to 50% of women in Europe and the USA are currently suffering from urinary incontinence (UI); by the age of 80, 11.1% of women have undergone operations for pelvic organ prolapse or UI [1, 2]. The negative impacts of these conditions can considerably influence the patients' quality of life, and need to be treated properly. However, the pathophysiology of these conditions is still unclear, and findings from epidemiologic studies are usually inconsistent as they are not designed to investigate cause-and-effect relationships.

A thorough understanding on the functionalities of the pelvic structures is required to develop novel and less invasive therapies, and anatomical analysis is the fundamental step in this process [3]. Modern imaging facilities such as ultrasound, computed tomography (CT) and magnetic resonance imaging (MRI) play a critical role to acquire the anatomy of the pelvic cavity, and have considerably enhanced the diagnosis accuracy in practice. With these imaging devices, the pelvic structures can be visualized from different spatial directions. Nevertheless, the acquired image data can only present information from the cross-sectional planes which are neither continuous nor intuitive. In order to perform further analysis, such as biomechanical simulations and quantitative analysis, the 3D models of the involved structures should

be built; therefore, their cross-sectional boundaries on each image slice need to be properly segmented. However, due to the complex anatomy of pelvic cavity, the segmentation of the involved organs and muscles from the acquired image series is a very challenging task. Also, the manual segmentation is very time consuming (normally takes 1-2 hours), and the results can suffer from intra/inter observer errors, especially when the images are influenced by noise and partial volume effect. Therefore, effective segmentation algorithms are required to assist this process.

The pelvic structures have distinct appearances under different imaging modalities; correspondingly, the computational algorithms should be developed based on the modality and the imaging features of the involved structures. This project mainly focused on the processing of axial magnetic resonance images, as MRI is currently preferred in many diagnoses of urological and pelvic pathologies due to its superior imaging quality for soft tissues [4]; also, the cross-sectional boundaries of the pelvic structures and their spatial relationships can be well identified in the axial view planes.

Though on MR images the pelvic structures have clearer appearances than in other non-invasive modalities, the influences of noise and partial volume effect can considerably affect the performance of the segmentation algorithms. Hence, an effective algorithm should be able to carry out the segmentation under these negative factors; combining with the imaging features of the pelvic structures, proper segmentation models need to be selected and the clues for segmentation should be defined. The segmentation algorithms that have been used for medical images provide a sound base that has potentials to be used for this project. Hence, a comprehensive review and classification of the algorithms for medical image segmentation were performed, and their applications to the structures in the pelvic cavity were discussed in the initial phase of this project.

The geometric deformable models are among the most intensively studied algorithms in the past few decades [5]. By using such a model, the segmentation and reconstruction can be carried out through curve evolution; and with the level set method [6] to track the moving contours, the algorithms have low computational complexity and can naturally handle the topological changes during the movement. The key point of a geometric deformable model is the proper modeling of the curve evolution so that the final positions of the moving contours correspond to the

boundaries of the interested structures. For the segmentation and 3D reconstruction of structures in the pelvic cavity, one attractive feature of the deformable models is their flexibility to incorporate different segmentation clues and techniques. Therefore, the use of deformable models to segment and reconstruct the pelvic structures had promising perspectives; and this PhD project was devoted to explore such perspectives.

2. Main aims of the project

This PhD project was dedicated to develop algorithms under a concrete medical application background: the female pelvic cavity. Hence, the objectives defined in this project included the following ones:

- To make a review and classification on the current algorithms used for medical image segmentation; based on the features of each type, to discuss their suitable application fields and their perspectives to be used to segment structures in the pelvic cavity.
- To analyze the features of different imaging modalities and choose the suitable one for the study in the project; then, find the imaging appearances of the pelvic structures under this modality and explore the clues presented in the images that can be used for efficient segmentation.
- To develop new computational methodologies for the segmentation of structures in the pelvic cavity. The pelvic organs that are frequently involved in the pelvic floor dysfunctions were focused; also, the pelvic floor muscles that have critical functionalities to support the pelvic organs were concerned. This part was the key objective of this project.
- To test the developed algorithms using case studies and analyze the segmentation results, both qualitatively and quantitatively; to make a comparison of the novel algorithms with the existing ones and find the aspects that have been achieved successfully and the aspects that still need to be improved.
- To develop new algorithms for the 3D reconstruction of pelvic organs; the algorithm should build a reliable surface model combining the information from multiple spatial views.

3. Organization of the thesis

This thesis is composed of two main parts of contents: Part A and Part B. Part A serves as a report of the PhD project and contains three sub-sections: a description of the developed works, a summary of the contributions obtained during the project, the final conclusions and a discussion about the future work. Part B is composed of seven articles written during the project and serves to describe in detail the achievements accomplished during this project; hence, in these articles, the algorithms for segmentation and 3D reconstruction that were developed to fulfill the defined objectives are described and explained. In this part, the sequence of the articles is organized as the following:

Article 1 – Title: *A review of algorithms for medical image segmentation and their applications to the female pelvic cavity*
Authors: Ma Z, Tavares JMRS, Jorge RN, Mascarenhas T
Published in Journal: Computer Methods in Biomechanics and Biomedical Engineering, 13(2): 235-246, 2010

Article 2 – Title: *Segmentation of female pelvic organs in axial magnetic resonance images using coupled geometric deformable models*
Authors: Ma Z, Jorge RN, Mascarenhas T, Tavares JMRS
Submitted to an international journal (under review, after revision), 2011

Article 3 – Title: *A shape guided C-V model to segment the levator ani muscle in axial magnetic resonance images*
Authors: Ma Z, Jorge RN, Tavares JMRS
Published in Journal: Medical Engineering & Physics, 32(7): 766-774, 2010

Article 4 – Title: *Novel approach to segment the inner and outer boundaries of the bladder wall in T2-weighted magnetic resonance images*
Authors: Ma Z, Jorge RN, Mascarenhas T, Tavares JMRS
Published in Journal: Annals of Biomedical Engineering, 39(8):2287-2297, 2011

Article 5 – Title: *Segmentation of female pelvic cavity in axial T2-weighted MR images towards the 3D reconstruction*
Authors: Ma Z, Jorge RN, Mascarenhas T, Tavares JMRS

Published in Journal: International Journal for Numerical Methods in Biomedical Engineering, 28(6-7): 714-726, 2012

Article 6 – Title: *A comparison between segmentation algorithms for urinary bladder on T2-weighted MR images*

Authors: Ma Z, Jorge RN, Tavares JMRS

Published in Conference Proceedings: Proceedings of the III ECCOMAS thematic conference on Computational Vision and Medical Image Processing. CRC Press, Taylor & Francis, 371-376, 2011

Article 7 – Title: *A level set based algorithm to reconstruct the urinary bladder from multiple views*

Authors: Ma Z, Jorge RN, Mascarenhas T, Tavares JMRS

Submitted to an international journal (Under review), 2012

4. Brief description of the developed work

The segmentation and 3D reconstruction of structures in the pelvic cavity are very challenging tasks due to their complex anatomy. The developed works during this project mainly concern the processing and analysis of pelvic organs and muscles in axial magnetic resonance images. During the project, the following works were accomplished to fulfill the defined objectives:

- In order to find the suitable methods and techniques for the segmentation, a review on the current medical segmentation algorithms was carried out. The algorithms were classified into three categories according to their principal methodologies: the ones based on thresholds, the ones based on pattern recognition techniques, and the ones based on deformable models. Typical algorithms of each type were discussed and their main ideas, application fields, advantages and disadvantages were summarized. The possibility of applying these algorithms to segment the organs and tissues of the female pelvic cavity were also discussed, and experiments were presented to illustrate the distinct characteristics of the different algorithms. The main guidelines that should be considered to design the segmentation algorithms for the pelvic cavity were proposed. In the discussions, the algorithms based on deformable models were focused for their flexibilities to incorporate different clues and segmentation

techniques; also, the algorithms developed during this project can be classified as this type. This review is presented in the Article 1 included in Part B.

Among the pelvic structure, the levator ani muscle has considerable shape variations at different imaging positions; the appearance of this muscle on the axial magnetic resonance images is usually thin and frequently blurred, which makes the segmentation of this tissue even harder than the pelvic organs. The main functionality of the levator ani muscle is to support the pelvic organs; the status of this muscle is closely related to the status of organs it supports. Therefore, in this project, the strategy was defined to segment the pelvic organs as the first step and then use the available information to assist the segmentation of the levator ani muscle.

- The urinary bladder, vagina, and rectum are among the female pelvic organs that are frequently involved in pelvic floor dysfunctions. To segment the three organs, a coupling algorithm was proposed based on their imaging appearances on axial T2-weighted MR images. The coupling approach is composed of three geometric deformable models with each one to segment an organ. The differences between the intensity distributions of the three pelvic organs are used as the clue for segmentation; and based on the intensity statistics the moving contours compete with each other and expand until arrive at the boundaries of organs. Meanwhile, since the different layers of the vagina and rectum have distinct appearances, the moving contours may stop at the inner boundaries; in order to solve this problem, a prior shape constrain was added given the two organs do not have large shape variations in the same image series. The coupling approach can obtain the boundaries of the three organs simultaneously, and with the region-based external forces and the prior shape constraint the algorithms can well handle the influences of noise and partial volume effect. This approach is described in the Article 2 included in Part B.
- On T2-weighted MR images the levator ani muscle has a low signal intensity appearance that is different to the neighboring tissues. However, due to the partial volume effect, its boundary is frequently blurred; hence, the intensity gradient is not a reliable clue for segmentation. With the boundaries of pelvic organs, especially the one of the rectum, the segmentation can be carried out in a small region around the pelvic organs; a shape guided Chan-Vese (C-V)

model was then developed to segment this tissue. In the proposed solution, a region of interest (ROI) was defined using the positions of the pelvic organs; consequently, the segmentation becomes an easier two-phase problem in the ROI defined. The difference between the signal intensities of the levator ani muscle and the surrounding tissues was used for the segmentation. In order to handle the over-expansion of the contour caused by partial volume effect, a shape influence field is defined following the shape of the rectum to mimic the forces to the muscles imposed by the pelvic organs, which can guide the moving contour to the correct position when some parts of the boundary are distorted. A topology preserving technique was incorporated into the proposed algorithm to guarantee that the obtained boundary is a single connected curve. This algorithm is described in the Article 3 include in Part B.

The novel coupling algorithm can segment three organs together; however, since in many studies of urological and pelvic conditions, the urinary bladder needs to be segmented separately, the segmentation and 3D reconstruction of this particular pelvic organ was focused in this project.

- Diagnosis of bladder-related conditions needs critical measurements that involve the bladder wall; hence, two deformable models were proposed to handle the segmentation of this muscular layer. On T2-weighted MR images the bladder wall has a low-signal-intensity appearance that can be identified easily from the high-signal-intensity urine and perivesical fat. Compared to the outer boundary of the bladder wall, the inner boundary is easier to be segmented because there is no influence from neighboring tissues; hence, the sequence was defined to first segment the inner boundary and then the outer boundary. A region-based geodesic active contour algorithm was proposed to segment the inner boundary. The contrast between the appearances of the bladder wall and the bladder lumen was used for segmentation; following the region-based external force the moving contours can pass the regions with intensity variations and arrive at the inner boundary of the bladder wall. Then, as the bladder wall is a thin tissue, to exclude the influence of neighboring tissues, the segmentation of the outer boundary was carried out in a nearby region of the inner boundary. In order to avoid the overlapping between the inner and outer boundaries when the appearance of the bladder wall is blurred,

a shape influence field was formed and used for the segmentation, which integrates the continuity of the boundary, the similarity of the two boundaries and the minimal bladder wall thickness to infer the missing information. The outer boundary of the bladder wall can be effectively segmented using the proposed algorithm, which is described in Article 4 include in Part B.

- A common procedure for the 3D reconstruction of the urinary bladder is based on the sequential cross-sectional boundaries in an image series; and the marching cubes algorithm is a popular algorithm to do this task. However, information at the slice gap is normally recovered through interpolation, which can cause inaccuracies in the built surface model. With the modern imaging facilities, this issue can be considerably improved if the information from different view directions is combined for reconstruction, as the missing information at one spatial view can be compensated by other spatial views. Hence, a new level set based reconstruction algorithm was developed to build the 3D surface model of the bladder using cross-sectional boundaries. The segmented boundaries are classified according to their reliabilities, and their influences to the reconstruction are evaluated following the classification. The evolving surface is driven to approach the position defined by the boundaries so that its weighted distances can be minimized. The developed algorithm provides a flexible solution to handle the discrepancies from different view planes and can obtain a reliable bladder surface with more geometric details. This novel algorithm is described in Article 7 included in Part B.

The developed algorithms can achieve satisfied performances under proper conditions; however, in order to make the segmentation fully automatic, some aspects of the algorithms need to be improved. Appropriate case studies were essential to verify these aspects; by comparing with other algorithms, potential techniques for improvement can be explored, and the performance of the algorithms can be validated comprehensively. In this PhD project, two major works were performed to address these issues:

- The proposed segmentation algorithms for pelvic organs and for the levator ani muscle were tested together using axial images from MR image series. The algorithms were reviewed, and the initialization conditions were improved and discussed. The procedures of the algorithms were illustrated, and the obtained

boundaries of each pelvic structure were compared with the ground truth that was segmented manually by experienced technicians; critical indexes of the tissues were used to make the quantitative analysis of the segmentation results. The developed algorithms proved to be effective when proper initial conditions were defined, while the aspects to be improved, the issues for implementation and towards three-dimensional reconstruction were identified and discussed. This work is described in Article 5 include in Part B.

- A comparative case study was performed to test the different segmentation algorithms for the urinary bladder. The performances of four algorithms, including the two ones developed during this project, were evaluated using MR image series. The cross-sectional boundary of the urinary bladder was segmented on the axial, sagittal and coronal view plans using the four algorithms, and the obtained boundaries were compared with the ground truth which was segmented manually by experienced technicians. Three indexes were used for the quantitative analysis; with the quantitative analysis, the effectiveness of each segmentation algorithm was confirmed and the aspects that require further improvements were identified. This work is described in Article 6 included in Part B.

5. Main contributions achieved

Until the conclusion of this thesis, six papers have been submitted to peer-reviewed journals, in which four papers have already been published, and two papers are currently under review; additionally, five papers and six abstracts have been included in conference proceedings. Besides, one journal paper and four conference papers were published related to the work developed during this project.

The main contributions obtained during this PhD project can be summarized as the following:

- A comprehensive review on the current segmentation algorithms was done, which contributes a staged discussion on the effective algorithms used for medical image segmentation. In particular, the review was carried out jointly with the discussions on the segmentation of structures in the pelvic cavity - the main focus of this project. The classification adopted in the review is based on the principle ideas and techniques of each algorithm, which helps to

summarize the common features of different algorithms and explore the potential application fields of each type.

- Novel effective algorithms were developed to segment the urinary bladder, vagina, and rectum on MR images of female pelvic cavity. The coupling approach introduced the concept of local region competition to assist the segmentation of the three organs; for the vagina and rectum, the constraints from prior shape knowledge provide an efficient way to avoid the moving contours from stopping at the inner boundaries. The proposed algorithms can effectively handle the influence of noise and partial volume effect and segment the three pelvic organs simultaneously.
- A new effective deformable model was developed to segment the levator ani muscle on MR images. The functionality of the muscle and its anatomical relationship with the pelvic organs are used for segmentation. The boundary and position of the rectum are assumed as prior knowledge; and the proposed algorithm simplifies the segmentation in a local region near to the pelvic organs. A shape influence field was defined to simulate the pressures from the organs so that the deformation of the muscle can be indicated, and with this vector field, the segmentation accuracy is improved, especially when the levator ani muscle and the connective tissues have similar appearances.
- Two novel effective deformable models were proposed to handle the segmentation of the bladder wall. The developed algorithms are based on the imaging features of the bladder wall, bladder lumen and the surrounding tissues. For the inner boundary of the bladder wall, the proposed algorithm can well handle the intensity variations inside the bladder lumen and drive the contours to the correct position. For the outer boundary, the similarity of the two boundaries and the minimal thickness of the bladder wall are combined to define the shape influence field, with which the outer boundary of the bladder wall can be inferred when the bladder wall is blurred and meanwhile the two boundaries will not overlap with each other.
- Case studies were used to test the developed algorithms. The current algorithms have some aspects to be improved; meanwhile, clinical validation requires objective measures to reflect the influence of segmentation accuracy

to quantitative analysis. With the case studies addressed in this project, preliminary discussions were performed on these issues; the procedures of the proposed algorithms were illustrated and issues from segmentation to 3D reconstruction were discussed. Besides, their performances were compared with manual segmentation and other algorithms. Through the comparisons, the good aspects of the developed solutions were verified and the weak points to be improved were identified.

- A novel deformable model was developed to build the 3D shape of the urinary bladder. The proposed algorithm combines the information from multiple view planes and provides a flexible and accurate method to reconstruct the bladder. The cross-sectional boundaries are weighted according to their reliabilities; and the more reliable ones are assigned with higher confidence level and correspondingly have larger influences to the reconstruction. The proposed algorithm solved the discrepancies between boundaries from multiple spatial views by requiring the evolving surface to approach the positions defined by the boundaries with higher confidence levels. Therefore, the surface built using the novel algorithm contains more geometric details and are more accurate.

6. Conclusions and future work

Segmentation and 3D reconstruction on medical images will continue to be an intensive focus of research. This PhD project explored the computational processing and analysis of MR images of female pelvic cavity and achieved preliminary positive results. To handle the complex imaging backgrounds, effective algorithms were developed to segment and reconstruct the pelvic organs and muscles; and their performances were validated in experiments. Besides, all the referred algorithms were integrated into a new computational platform developed during this project using the Microsoft Foundation Class Library (MFC) with three open-source toolkits – OpenCV (http://opencv.org), ITK (http://www.itk.org/), and VTK (http://www.vtk.org/). The new platform provides an intuitive interface to define the parameters and initial conditions of the developed algorithms, and facilitates the analysis and comparison of results. Figure 1 shows three examples of the platform interface: to visualize DICOM image series and obtain information from the DICOM

tags, to segment the levator ani muscle, and for the 3D reconstruction of the urinary bladder.

Given the fact that the female pelvic cavity has delicate anatomy, and the shapes of pelvic structures have large variations among individuals, the segmentation and 3D reconstruction of structures on the acquired image data are very complex tasks. Although the developed algorithms have achieved successful results, there are some aspects that still need to be improved.

The common premises for the developed algorithms to obtain a satisfactory performance include that the pelvic structures do not suffer from large shape deformations, and the acquired images are not severely influenced by noise and partial volume effect. However, in some conditions the organs and muscles can have considerable changes of shapes and imaging appearances; to effectively handle these cases, the robustness of these algorithms should be enhanced, and proper improvements may be required for a specific condition. Besides, following the method described in Article 1 included in Part B, the segmentation algorithms developed in this project belong to the ones based on deformable models; hence, the automatic selection of proper parameters is an unsolved problem which is also the main obstacle to make the algorithms fully automatic. Therefore, to decrease the sensitivity to parameters and initial conditions is an objective to be addressed.

In particular, regarding the algorithms developed during this thesis, the possible future works are summarized as follows:

- To enhance the automation of the shape guided algorithm described in Article 3 of Part B. The definition of the ROI (region of interest) in the algorithm is critical for the performance of the segmentation. In Articles 3 and 5, the ROI was defined based on the boundary of the rectum and the boundaries of three pelvic organs, respectively. However, the methods used in these two articles may fail to include the muscle completely to the ROI due to the damage of the muscle in some conditions of pelvic floor dysfunction. Future work should address the more robust definition of the ROI; for examples, by incorporating a prior knowledge attained from clinical studies.

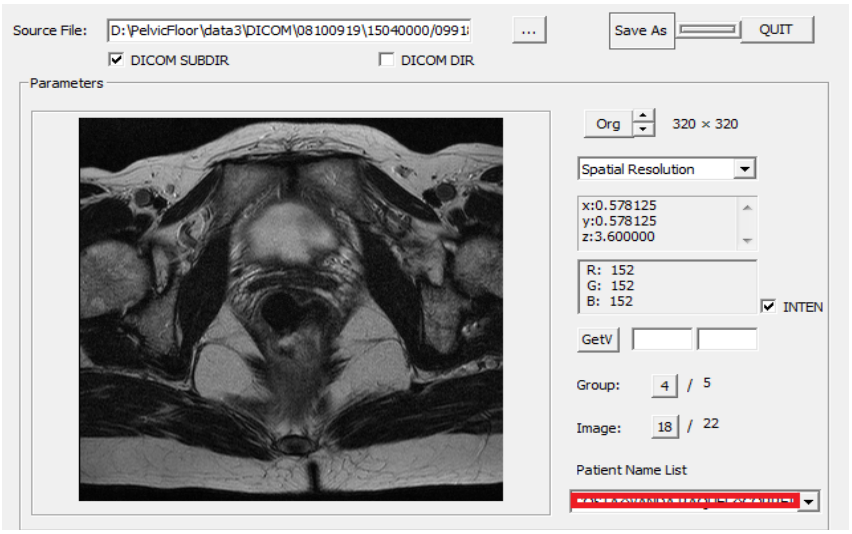

(a)

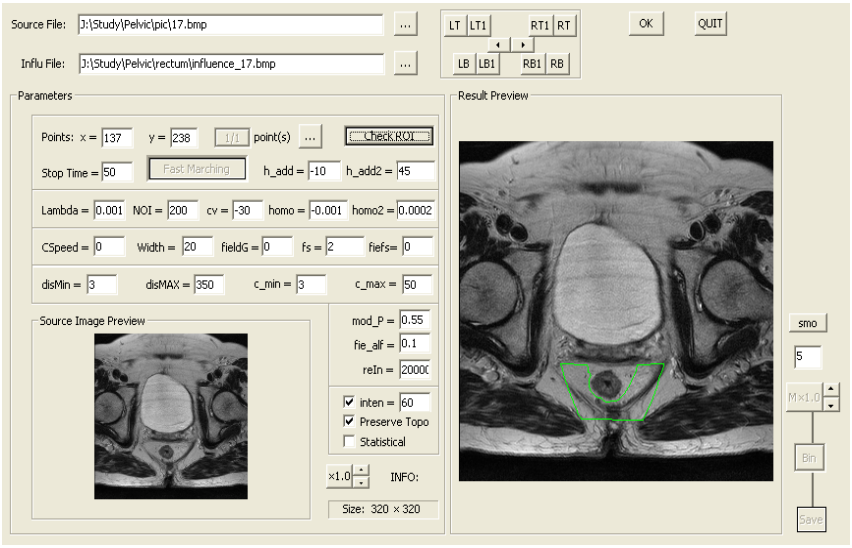

(b)

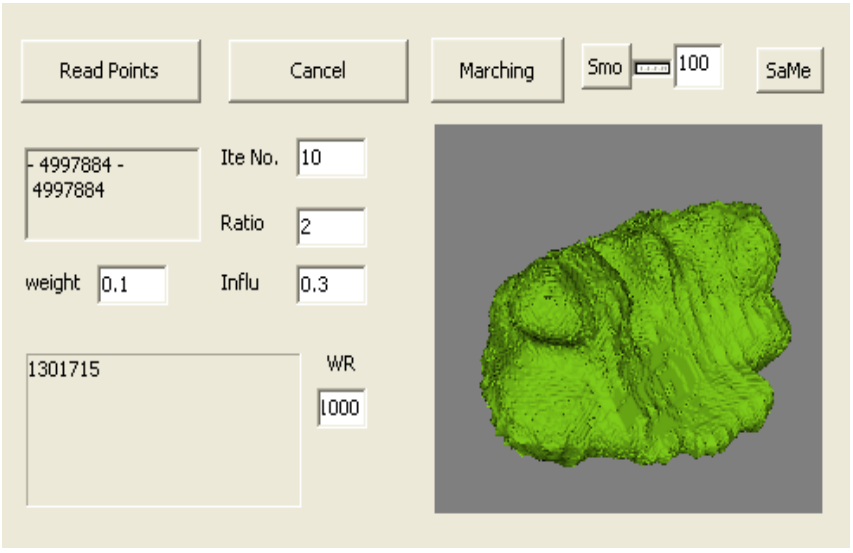

(c)

Figure 1: The interface of the new computational platform: (a) DICOM viewer – patient's name was erased by red lines for consideration of privacy; (b) to segment the levator ani muscle; (c) to reconstruct the 3D model of the urinary bladder.

- To improve the algorithms described in Article 4 of Part B. For the current algorithms, there are some cases in which the developed algorithms cannot perform successfully; for example, when a heavy intensity bias caused by the tumor happens inside the bladder lumen, the intensity statistics can be influenced considerably without manual interventions and lead to incorrect segmentation. For the outer boundary of the bladder wall, when the neighboring tissues are close to the bladder wall, manual intervention is also needed to exclude their influence in the definition of the segmentation region. The improvement should focus on how to handle the cases with the presence of a tumor or carcinoma and enhance the robustness and automation of the algorithms.
- To further study the influence of segmentation in the 3D reconstruction. The accuracy of the cross-sectional boundaries can affect the 3D models built; while currently there are few studies or works concerning their relationships or perform quantitative analysis to study the influences of the 3D models to the consequent biomechanical simulations and clinical diagnosis. Future works should consider these issues.

References

[1] Fantl JA, Newman DK, Colling J, et al. Urinary incontinence in adults: acute and chronic management. Clinical Practice Guideline, Clinical Practice Guideline, Rockville (MD): Agency for Health Care Policy and Research, Public Health Service, U.S. Department of Health and Human Services, No. 2. 1996.

[2] Olsen AL, Smith VJ, Bergstrom JO, Colling JC, Clark AL. 1997. Epidemiology of surgically managed pelvic organ prolapse and urinary incontinence. Obstet Gynecol. 89(4):501-506.

[3] Herschorn S. 2004. Female pelvic floor anatomy: the pelvic floor, supporting structures, and pelvic organs. Rev Urol. 6(Suppl 5):S2-S10.

[4] Paramasivam S, Proietto A, Puvaneswary M. 2006. Pelvic anatomy and MRI. Best Pract Res Cl Ob. 20(1):3-22.

[5] Pham DL, Xu C, Prince JL. 2000. A survey of current methods in medical image segmentation. Ann Rev Biomed Eng. 2:315-338.

[6] Osher S, Sethian J. 1988. Fronts propagating with curvature-dependent speed: algorithms based on Hamilton-Jacobi formulations. J Comput Phys. 79(1):12-49.

Part B – Article 1

A Review of Algorithms for Medical Image Segmentation and their Applications to the Female Pelvic Cavity

Zhen Ma, João Manuel R. S. Tavares, Renato Natal Jorge, T. Mascarenhas

Published in: Computer Methods in Biomechanics and Biomedical Engineering, 13(2): 235-246, 2010.

Abstract

This paper aims to make a review on the current segmentation algorithms used for medical images. Algorithms are classified according to their principal methodologies, namely the ones based on thresholds, the ones based on clustering techniques and the ones based on deformable models. The last type is focused due to the intensive investigations on the deformable models that have been done in the last few decades. Typical algorithms of each type are discussed and the main ideas, application fields, advantages and disadvantages of each type are summarized. Experiments that apply these algorithms to segment the organs and tissues of the female pelvic cavity are presented to further illustrate their distinct characteristics. In the end the main guidelines that should be considered for designing the segmentation algorithms of the pelvic cavity are proposed.

Keywords: Bioengineering, Biomedical Engineering, Medical Imaging, Image Segmentation, Algorithms Review, Deformable Models, Female Pelvic Cavity.

1. Introduction

The high resolution images produced by the modern imaging modalities offered to the medical doctors with multi-orientation views and much more details, considerably assisting the clinical diagnosis and the treatment that follows. The first step of processing these images is to segment the desired organs or structures from image series. Usually, to perform the manual segmentation medical technicians need to sketch the contours slice by slice using pointing devices such as a mouse or a trackball. This procedure is very time-consuming and the results may suffer from intra- or inter-observer variability. In the past few decades, many algorithms have been proposed to perform the computer-aided segmentation. The incorporations of modern mathematical and physical techniques have greatly enhanced the accuracy of the segmentation results.

Compared with the algorithms for common images, the ones for medical applications need more concrete background. Information used for medical image processing comes not only from image appearances but also from imaging devices and doctors' professional knowledge. A prior knowledge such as the imaging

environment or structures' biomechanical behavior can be crucial information for designing an effective algorithm, especially when the images are influenced by noises or partial volume effect (PVE) [1]. Also, the appearances of the same organs or structures may vary in different slices and imaging modalities and therefore, may need distinctive segmentation algorithms. For example, high density structures such as bones and calcified plaque have high Hounsfield Unit (HU) values in computerized tomography (CT) images and can be easily segmented, while they have much lower appreciable features in magnetic resonance (MR) images so that the segmentation algorithm may not be trivial.

In the following sections, segmentation algorithms are classified into three main types based on their principal techniques, specifically the ones based on threshold, the ones based on clustering techniques and the ones based on deformable models. The main ideas, application fields, advantages and disadvantages of each type are discussed and summarized. Each type is described using their typical algorithms and illustrated by the experimental results after these algorithms have been applied to the pelvic cavity. As it is common that multiple segmentation techniques are used in one algorithm, definite classifications of certain algorithms may not be feasible. The general principle of classification in this paper is the most appreciable characteristics of an algorithm.

The motivation for focusing on the segmentation of the pelvic cavity originates from the recognition of the high prevalence of pelvic floor (PF) disorders. PF disorders include a group of conditions that affect adult women including pelvic organ prolapse, urinary incontinence, faecal incontinence, and other sensory and emptying abnormalities of the lower urinary and gastrointestinal tracts. The fact that women will be living longer and are more often attending to PF disorders makes its study urgent, particular due to its high complexity and societal impact. It is estimated that 30 - 50% of woman in Europe and the USA are affected by urinary incontinence [2]. Over 20% of French suffer from obstructed defecation [3]. About 15% of population of New Zealand and 2.2 - 6.9% of population in the USA suffer from fecal incontinence [4-6]. The importance of developing a method to visualize, measure and model the dynamic responses of the pelvic structures has been more and more recognized. A real understanding of the pathophysiology of PF disorders is still lacking.

CT and MR images are widely used modalities for the study of the pelvic cavity. MR images are preferred in the static study of pelvic cavity because CT images usually contain large amount of noises and have low spatial resolution of soft tissues. A successful segmentation of 2D image slices can greatly facilitate the later reconstruction of a 3D pelvic cavity model which can help doctors understand its mechanism and establish a more objective basis for the diagnoses and evaluation of the clinical treatments. The complex anatomical structures and the inter-connectivity between organs make the segmentation difficult to perform. Consequently, there is no effective algorithm for this task. The segmentation of pelvic cavity includes sketching bladder, urethra, vagina, rectum, obturator internus and levator ani. In this paper we do not intend to propose a new algorithm but use this example to illustrate the different characteristics of algorithms and make a discussion on their possible applications to this area. Furthermore, the main guidelines that an effective algorithm should adopt for a successful segmentation of the pelvic cavity are indicated.

The paper is organized as follows: In Section 2, a review on the segmentation algorithms is made and their characteristics are illustrated through experiments on the pelvic cavity; In Section 3, the advantages and disadvantages of each type are summarized; In Section 4, some conclusions are summarized and the guidelines of the segmentation algorithms for the pelvic cavity are presented.

2. Algorithms Review

In this section, we present a review based on the principal features of the algorithms, classifying them into three types as referred in Section 1. Due to the fact that backgrounds and requirements for each task are different, a survey on a concrete application is beyond the scope of this paper. Instead, we extract the common features of each type, discuss and summarize their advantages and disadvantages using typical algorithms. Applications of each type to the pelvic cavity are illustrated to further state their characteristics.

2.1 Algorithms based on thresholds

Traditionally algorithms of this type make the promise that the interested structures or organs have distinctive quantifiable features such as image intensity or gradient magnitude. The procedure of segmentation is to search for the pixels whose values are within the ranges defined by the thresholds. Thresholds used in these algorithms can

be selected manually or automatically. Manual selection needs a *priori* knowledge and sometimes trial experiments to find the proper threshold values while the latter way combines the image information to get the adaptive threshold values automatically. For example, the Otsu's method [7] obtains the threshold values using image histogram. According to the information used to define the threshold values, algorithms can be further classified as edge-based ones, region-based ones and hybrid ones.

Threshold values in the edge-based algorithms are related with the edge information as structures are depicted by edge points. Wavelets transform [8] and common edge detection algorithms such as Canny edge detection [9], Sobel edge detection and Laplacian edge detection [10] belong to this type.

Algorithms try to find edge pixels meanwhile eliminate the noise influence. For example, Laplacian edge detection uses the second derivation information of the image intensity; Canny edge detector uses the gradient magnitude to find the potential edge pixels and suppresses them through non-maximal suppression and hysteresis thresholding. Since the operations of the algorithms are based on pixel intensities, the detected boundaries consist of discrete pixels and therefore may be incomplete or discontinuous. It is then necessary to apply post-processing techniques like morphological operations to connect the breaks or eliminate the holes. Due to noise influence and PVE, the edges of organs or structures in medical images are usually not clearly defined. Therefore, algorithms based on edge-detection are seldom used alone but instead as an efficiency pre-processing step for the later segmentation [11, 12].

The idea of region-based algorithms comes from the observation that quantifiable features inside a structure tend to be homogeneous. Algorithms aim to search for the pixels with similar feature values. Region growing algorithms [13-16] are typical examples of this type.

The searching rules are different among algorithms. For example, a simple approach can be to choose the initial seeds and merge their neighbor pixels whose intensities are within the threshold values until all the intensities of the surrounded pixels are outside the pre-defined ranges; the rule of seeded region growing method [13] is to expand a seed region through merging the unallocated neighbor pixels which have the smallest intensity difference between the pixel and the region; the rule of unseeded region growing algorithms is almost the same as the seeded region

growing except when the within-class variance is too large or too small regions will split or merge. To eliminate the dependence on initial seeds and make the algorithm automatic, statistical information and a *priori* knowledge can be incorporated to the algorithms [14, 17]. For example, a homogeneity criterion was introduced in [14] which made the region growing algorithms adaptive for different locations of the initial seeds and achieved success in the segmentation of CT and MR images. However, these algorithms have difficulties controlling the leakage or eliminating the influence of PVE due to their reliance on intensity.

Information used in the hybrid algorithms combines different image cues to complete the segmentation. Typical examples are watershed algorithms [18-22] which combine image intensity with gradient information and use mathematical morphology operations to do the segmentation.

In watershed algorithms, grey scale images are considered as reliefs and the gradient magnitude is treated as elevation. Watershed lines are defined to be the pixels with local maximum gradient magnitude and a region of the image is defined as the pixels enclosed by the same watershed line. The segmentation procedure is to construct watersheds during the successive flooding of the grey value relief. Due to the combination of diverse image information, watershed algorithms can achieve satisfactory results and always produce a complete segmentation of an image. Nevertheless, watershed algorithms tend to present over-segmentation problems, especially when the images are noisy or the desired objects themselves have low signal-to-noise ratio appearances. Hybrid threshold-based algorithms usually incorporate other techniques to perform the segmentation [20, 22, 23]. For example, in [20] the marker imposition technique was used to combine a *priori* knowledge and successful experiments have been reported on the segmentation of the knee cartilage and white/gray matter in MR images. In [22], shape and appearance knowledge are used to improve the performance of watershed algorithm and C-Means (CM) algorithm is used to handle the over-segmentation problems.

Figure 1(a) presents an MR axial pelvic cavity image, from which the appreciable influences of PVE can be easily seen. The segmentation results of Canny edge detector, a region growing algorithm and a watershed algorithm are illustrated in Figure 1(b)-(d). The boundaries obtained by the Canny edge detection algorithm are discontinuous due to the noises and PVE. Besides, the spatial relationships of edge points are not reflected; hence, most of the detected boundaries are incomplete or

connected wrongly. For the region growing algorithm, the boundaries of the bladder and the vagina are well segmented, but the boundary of right obturator internus leaks; the outer boundary of vagina is discontinuous and leaks in the upward direction. The watershed algorithm gives a complete segmentation of the image. However, the over segmentation can be seen in the area between bladder and vagina because there are a lot of pixels with local maximums of gradient magnitude. Moreover, the levator ani and obturator internus are merged because of the influence of PVE at the joint.

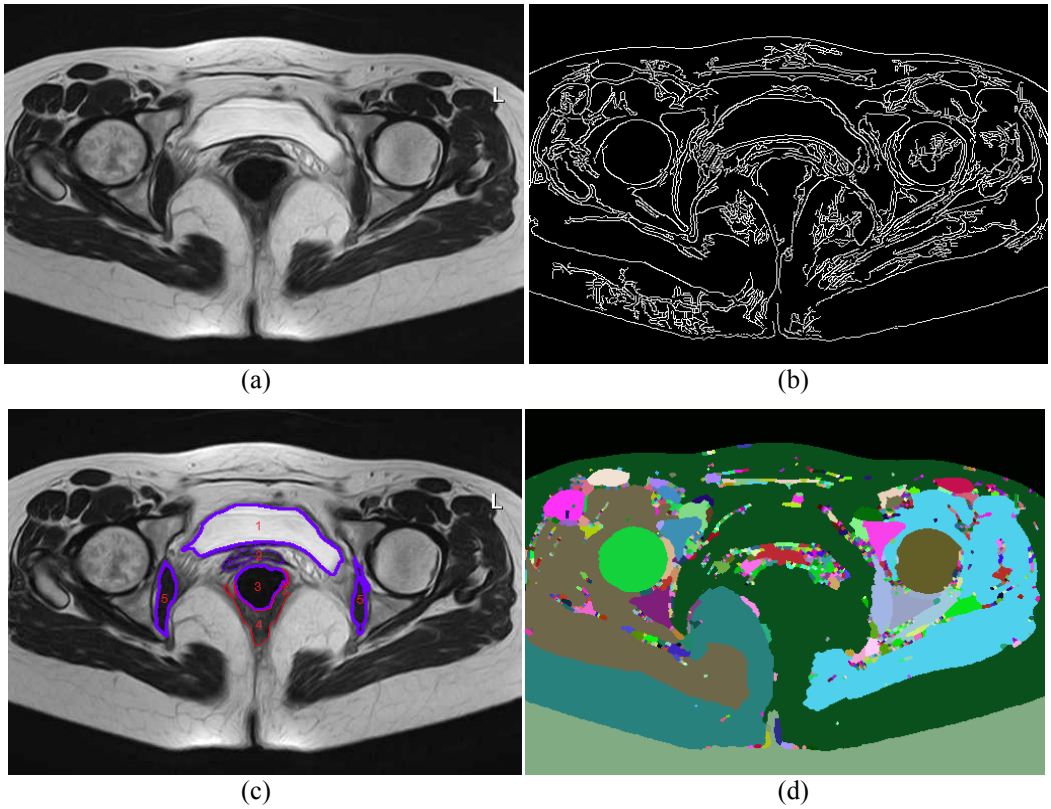

(a) (b)

(c) (d)

Figure 1: (a) MR image of the pelvic cavity; (b) Canny edge detection; (c) Region growing algorithm: 1-bladder; 2-vagina; 3-rectum; 4-levator ani; 5-obturator internus; (d) Watershed algorithm.

2.2 Algorithms based on clustering techniques

As structures in medical images can be treated as patterns, techniques from pattern recognition fields can be used to perform the segmentation. Clustering techniques are the most popular ones for medical image segmentation. In the following part, two main types of these algorithms are reviewed: supervised classification algorithms and unsupervised classification algorithms.

Frequently used supervised classification techniques include k-nearest neighbor (kNN) classifier, maximum likelihood (ML) algorithm, supervised artificial neural network (ANN), support vector machine (SVM), active shape model (ASM), and

active appearance model (AAM). A training set is needed to extract structure information but its function is different among different algorithms.

The training phase of kNN classifier is to store feature vectors and class labels of the training samples. K nearest stored points are selected for each unlabelled point according to the point distance. The classification of an unlabelled point is then 'voted on' by the selected points, for example the most frequent class label appearing in the selected points. The training step of ML algorithms is to identify the parameters used in the statistical models. ML algorithms assume that the pixel intensities are independent random variables with parameterized probability distributions, so the probability distribution of this mixture model is given by the multiplication of these parameterized probability functions. Parameters are then evaluated by maximizing the likelihood function of the mixture model. As the calculations are based on probability, ML algorithms provide a soft segmentation. Application of kNN and ML algorithms can be found in [24, 25].

Supervised ANNs are non-linear statistical data modeling tools and can be used to model complex relationships between input and output. Weights or parameters in different layers are updated after processing each sample to minimize the cost function defined by the features of structures. Typical examples of neural networks include feedforward networks and radial basis function networks [26]. SVMs are also known as maximum margin classifiers because the algorithms try to find a hyperplane to maximize the margin between two classes. SVMs can simultaneously minimize the empirical classification error and maximize the geometric margin between classes. For ANNs and SVMs information extracted from the training set provides the features of structure in the form of weights or parameters that can be used for the later segmentation. Common applications of ANNs and SVMs are on the segmentation of cardiac images and brain images inside which the organs and tissues have comparably stable shapes and anatomical structures [27-30]. Further classification and detailed procedures of ANNs and SVMs can be found in [31, 32].

Unsupervised classification techniques include CM algorithms, fuzzy C-means (FCM) algorithms, iterative self-organizing data analysis technique algorithm (ISODATA) and unsupervised neural networks. These algorithms are also called clustering algorithms. Structure features are extracted from the classified points.

CM algorithms are also called K-means algorithms, where C and K are the pre-defined number of clusters. The algorithm tries to minimize the intra-cluster variation

through iterations. The unlabelled pixels are assigned to the nearest clusters based on their distances to the cluster centroids, then the cluster centroid is updated and the pixels are re-assigned. The algorithm runs until all the pixels have fixed labels. ISODATA algorithm is similar to the CM algorithm while the number of clusters is determined by the threshold defined in the merging and splitting procedure. Applications of these algorithms are commonly used for nuclear medicine and transmission image segmentation [33-35]. For the medical applications, FCM algorithms that combine CM algorithm with fuzzy theory have more applications. The procedures of FCM algorithm are the same as the ones of CM algorithm except FCM adds weights to the calculation of cluster centroids and point distance. FCM algorithms are fuzzy clustering techniques that can provide soft segmentations in the way that instead of classifying a pixel into a fixed cluster, the algorithm calculates the membership or possibility that it belongs to each cluster. A soft segmentation is preferred as the complex imaging conditions such as shading artifacts or PVE have intrinsically determined the vagueness of the pixels. The performance of FCM algorithms can be improved through adding spatial influence in the objective function [36-40] or using kernel techniques that can better transfer non-linear problem to linear problem [41, 42]. For example, in [37] the objective function is modified by adding an influence term defined by the labels to the neighborhood pixels. In [42] the proposed algorithm used a kernel filter to map the data into a higher-dimensional feature space and then apply the FCM algorithm with strategies introduced in [38] to gain high computational efficiency. FCM algorithms are widely applied to the segmentation of MR images especially for the MR brain images [39, 43, 44].

Unsupervised neural networks are based on unsupervised learning which means the targets are the same as the inputs [45]. The weights in the classifiers are trained according to the learning rule. For example, the Hopfields neural network adopts the learning rule as winner-takes-all to decide the weights either to be 0 (zero) or 1 (one). A successful application of Hopfields neural network to CT and MR images can be seen in [46, 47]. Other popular learning rules include Hebbian learning and competitive learning [26]. A review on unsupervised neural network learning procedures and their applications can be found in [48].

There are also algorithms that use other pattern recognition techniques. For example, image registration techniques such as template matching algorithms and atlas-guided algorithms are also frequently seen to be applied for medical image

segmentation [49-51]. A *priori* knowledge is used in these algorithms to assist the segmentation. For example, in [51] prior probability knowledge of anatomic structures is incorporated into an MRI probabilistic atlas to extract the structure features, then an SVM is trained using the extracted information to finally segment the brain structures.

Figure 2 presents the segmentation result of CM algorithm and its refinement using Markov Random Field techniques [52]. Four clusters are defined with the initial mean intensities: 25, 80, 150, and 213. With these parameters CM algorithm can correctly segment the boundary of bladder. Most of the pixels that represent the same organ are clustered into one group. However, the noise influences are also appreciable. The boundaries of vagina and right obturator ani are incomplete and the boundaries of rectum and left obturator ani leaked. The refined result in Figure 2(b) gives a smoother segmentation with less noise influence because spatial constraint is incorporated using MRF techniques. Both segmentation results are very sensitive to the selection of initial number of groups and their mean intensity values.

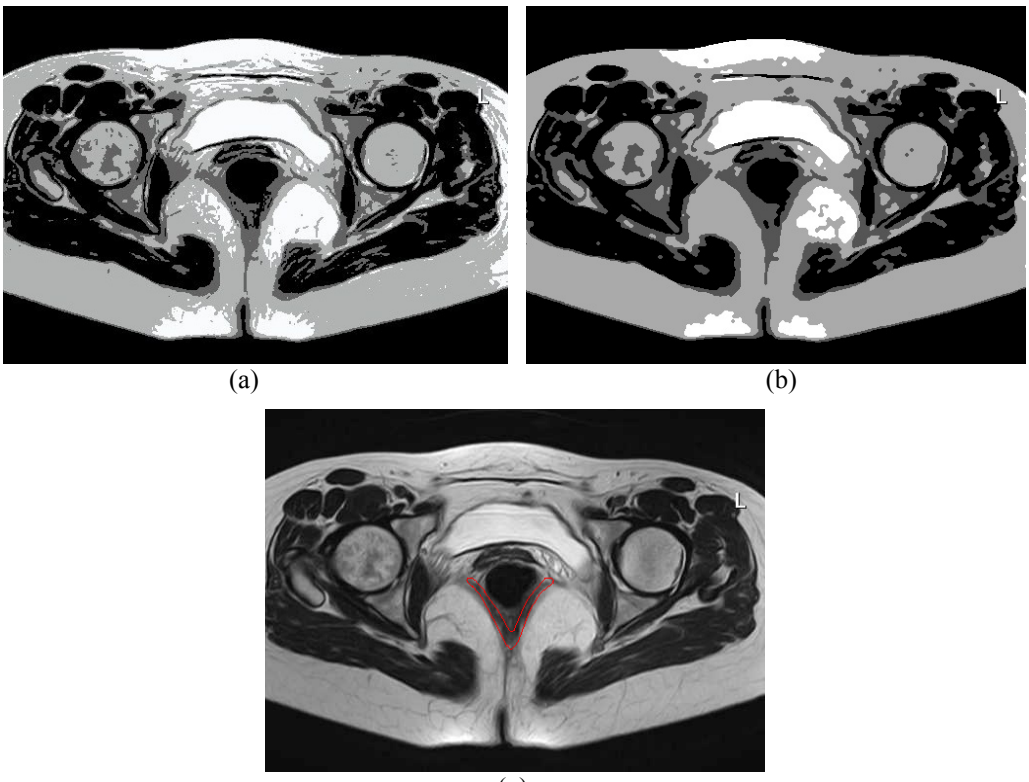

(a) (b)

(c)

Figure 2: (a) C-means algorithm (number of groups: 4; initial mean values of intensity: 25, 80, 150, 213); (b) Refined by MRF; (c) Manual segmentation of levator ani muscles.

Algorithms based on clustering techniques can be applied to segment the levator ani muscles. A successful segmentation of levator ani muscles is critical for the later

3D reconstruction of pelvic cavity. The muscles should have a presumed anatomy if they are not severely damaged. This characteristic can be easily guaranteed using algorithms based on clustering techniques. A manual segmentation of these muscles is shown in Figure 2(c). However, one should notice that the appearances of levator ani in static images are usually highly textured and have considerable variances in different slices. To identify the correct boundaries professional knowledge such as anatomical structures or information from multi-view images are needed. Modifications should focus on incorporating the spatial relationship between these muscles and other structures.

2.3 Algorithms based on deformable models

Compared with the above two types, the ones based on deformable models are more flexible and can be used for complex segmentations. Algorithms treat the structure boundary as the final status of the initial contours. The procedure of these algorithms can be viewed as a modelling of curve evolution. According to the way that is used for tracking the moving contour, deformable models can be further classified to parametric models and geometric models.

2.3.1 Parametric deformable models

Parametric deformable models track the evolution through sampled contour points. Explicit tracking has the advantage of high computational efficiency and allows for real-time applications. The moving equation for the contour can be derived through energy functional or defined directly through dynamic forces. A *priori* knowledge can be incorporated in the procedure of defining the energy functional, the initial conditions or the parameters. A typical energy functional includes the internal energy and the external energy. The internal energy aims to keep the regularity of the contour and is usually defined through the geometric properties of the contour such as length, area or curvature; the external energy attracts the contour to the boundary position and is defined by the image information. The definitions of external forces are the main differences between algorithms. Using calculus of variations, the Euler-Lagrange (E-L) equation of the energy functional with the internal forces and external forces can then be derived simultaneously. Since the definition of energy function guarantees that its minimum is achieved when the contours are at the position of structure boundaries, the E-L equation states that the balancing equilibrium of the contour

under external forces and internal forces is the right position of the structure boundary. Then the moving equation can be derived through adding a time variable to the E-L equation.

The development of parametric deformable models has a tight relationship with the snake method [53] which is the first deformable model applied to the medical image segmentation. The original snake method used the tension and rigidity of the contour as the internal energy and the gradient magnitude as the external energy. However, the snake method is sensitive to the initial conditions. The moving contour may stop at places with local functional minimum or places where the gradient magnitude is too small so that the external force tends to be zero. Also, the explicit tracking has the difficulty of handling topological changes. Consequently, in order to get a correct segmentation the initial contour must have the same topology as the desired object and must be placed near to the object boundary so that the external forces are strong enough.

The later proposed algorithms such as the ones proposed in [54-57] aimed to eliminate the dependence on the initial position and the noise influence. For example, in order to prevent the curves from shrinking or stopping on local minima, Cohen [54] added a balloon force to the external forces to make the contour inflate or deflate when the gradient field is weak. Xu and Prince [56] analyzed the reason why snake methods have poor convergence to boundaries with large curvatures and replaced the gradient field with the gradient vector field (GVF), which has a larger capture region and slowly changes away from the boundaries. Consequently, the dependence on initial positions is decreased but the field can attract the moving contour to the right position. In [55] except for adding the balloon force, an interactive mechanism was developed that allows user to select control points in order to form a constraining force to influence the curve movement. Numerical comparisons [58] have shown that these improved algorithms considerably decrease the influence of initial conditions and improve the segmentation results.

Parametric deformable models which incorporate statistical techniques are also popular. Typical examples include ASM [59, 60] and AAM [61]. Training samples are used to extract the mean shape and define proper ranges of the parameters. After finding an approximate position of the new examples, ASM uses the edge information to move the shape points to better positions while AAM used the mean texture of each shape point to find a better position. The searching procedure is like the snake

methods but the movements of shape points are constrained by the ranges of shape parameters which guarantee the similarity between the segmentation result and the training samples. This characteristic is very useful when the shape or topology of structures can hardly be identified from their appearances in the images. ASM and AAM have been applied widely in medical image segmentation and registration [50, 59, 62, 63].

Parametric deformable models are widely used in structure segmentation and 3D reconstructions. A system review can be found in [64]. However, the computational complexity such as parameterization of the contour, handling of topological changes and re-distribution of the contour points considerably restricts their applications.

2.3.2 Geometric deformable models

The geometric deformable models are based on the level set method [65] which was initially proposed to handle the topological changes during the curve evolution. The main idea of the level set method is to implicitly embed the moving contour into a higher dimensional level set function and view the contour as its zero level set. Then instead of tracking the discrete contour points, one can track the zero level set of the level set function. The advantage of doing so is that the topological changes can be easily handled and the geometric properties of the contour can be implicitly calculated. Therefore, the computational complexity of geometric deformable models is decreased. Like in the parametric deformable models, speed functions should be defined properly to drive the contour to the right position. Malladi et al. [66, 67] and Caselles et al. [68] applied level set methods to medical image segmentation. Malladi's algorithms used the gradient information to define the speed function and add the curvature influence to keep the contour smooth. The function of Malladi's speed model is intuitive: when the contour moves to the structure boundary, the increase of the gradient magnitude decreases the speed value so that the evolution of the contour slows down. Then, the evolution can be stopped after a time to gain the position of structure boundary. However, Malladi's speed models suffered from the drawback of leakage due to their bare dependence on the gradient information. The stopping criterion should be selected carefully to make sure the contour stops at the right position. If the images are noisy or blurred, the contour may leak or shrink to disappear after a long evolution [69-71]. To handle the leakage, the edge strength item [69] and area forces item [70] were incorporated to improve the model.

Unlike Malladi's model, geodesic active contour algorithm (GAC) modeled the segmentation as an optimization problem of finding the minimal distance curve in the image. Like in the parametric deformable models, the moving equation of GAC is derived from an energy function; the procedure of finding the optimal solution corresponds to the searching of the structure boundary. The moving equation is then obtained through the E-L equation. Instead of tracking the contour points, the contour is embedded in a level set function and therefore the moving equation becomes a level set equation. The speed function in GAC does not have an intuitive meaning; instead the derivation of the moving equation comes from energy function. Unlike in Malladi's models, the equilibrium state of the moving contour guarantees that a long computation will not lead to leakage.

The GAC algorithm shows a tight relationship between the parametric model and the geometric model. The introduction of the level set expression makes the algorithm flexible to handle the topological changes. GAC and the later improved GAC algorithms are widely applied to process the MR, CT and ultrasound images in order to accomplish tumor detection and cardiac segmentation. For example, in [72] a *priori* statistical techniques and shape information was incorporated. The contours are post-processed with the priori shape knowledge by using statistical techniques such as maximizing a posterior (MAP) and principle component analysis (PCA). In [73] the proposed algorithm combined the gradient vector flow field with the GAC algorithm to eliminate dependence on the initial conditions; intensity distributions in the left ventricle and the distance between the interfaces of endocardium and epicardium are incorporated. The results are better than the original GAC algorithm.

Another popular geometric model is proposed by Chan and Vese [74, 75]. Chan-Vese's model is a simplified version of Mumford-Shah energy model. The algorithm extracts the desired object through simultaneously minimizing the intensity variations inside and outside the contour. The most appreciable advantage of Chan-Vese's model is that it can obtain a boundary of discrete points, which is quite useful when the objects of interest are represented by discrete pixel clusters and have no clear definition of boundaries.

Most of the moving equations of the later proposed geometric deformable models are derived through the energy function because a *priori* knowledge and other techniques can be easily incorporated to the energy function. Algorithms based on geometric deformable models aim to eliminate noise influence, prevent leakage,

enhance accuracy and efficiency, make the algorithms more automatic and less dependent on the initial conditions. In order to achieve these goals, algorithms incorporated various cues such as image intensity and prior knowledge of structures. More details of geometric deformable models can be found in [71, 76]. A survey of algorithms that combine statistical techniques with level set methods can be found in [77].

Figures 3 and 4 illustrate the segmentation results of Malladi's algorithm and the GAC algorithm. Compared with the former segmentation results, the structure boundaries are more regular and less influenced by noise due to the smoothing items defined in the speed function. Nevertheless, small shape details such as the left bottom part of bladder are also erased. Proper stopping criterion should be defined for Malladi's algorithm; otherwise, the moving contours may leak, like the one illustrated in Figure 3(b). In this case, the PVE decreases the stopping strength at the right bottom boundary of rectum; hence, the contour leaked due to long evolution time. In Figure 4, the GAC algorithm provides a good segmentation of obturator internus, rectum and vagina. The regulating effects of internal forces make the boundary shape more reasonable and less influenced by noise. Also, leakage will not happen after long evolution time.

Deformable models are promising for the segmentation of the pelvic cavity because these models can easily incorporate statistical information, a *priori* knowledge and other techniques, while using the curve evolution to find the optimal boundaries can provide a contour with regular geometric properties. One possible way is to incorporate the comparative distances between organs and use prior shape information to constrain the deformation of the moving contour.

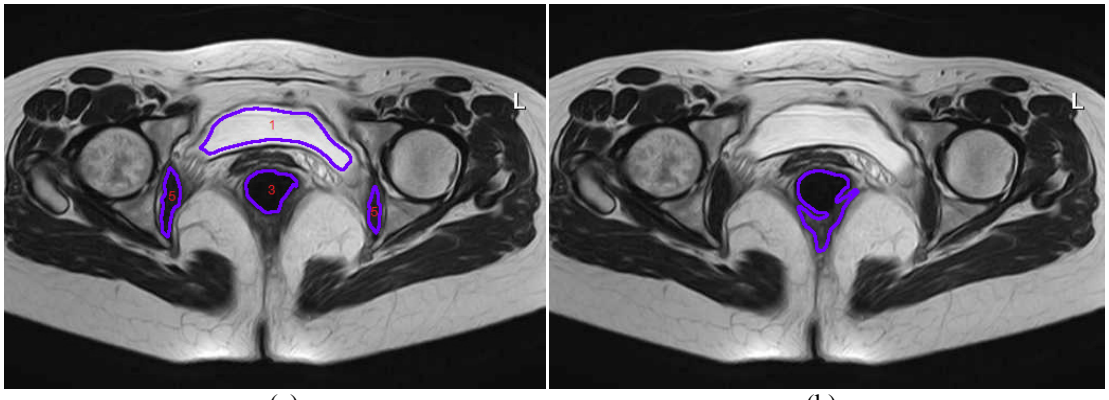

(a) (b)

Figure 3: (a) Malladi's algorithm (annotations are the same as in Figure 1c); (b) Leakage due to over evolution using Malladi's algorithm.

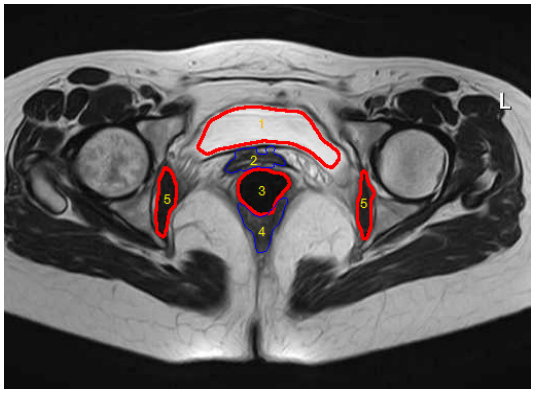

Figure 4: Geodesic active contour algorithm (annotations are the same as in Figure 1c).

3. Discussion

When the interested structures have distinctive quantifiable features, using threshold-based algorithms is effective. Procedures of these algorithms do not include complex operations and therefore are computationally efficient. However, due to their dependence on threshold values, algorithms are sensitive to noise, and most of them are difficult to be applied to multi-channel images. As medical images usually suffer from noise and intensity inhomogeneity, the segmentation results of threshold-based algorithms are far from satisfactory. Consequently, these algorithms are seldom used alone. Instead they are often used through incorporating a *priori* knowledge [16, 17]; or as an efficient pre-segmentation step [11, 12].

Except for the training step of the supervised classification algorithms, algorithms based on clustering techniques are also computationally efficient. Structure information can be easily used in these algorithms. When the interested structures in medical images are regular and not much influenced by noises, using pattern recognition techniques can sometimes achieve better results [27, 48]. If properly modeled, supervised classification algorithms can greatly enhance segmentation accuracy, especially when the appearance of structures is blurred or influenced by noise. The lack of incorporating spatial characteristics can be solved through using MRF model [78, 79]. Unsupervised classification algorithms can be applied to cases where there are few available segmentation samples or when the interested structures have large shape variations and have shown promise for medical image segmentation in fields like tumor detection in positron emission tomography (PET) imaging [1]. However, pattern recognition models are also sensitive to noise. Results of these algorithms depend on the initial conditions. For the supervised algorithms, the segmentation results depend on the size of the training sets and the correctness of the

segmentations in samples. For the unsupervised algorithms, the number of clusters, the position of initial points and the parameters used in the model should be properly defined. The applications of both supervised algorithms and unsupervised algorithms are constrained because of the large shape variations of organs and structures in medical images.

Due to the advantages of being able to handle structures with complex topology, easy to incorporate with another techniques, sub-pixel accuracy, noise insensitive and intuitive interaction mechanisms, the deformable models are intensively investigated in the last few decades. Parametric deformable models have high computational efficiency and can easily incorporate a *priori* knowledge [64]. However, these models cannot naturally handle topological changes and are sensitive to initial conditions. Geometric deformable models have the advantage of naturally handling the topological changes and are widely studied for medical segmentation [76]. Using a parametric model or geometric model depends on the concrete segmentation task. Topological flexibility is not always a desirable feature under some applications [80, 81]. In general, when structures have large shape variety or complicated topology, geometric deformable models are preferred; when the interested structures have open boundaries or the structures are thin or the algorithms need real-time operations, parametric models are preferred.

Deformable models in medical image segmentation have shown promising results and may continue to be focused in the next few years. Nevertheless, the deformable models also have disadvantages. Algorithms usually contain certain number of parameters. Parameters must be selected properly to get a satisfactory result while this is usually a time-consuming task.

4. Conclusions

As pointed out in Section 1, most of the algorithms combine multiple segmentation techniques and use diverse image cues to improve the segmentation results. Therefore, a definite classification of an algorithm may be infeasible. In this paper, current algorithms are classified into three types and their respective characteristics are summarized. Applications of the current algorithms to segment the organs contained in pelvic cavity were illustrated. These examples were also used to further state the

distinct characteristics of different types of algorithms. From the discussions, one can see that each segmentation algorithm category has its suitable application fields.

For the segmentation of the pelvic cavity, as some organs like the bladder can be successfully segmented using the current algorithms, its information should be combined with the relative position of organs or a 3D atlas and other image cues to segment the objects that are influenced by PVE or intensity inhomogeneity. To perform this, applying the algorithms based on deformable models can be a good choice. For structures such as the PF muscles whose boundaries cannot be defined barely through the image appearance, a *priori* shape model and a restriction on shape variations are needed. These tasks can be better fulfilled using the algorithms based on clustering techniques. Pixels with special features such as the edge points can be used to identify the boundary position or define the energy functional. The searching of these pixels can then be done by the efficient algorithms based on thresholds. In conclusion, for a concrete segmentation task in medical images, the application background and practical requirements such as accuracy of segmentation, computational complexity and interactive ability should all be considered in the design of algorithms.

Acknowledgment

This work was partially done in the scope of the projects "Segmentation, Tracking and Motion Analysis of Deformable (2D/3D) Objects Using Physical Principles" and "BIOPELVIC-Study of Female Pelvic Floor Disorders", with references POSC/EEA-SRI/55386/2004 and PTDC/SAU-BEB/71459/2006, financially supported by Fundação para a Ciência e a Tecnologia of Portugal. The authors would like to thank the anonymous reviewers for their valuable suggestions.

The first author would like to thank FCT for his PhD grant with reference SFRH/BD/43768/2008.

References

[1] Zaidi H. 2005. Quantitative Analysis in Nuclear Medicine Imaging. 1st ed. New York: Springer.

[2] Buchsbaum GM, Duecy EE, Kerr LA, Huang LS, Guzick DS. 2005. Urinary incontinence in nulliparous women and their parous sisters. Obsete Gynecol. 106(6):1253-1258.

[3] Siproudhis L, Pigot F, Godeberge P, Damon H, Soudan D, Bigard MA. 2006. Defecation disorders: a French population survey. Dis Colon Rectum. 49(2):219-227.

[4] Drossman DA, Li Z, Andruzzi E. 1993. U.S. householder survey of functional gastrointestinal disorders: prevalence, sociodemography, and health impact. Dig Dis Sci. 38(9):1569-1580.

[5] Nelson R, Norton N, Cautley E, Furner S. 1995. Community based prevalence of anal incontinence. J Amer Med Assoc. 274(7):559-561.

[6] Macmillan AK, Merrie AEH, Marshall RJ, Parry BR. 2004. The prevalence of fecal incontinence in community-dwelling adults: a systematic review of the literature. Dis Colon Rectum. 47(8):1341-1349.

[7] Otsu N. 1979. A threshold selection method from gray-level histograms. IEEE T Syst Man Cyb. 9(1):62-66.

[8] Chui CK. 1993. An introduction to wavelets. SIAM Rev. 35(2):312-313.

[9] Canny J. 1986. A computational approach to edge detection. IEEE T Pattern Anal. 8(6):679-698.

[10] Davis LS. 1975. A survey of edge detection techniques. Comput Vision Graph. 4(3):248-270.

[11] Andreao RV, Boudy J. 2007. Combining wavelet transform and hidden Markov models for ECG segmentation. EURASIP J Appl Sig P. 2007(1):95.

[12] Qin XJ, Jiang JH, Wang WH, Zhang F. 2007. Canny operator based level set segmentation algorithm for medical images. Paper presented at: ICBBE 2007. Proceedings of the 1st International Conference on Bioinformatics and Biomedical Engineering; Wuhan, China.

[13] Adams R, Bischof L. 1994. Seeded region growing. IEEE T Pattern Anal. 16(6):641-647.

[14] Pohle R, Toennies KD. 2001. Segmentation of medical images using adaptive region growing. Paper presented at: MI 2001. Proceedings of the SPIE Medical Imaging 2001. San Diego, California, USA.

[15] Yi J, Ra JB. 2001. Vascular segmentation algorithm using locally adaptive region growing based on centerline estimation. Paper presented at: MI 2001. Proceedings of the SPIE Medical Imaging 2001; San Diego, California, USA.

[16] Pan ZG, Lu JF. 2007. A Bayes-based region-growing algorithm for medical image segmentation. Comput Sci Eng. 9(4):32-38.

[17] Dehmeshki J, Ye X, Costello J. 2003. Shape based region growing using derivatives of 3D medical images: application to semiautomated detection of pulmonary nodules. Paper presented at ICIP 2003. Proceedings of the 2003 International Conference on Image Processing; Barcelona, Spain.

[18] Beucher S, Lantue´joul C. 1979. Use of watersheds in contour detection. Proceeding of International Workshop on Image Processing, Real-Time Edge and Motion Detection/Estimation; Rennes, France.

[19] Vincent L, Soille P. 1991. Watersheds in digital spaces: an efficient algorithm based on immersion simulations. IEEE T Pattern Anal. 13(6):583-598.

[20] Grau V, Mewes AU, Alcañiz M, Kikinis R, Warfield SK. 2004. Improved watershed transform for medical image segmentation using prior information. IEEE T Med Imaging. 23(4):447-458.

[21] Ng HP, Ong SH, Foong KWC, Goh PS, Nowinski WL. 2006. Medical image segmentation using k-means clustering and improved watershed algorithm. Paper presented at: SSIAI 2006. Proceedings of the IEEE Southeast Symposium on Image Analysis and Interpretation; Denver, Colorado, USA.

[22] Hamarneh G, Li XX. 2009. Watershed segmentation using prior shape and appearance knowledge. Image Vision Comput. 27(1):59-68.

[23] Haris K, Efstratiadis SN, Maglaveras N, Katsaggelos AK. 1998. Hybrid image segmentation using watershed and fast region merging. IEEE T Image Process. 7(12):1684-1699.

[24] Sarti A, Corsi C, Mazzini E, Lamberti C. 2005. Maximum likelihood segmentation of ultrasound images with rayleigh distribution. IEEE T Ultrason Ferr. 52(6):947-960.

[25] Vrooman HA, Cocosco CA, Stokking R, Arfan IM, Vemooij MW, Breteler MM, Niessen WJ. 2006. kNN-based multi-spectral mri brain tissue classification: manual training versus automated atlas-based training. Paper presented at: MI 2006. Proceedings of the SPIE Medical Imaging 2006; California, USA.

[26] Bishop CM. 2006. Pattern recognition and machine learning, 1st ed. New York, NY: Springer.

[27] Bezdek JC, Hall LO, Clarke LP. 1993. Review of MR image segmentation techniques using pattern recognition. Med Phys. 20(4):1033-1048.

[28] Alirezaie J, Jernigan ME, Nahmias C. 1997. Neural network-based segmentation of magnetic resonance images of the brain. IEEE T Nuclear Sci. 44(2):194-198.

[29] Wang S, Zhu WY, Liang ZP. 2001. Shape deformation: SVM regression and application to medical image segmentation. Paper presented at: ICCV 2001. Proceedings of the 8th International Conference on Computer Vision; Vancouver, British Columbia, Canada.

[30] Benamrane N, Aribi A, Kraoula L. 2006. Fuzzy neural networks and genetic algorithms for medical images interpretation. Paper presented at: GMAI 2006. Proceedings of Geometric Modeling and Imaging; London, UK.

[31] James M. 1985. Classification algorithms, 1st ed. New York, NY: Wiley-Interscience.

[32] Mitchell T. 1997. Machine Learning, 1st ed. McGraw-Hill.

[33] Jacobs MA, Knight RA, Soltanian-Zadeh H, Zheng ZG, Goussev AV, Peck DJ, Windham JP, Chopp M. 2000. Unsupervised segmentation of multiparameter MRI in experimental cerebral ischemia with comparison to T2, diffusion, and ADC MRI parameters and histopathological validation. J Magn Reson Im. 11(4):425-437.

[34] Biswal B, Shah N, Shah N, Trivedi M, Nayak S, Dave H. 2006. Automatic segmentation of pancreatic images using ISODATA algorithm. J Clin Oncol 2006 ASCO Annu Meet Proc. 24(18):14149.

[35] Tai XY, Song WH. 2007. An improved approach based on FCM using feature fusion for medical image retrieval. Paper presented at: FSKD 2007. Proceedings of the 4th International Conference on Fuzzy Systems and Knowledge Discovery; Hainan, China.

[36] Pham DL, Prince JL. 1999. An adaptive fuzzy c-means algorithm for image segmentation in the presence of intensity inhomogeneities. Pattern Recogn Lett. 20(1):57-68.

[37] Ahmed MN, Yamany SM, Mohamed N, Farag AA, Moriarty T. 2002. A modified fuzzy C-means algorithm for bias field estimation and segmentation of MRI data. IEEE T Med Imaging. 21(3):193-199.

[38] Cai WL, Chen SC, Zhang DQ. 2007. Fast and robust fuzzy C-means clustering algorithms incorporating local information for image segmentation. Pattern Recogn. 40(3):825-838.

[39] Wang J, Kong J, Lu Y, Qi M, Zhang B. 2008. A modified fcm algorithm for mri brain image segmentation using both local and non-local spatial constraints. Comput Med Imag Grap. 32(8):685-698.

[40] Zhou HY, Schaefer G, Sadka A, Celebi ME. 2008. Anisotropic mean shift based fuzzy c-means segmentation of skin lesions. Paper presented at: CSTST 2008. Proceedings of the 5th International Conference on Soft Computing as Transdisciplinary Science and Technology; Cergy-Pontoise, Paris, France.

[41] Zhang DQ, Chen SC. 2003. Robust image segmentation using FCM with spatial constraints based on new kernel-induced distance measure. IEEE T Syst Man Cyb. 34(4):1907-1916.

[42] Liao L, Lin TS, Li B. 2008. MRI brain image segmentation and bias field correction based on fast spatially constrained kernel clustering approach. Pattern Recogn Lett. 29(10):1580-1588.

[43] Clark MC, Hall LO, Goldgof DB, Clarke LP, Hajj LO, Velthuizen RP, Silbiger MS. 1994. MRI segmentation using fuzzy clustering techniques. IEEE Eng Med Biol. 13(5):730-742.

[44] Mohamed NA., Ahmed MN, Farag A. 1999. Modified fuzzy c-mean in medical image segmentation. Paper presented at: ICASSP 99. Proceedings of the 20th Annual International Conference on Acoustics, Speech, and Signal Processing. Phoenix, Arizona, USA.

[45] Sarle WS. 1994. Neural networks and statistical models. Paper presented at: SUGI 19. Proceedings of the 19th Annual SAS Users Group International Conference; Dallas, Texas, USA.

[46] Cheng KS, Lin JS, and Mao CW. 1996. The application of competitive Hopfield neural network to medical image segmentation. IEEE T Med Imaging. 15(4):560-567.

[47] Lin JS, Cheng KS, and Mao CW. 1996. A fuzzy Hopfield neural network for medical image segmentation. IEEE T Nucl Sci. 43(4):2389-2398.

[48] Becker S, Plumbley M. 1996. Unsupervised neural network learning procedures for feature extraction and classification. Appl Intell. 6(3):185-203.

[49] Gindi G, Rangarajan A, Zubal G. 1993. Atlas-guided segmentation of brain images via optimizing neural networks. Proceedings of the SPIE Biomedical Image Processing IV; San Jose, California, USA.

[50] Ginneken BV, Frangi AF, Frangi RF, Staal JJ, Romeny BM, Viergever MA. 2002. Active shape model segmentation with optimal features. IEEE T Med Imaging. 21(8):924-933.

[51] Akselrod-Ballin A, Galun M, Gomori M, Basri R, Brandt A. 2006. Atlas guided identification of brain structures by combining 3D segmentation and SVM classification. Paper presented at: MICCAI 2006. Proceeding of the 9th International Conference on Medical Image Computing and Computer Assisted Intervention; Copenhagen, Denmark.

[52] Kindermann R, Snell JL. 1980. Markov Random Fields and Their Applications. Rhode Island: American Mathematical Society.

[53] Kass M, Witkin A, Terzopoulos D. 1987. Snakes: active contour models. Int J Comput Vision. 1(4):321-331.

[54] Cohen LD. 1991. On active contour models and balloons. Comput Vis Image Und. 53(2):211-218.

[55] McInerney T, Terzopoulos D. 1995. A dynamic finite element surface model for segmentation and tracking in multidimensional medical images with application to cardiac 4D image analysis. Comput Med Imag Grap. 19(1):69-83.

[56] Xu CY, Prince JL. 1998. Snakes, shapes, and gradient vector flow. IEEE T Image Process. 7(3):359-369.

[57] Gonçalves PC, Tavares JM, Jorge RM. 2008. Segmentation and simulation of objects represented in images using physical principles. Comp Model Eng. 32(1):45-55.

[58] He L, Peng ZG, et al. 2008. A comparative study of deformable contour methods on medical image segmentation. Image Vision Comput. 26(2):141-163.

[59] Cootes TF, Hill A, Taylor CJ, Haslam J. 1994. The use of active shape models for locating structures in medical images. Image Vision Comput. 12(6):355-366.

[60] Cootes TF, Taylor CJ, Cooper DH, Graham J. 1995. Active shape models - their training and application. Comput Vis Image Und. 6(1):38-59.

[61] Cootes TF, Edwards GJ, Taylor CJ. 2001. Active appearance models. IEEE T Pattern Anal. 23(6):681-685.

[62] Beichel R, Bischof H, Leberl F, Sonka M. 2005. Robust active appearance models and their application to medical image analysis. IEEE T Med Imaging. 24(9):1151-1169.

[63] Vasconcelos MJM, Tavares JMRS. 2008. Methods to automatically built point distribution models for objects like hand palms and faces represent in images. Comput Model Eng. 36(3):213-241.

[64] McInerney T, Terzopoulos D. 1996. Deformable models in medical image analysis: a survey. Med Image Anal. 1(2):91-108.

[65] Osher S, Sethian J. 1988. Fronts propagating with curvature-dependent speed: algorithms based on Hamilton-Jacobi formulations. J Comput Phys. 79(1):12-49.

[66] Malladi R, Sethian JA, Vemuri B. 1993. A topology independent shape modeling scheme. Proceedings of the SPIE Conf. on Geometric Methods in Computer Vision II; San Diego, California, USA.

[67] Malladi R, Sethian JA. 1996. Level set and fast marching methods in image processing and computer vision. Paper presented at: ICIP 96. Proceedings of the IEEE International Conference on Image Processing; Lausanne, Switzerland.

[68] Caselles V, Kimmel R, and Sapiro G. 1997. Geodesic active contours. Int J Comput Vision. 22(1):61-79.

[69] Kichenassamy S, Kumar A, Olver P, Tannenbaum A, Yezzi AJ. 1996. Conformal curvatures flows: from phase transitions to active vision. Arch Ration Mech An. 134(3):275-301.

[70] Siddiqi K, Lauziere YB, Tannenbaum A, Zucker SW. 1998. Area and length minimizing flows for shape segmentation. IEEE T Image Process. 7(3):433-43.

[71] Suri JS, Liu KC, Singh S, Laxminarayan SN, Zeng XL, Reden L. 2002. Shape recovery algorithms using level sets in 2-D/3-D medical imagery: a state-of-the-art review. IEEE T Inf Technol B. 6(1):8-28.

[72] Leventon M, Grimson W, Faugeras O. 2000. Statistical shape influence in geodesic active contours. Paper presented at: CVPR 2000. Proceedings of the IEEE Conf. on Comp. Vision and Pattern Recognition; Hilton Head Island, South Carolina, USA.

[73] Paragios N, 2002. A variational approach for the segmentation of the left ventricle in cardiac image analysis. Int J Comput Vision. 50(3):345-362.

[74] Chan T, Vese LA. 1999. An active contour model without edges. Proceedings of the Int. Conf. Scale-Space Theories in Computer Vision; Corfu, Greece.

[75] Chan T, Vese LA. 2002. Active contour and segmentation models using geometric PDE's for medical imaging. Geometric Methods in Bio-Medical Image Processing. Springer.

[76] Niessen WJ, Romeny EM, Viergever MA. 1998. Geodesic deformable models for medical image analysis. IEEE T Med Imaging. 17(4):634-641.

[77] Cremers D, Rousson M, Deriche R. 2007. A review of statistical approaches to level set segmentation: integrating color, texture, motion and shape. Int J Comput Vision. 72(2):195-215.

[78] Held K, Kops ER, Krause BJ, Wells III WM, Kikinis R, Muller-Gartner HW. 1997. Markov random field segmentation of brain MR images. IEEE T Med Imaging. 16(6):878-885.

[79] Flitti F, Collet C, Joannic-Chardin A. 2005. Unsupervised multiband image segmentation using hidden Markov quadtree and copulas. Paper presented at: ICIP 2005, Proceedings of the 2005 International Conference on Image Processing; Genova, Italy.

[80] Han X, Xu CY, Prince JL. 2003. A topology preserving level set method for geometric deformable models. IEEE T Pattern Anal. 25(6):755-768.

[81] Guyader CL, Vese LA. 2008. Self-repelling snakes for topology-preserving segmentation models. IEEE T Image Process. 17(5):767-779.

Part B – Article 2

Segmentation of Female Pelvic Organs in Axial Magnetic Resonance Images using Coupled Geometric Deformable Models

Zhen Ma, Renato Natal Jorge, T. Mascarenhas, João Manuel R. S. Tavares

Submitted to an international journal (Under review, after revision), 2012.

Abstract

The segmentation of pelvic structures in magnetic resonance (MR) images of the female pelvic cavity is a challenging task. This paper proposes the use of three novel geometric deformable models to segment the bladder, vagina and rectum in axial MR images. The different imaging appearances and prior shape knowledge are combined into a level set framework as segmentation clues. The moving contours are coupled with each other based on interactive information, and the organ boundaries can be segmented simultaneously. With the region-based external forces defined, the proposed algorithms are robust against noise and partial volume effect.

Keywords: Image Segmentation; Level Set; Prior Shape Knowledge; Imaging Appearance; Bladder; Vagina; Rectum.

1. Introduction

Pelvic organ prolapse and pelvic floor dysfunction are common clinical conditions affecting a large number of women [1-5]. For example, from 30 to 50% of women in Europe and the USA suffer from urinary incontinence (UI) [4]; by the age of 80, 11.1% of women have undergone operations for pelvic organ prolapse or UI, and many of them have experienced more than one operation [5]. However, the pathophysiology and its relationship with the symptoms are still unclear. Findings from epidemiologic studies are usually inconsistent, because they are not designed to investigate cause-and-effect relationships.

For a patient-specific study, the development of novel and less invasive therapies requires a thorough knowledge of the relationship between the pathophysiology of incontinence and anatomy; an anatomic analysis lays the necessary foundation for understanding the specific mechanical etiologies of pelvic floor disorders [6, 7]. Static magnetic resonance imaging (MRI), especially T2-weighted imaging, is currently a preferred modality for this study [8-10]. The imaging data from MRI have improved the accuracy of clinical diagnoses considerably and assisted the planning of therapeutic strategies. Nevertheless, in order to carry out quantitative analyses or biomechanical simulations, the relevant structures need to be segmented in 2D image

slices. This process is presently done by manual segmentation, which is usually very time consuming (often 1-2 hours) [11, 12] and can lead to results that suffer from intra/inter observer errors, particularly when the images were influenced by noise and partial volume effect [13, 14]. Therefore, effective segmentation algorithms are required.

Due to the complex anatomy, the segmentation of the structures in the pelvic cavity needs to be carried out carefully. Applying the current segmentation algorithms to the female pelvic cavity was discussed in [13], and it was concluded that an effective algorithm should be based on imaging features of the relevant pelvic structure. A deformable model was then proposed in [14], which combined the imaging appearance with the prior knowledge, and was able to handle the segmentation of the levator ani muscles in T2-weighted MR images. A coupled surface evolution algorithm was proposed in [15] to segment the prostate and the bladder in CT images. This approach combines a shape constraint to assist the segmentation and uses a coupling technique to avoid overlapping of the two organs.

However, few algorithms have been proposed to segment the pelvic organs in MR images and most of them are not suitable for T2-weighted MR images [16-18]. For example, the seeded region growing algorithm [19] was proposed to segment the bladder and the rectum in [16] but this algorithm is sensitive to image noise and the initial conditions adopted. A coupled level set framework, which can handle successfully the segmentation of inner and outer bladder walls in T1-weighted MR images, was proposed in [17]. Nevertheless, in T2-weighted images the bladder has different imaging appearances, and the influence of noise and partial volume effect (PVE) is more appreciable.

This paper focuses on the segmentation of axial T2-weighted MR images because using T2-weighted MR images the pelvic structures are seen more clearly and the physiological anatomy of the pelvic structures can be clearly identified on the axial plane [7]. Geometric deformable models are among the segmentation techniques that have been intensively studied in recent years. Due to their ability to incorporate various segmentation clues, they are ideal for the segmentation of pelvic structures [13]. In this paper, a coupling approach is proposed to segment the bladder, vagina and rectum from axial T2-weighted MR images of the female pelvic cavity. The approach proposes three novel geometric deformable models that couple with each other and segment the three organs simultaneously. The distinct imaging appearances

of the organs and the prior shape knowledge are incorporated into a level set framework. Using the adopted external forces, the pelvic organs can be accurately segmented even when there is noise and PVE. Several numerical experiments have given very promising results and have demonstrated the effectiveness of the proposed approach.

The paper is organized as follows: In Section 2, the female pelvic anatomy and geometric deformable models are reviewed. Section 3 introduces the novel coupling approach along with detailed explanations about the associated moving equations. Then, in Sections 4 and 5, various numerical experiments are presented and discussed. Finally, in the last section, the main contributions are outlined and future works are suggested.

2. Background

2.1 Anatomy and imaging appearance

In axial T2-weighted MR images, the spatial relationship of the pelvic organs can be well depicted and the imaging appearances of the three pelvic organs and surrounding tissues are satisfactorily distinct. An example can be seen in Figure 1.

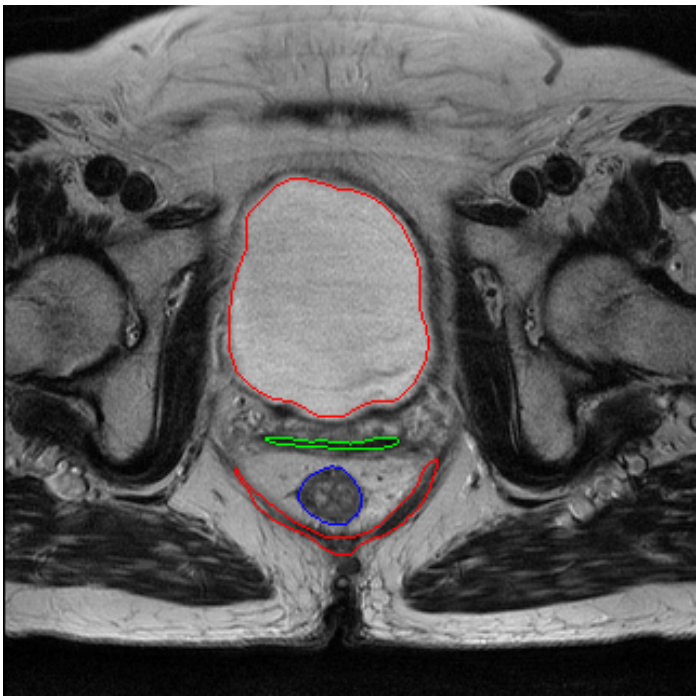

Figure 1: Axial view of pelvic cavity with the boundaries of the structures identified, from top to bottom: bladder (in red), vagina (in green), rectum (in blue), and the levator ani muscle (in purple).

The urinary bladder is a hollow distensible organ composed of smooth muscular walls; mainly, the detrusor muscle (Figure 1). In the female pelvic cavity, the urinary bladder sits inferior to the uterus and anterior to the vagina. It is a temporary reservoir for urine whose status is closely related to its contents and the state of neighboring organs [22]. In T2-weighted MR images, the bladder lumen has high signal intensity due to the urine within it, while the muscular bladder wall has intermediate signal intensity that is similar in appearance to the vaginal and rectal walls.

The vagina is a muscular sheath-like structure that extends from the cervix to the vulva (Figure 1). It is located in front of the rectum and behind the bladder. The widest part of the vaginal is at the proximal vagina (32.5 mm) then its width decreases as it passes through the pelvic floor (27.8 mm) and becomes narrowest at the introitus (26.2 mm) [23]. The different layers of the vagina can be observed in T2-weighted axial MR images. The outer muscular layers have homogeneous low signal intensity, while the mucosal layer and the secretions within the vaginal canal have high signal intensity. The appearance of the mucosal layer varies with hormonal stimulation: in women that are before menarche or after menopause, the high signal intensity central strip is very thin; but in women of reproductive age, the high signal intensity central stripe can be clearly observed, especially during the secretory phase [24]. The tissues around the vagina also have high signal intensity but are appreciably lower than the signal intensity of the bladder lumen. Nevertheless, these tissues around the vagina are more similar to the bladder lumen than to the vagina and rectum.

The rectum is the terminal portion of the large intestine, and lies posterior to the uterus following the curvature of the sacrum (Figure 1). The rectum also has different layers with large variances in their appearances. The muscular layer of the rectum has intermediate signal intensity that is distinguishable from the bladder wall; while the rectal lumen, which is bounded by the mucosa and submucosa, has low signal intensity similar to the muscular vaginal wall. The tissues around the rectum have appearances alike those around the vagina.

With the complex imaging background of the female pelvic cavity, the information just about the intensity gradient is not sufficient to carry out an accurate segmentation. Figure 2 illustrates the segmentation results using the geodesic active contour [25], from which one can see that the inhomogeneous signal intensity of the pelvic organs is an obstacle for algorithms that use the gradient information. Due to

the influence of noise and PVE, the boundaries either stop incorrectly at places with a high intensity gradient or leak outside.

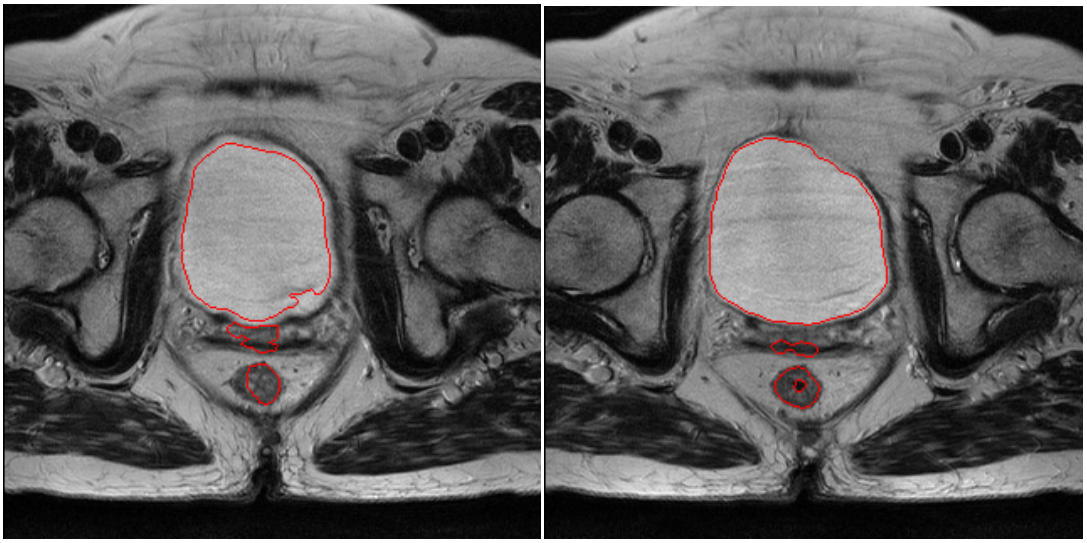

(a) (b)

Figure 2: Segmentation results using the geodesic active contours algorithm: (a) with unclear inner layer of rectum; (b) with clear inner layer of rectum.

On T2-weighted MR images, the bladder lumen has high signal intensity, while the bladder wall has a low signal intensity that is similar to the appearance of the muscular layer of the rectum. Regarding the vagina and rectum, the surrounding fat tissues have comparably high signal intensity appearances that are more like the bladder lumen than the other two organs. The different appearances of the pelvic organs and the similarity between the organ layers and the surrounding tissues are valuable segmentation clues. Moreover, although the vagina and rectum normally have blurred imaging appearances with highly inhomogeneous signal intensities on T2-weighted MR images, their shapes do not change much in an image series under the axial planes; therefore, prior shape information can be used to provide shape guidance. Based on these features, the three pelvic organs can be segmented using geometric deformable models.

2.2 Geometric deformable models

Geometric deformable models can segment images using a curve evolution and the level set method [26]. In these models, initial contours are defined first and then moved according to a speed function until they reach the boundary to be segmented. Usually, the moving equation of a geometric deformable model is a level set equation such as [26]:

$$\phi_t + F\left|\nabla\phi\right| = 0\,, \tag{1}$$

where $\phi(X,t)$ is the level set function typically defined as the signed distance function, and $F(X,t)$ is the speed function.

By using the level set method, the geometric deformable models have low computational complexity and can handle the topological changes during the contour movement. The definition of speed function should guarantee that the moving contours are attracted to the desired boundaries; in this process, segmentation clues, restrictions on contour movement, and other techniques can be easily incorporated to the model. These features are attractive for medical imaging [13, 27-29]. Based on the anatomy and the imaging features of the pelvic cavity, using geometric deformable models can be a suitable way to carry out the segmentation.

2.2.1 Multiphase segmentation

If there are more than two regions or structures to be segmented, suitable strategies should be added to the geometric deformable models. One possibility is to use different level set functions for distinct regions. An effective model was proposed in [30] as the minimization of the following energy functional:

$$E(\Gamma,\{\alpha_i\}) = \sum_{i=1}^{N}\left(\frac{\mu}{2}\int_{\partial R_i} ds - \log\left(P\left(\left\{I_{(x,y)} : (x,y)\in R_i\right\}\middle|\alpha_i\right)\right) + \lambda\right), \quad (2)$$

where μ is the weight that controls the influence of the boundary length – a large μ is favorable to merge small sub-regions and avoid over-segmentation, ∂R_i is the boundary of the region R_i, and $P(I|\alpha_i)$ is the pre-specified posteriori probability density function with α_i standing for the parameters contained in these functions; for example, when P is a Gaussian distribution, and α_i are the mean and variance of the image intensity. The first term in Eq. (2) is related to the length of the boundaries, and serves as the internal energy to control the smoothness of the moving contour. The second term calculates the cost of classifying the pixels to their current region, and serves as the external energy to attract the contours to the correct boundaries. The third term λ is a weight defined for each region R_i based on the image contents; for example, λ can be penalties related to the area of each region.

Although Eq. (2) gives a rigorous modeling for the multiphase segmentation, the minimization of the functional requires complex operations [30, 31]. To solve this problem, the following region competition model was proposed [20]:

$$\frac{\partial \phi_i}{\partial t} = \delta(\phi_i)\left(e_i - \max_{\delta(\phi_j)>0, j\neq i} \left(e_j, e_i - 1\right)\right), \text{ with} \tag{3}$$

$$e_k = \log(p_k) + \gamma \operatorname{div}\left(\frac{\nabla \phi_k}{|\nabla \phi_k|}\right),\ i,k = 1,\cdots,N,$$

where γ is the weight of the internal force used to control the smoothness of the moving contour – a larger γ corresponds to a smoother boundary, δ is the Dirac function with the Heaviside function (i.e. the unit step function) defined as $H(x)=1$, for $x \geq 0$ and $H(x)=0$, for $x<0$, and p_k is the probability of a pixel belonging to the *k*-th region and is calculated using the probability density function $P\left(I|\alpha_k\right)$ in Eq. (2).

The contour movement given by Eq. (3) depends on the competitions among the neighboring regions, which is reflected by the comparison between the logarithms of the probabilities. The contours with the highest probability among their neighbors will expand, while the others will retract. The condition for the maximum operator requires that only contours which are close enough can compete with each other; and the additional term $e_i - 1$, assures that if there is a vacuum between neighboring regions, the best fitting region will move forward. Thus, an image can be segmented completely, while the overlapping of contours is avoided.

2.2.2 Prior shape knowledge

Prior shape information is a valuable clue for robust and efficient image segmentation algorithms. To apply the shape guidance, the difference between the current shape and the prior shape needs to be quantified. By using the dissimilarity measure defined in [32, 33], an effective shape energy functional was proposed as [21]:

$$E(\phi) = d^2(\phi, \phi_0) = \int_\Omega \left(H\left(\phi\left(x + \mu_\phi\right)\right) - H\left(\phi_0(x)\right)\right)^2 dx, \tag{4}$$

where Ω is the image region, ϕ_0 is the level set function representing the prior shape, and μ_ϕ is the center of gravity of the area defined by the moving contour that can be calculated as $\mu_\phi = \int_\Omega xH(\phi)dx \Big/ \int_\Omega H(\phi)dx$. The addition of μ_ϕ can intrinsically align the current shape and the prior shape to the same coordinates of the center of gravity.

Based on the Euler-Lagrange equation of Eq. (4), the moving equation was derived as:

$$\frac{\partial \phi}{\partial t} = -\left(H\left(\phi(x)\right) - H\left(\phi_0\left(x-\mu_\phi\right)\right)\right) - \frac{\left(x-\mu_\phi\right)^T}{\int H(\phi)\,dx} \times \int \left(H\left(\phi(x')\right) - H\left(\phi_0\left(x'-\mu_\phi\right)\right)\right)\delta\left(\phi(x')\right)\nabla\left(\phi(x')\right)dx' \quad . \tag{5}$$

Using this equation, the moving contour will match the prior shape. The model represented in Eq. (5) provides a simple way to provide the shape guidance. However, the use of shape guidance normally works on the premise that the structure to be segmented does not have large shape variations. Here, the shapes of the pelvic organs are closely related to the patient's physiological status and have considerable variations among different individuals. Therefore, no representative training set is available and special treatments are required in order to use this information for segmentation.

3. Methods

Due to the complex imaging background and the irregular shapes, it is difficult to define a region of interest (ROI) that covers the three pelvic organs in a simple background. Three level set functions were defined and used coupled together to segment, simultaneously, the three pelvic organs: Bladder, Vagina and Rectum. Since these organs are near to each other, initial contours were defined manually within the boundaries of each organ in order to obtain the correct intensity distributions and exclude the influences among the organs and from their neighboring structures, such as the obturator internus muscles. Hence, the segmentation is accomplished through the expansion of the moving contours.

To facilitate the following discussion, the level set function ϕ_1 is used to segment the bladder, ϕ_2 for the vagina, and ϕ_3 for the rectum. All the initial level set functions are defined as the signed distance functions with positive (negative) values inside (outside) the contour. Correspondingly, the internal region of the moving contour i at the time t is $\Omega_i = \left\{(x,y)\middle|\phi_i(x,y,t) \geq 0\right\}$, with $i = 1,2,3$.

3.1 Bladder

As discussed in Section 2.1, the bladder can have large shape variations even in the same image series. Hence, no prior shape information is available. Additionally, the imaging appearances of the bladder can vary largely due to the inhomogeneous magnetic field. Segmentation only through the intensity or the intensity gradient is not reliable. However, given the different appearances of the pelvic organs and the appearance of the bladder wall, if the initial contours are placed inside the bladder lumen and expand according to the local intensity similarity, they will stop at the bladder wall. Hence, the region competition model in Eq. (3) can be used to segment the bladder. Since the three initial contours are all inside the organs and the organs are spatially next to each other, the gaps between the pelvic organs should not be covered by the moving contours. Therefore, the term $e_1 - 1$ in the maximum operator of Eq. (3) should be removed and the moving equation for segmenting the bladder should be:

$$\frac{\partial \phi_1}{\partial t} = \delta(\phi_1)\left(e_1 - \max(e_2, e_3) + \gamma \operatorname{div}\left(\frac{\nabla \phi_1}{|\nabla \phi_1|} \right) \right), \tag{6}$$

where $e_k = \log(p_k)$, $k = 1, 2, 3$.

Nevertheless, there are still problems when using the above moving equation. To clarify this point, supposing the intensity distribution of the pelvic organs can be described by the Gaussian functions and $e_2 \geq e_3$, then the external force is:

$$e_1 - \max(e_2, e_3) = -\frac{1}{2}\left(\frac{1}{\sigma_1^2} - \frac{1}{\sigma_2^2} \right) I^2 + \left(\frac{u_1}{\sigma_1^2} - \frac{u_2}{\sigma_2^2} \right) I - \frac{1}{2}\left(\frac{u_1^2}{\sigma_1^2} - \frac{u_2^2}{\sigma_2^2} \right) + \log\left(\frac{\sigma_2}{\sigma_1} \right),$$

where u_i and σ_i are the mean and standard deviation of the intensity, respectively.

For the sake of simplicity, if one considers $\sigma_1 = \sigma_2 = \sigma$, then the above formula becomes:

$$e_1 - \max(e_2, e_3) = \frac{u_1 - u_2}{\sigma^2}\left(I - \frac{u_1 + u_2}{2} \right).$$

As the mean intensity of the bladder region is highest among the three pelvic organs ($u_1 > u_2$), the speed function in Eq. (6) is an increasing function of the image intensity I when $I > \frac{u_1 + u_2}{2}$. However, the relationship between the probability p_1 and the contour movement is unclear. For example, if the contour arrives at the pixels with intensity $I > u_1 + 3\sigma_1$, which means p_1 is small and the contour is probably moving

outside the bladder region, the contour will still move forward with a speed greater than the ones at the pixels with intensity $|I-u_1|<3\sigma_1$. This is undesirable as the moving contour is supposed to be attached to the structure boundary.

According to Eq. (3), the moving contours should stop at the region boundaries because pixels outside a region are more likely to belong to another region and therefore should be covered by a competing contour. While here the appearance comparison is only among the three pelvic organs, in some images the appearances of the perivesical tissues and fats are more similar to the bladder compared with the other two organs; then, the speed values calculated by Eq. (6) may still be large, even if the value of p_1 is small. If the bladder wall is blurred, when the contour moves there, the large expanding speed will make the contour leak into the surrounding tissues and will not be able to draw back. A case in point is shown in Figure 3. The relationship between p_1 and the expanding speed is shown in Figure 3c by using the scatter diagram of the pixels inside a neighboring band (r = 10) around the bladder boundary. One can see that, due to the maximum and logarithmic operations involved, the expanding speeds can be quite different even if the values of p_1 are similar; and when p_1 is small, the speed value does not decrease sharply.

Thus, the good properties of the region competition model in Eq. (3) cannot be used for the local segmentation. To solve these problems, the moving equation is proposed as:

$$\frac{\partial \phi_1}{\partial t}=\delta(\phi_1)\left(p_1\left(e_1-\max\left(e_2,e_3,e_1-1\right)\right)+\alpha\nabla p_1\cdot\nabla\phi_1+\gamma_1\mathrm{div}\left(\frac{\nabla\phi_1}{|\nabla\phi_1|}\right)\right), \tag{7}$$

where δ is the Dirac function, $p_i=\frac{1}{\sqrt{2\pi}\sigma_i}\exp\left(-\frac{(I-u_i)^2}{2\sigma_i^2}\right)$ and $e_i=\log(p_i)$, u_i and σ_i are the mean and the standard deviation of the intensity inside the moving contour i, with $i=1,2,3$, α is the weight to control the influence of the probability gradient field and γ_1 is the weight to control the influence of the internal force.

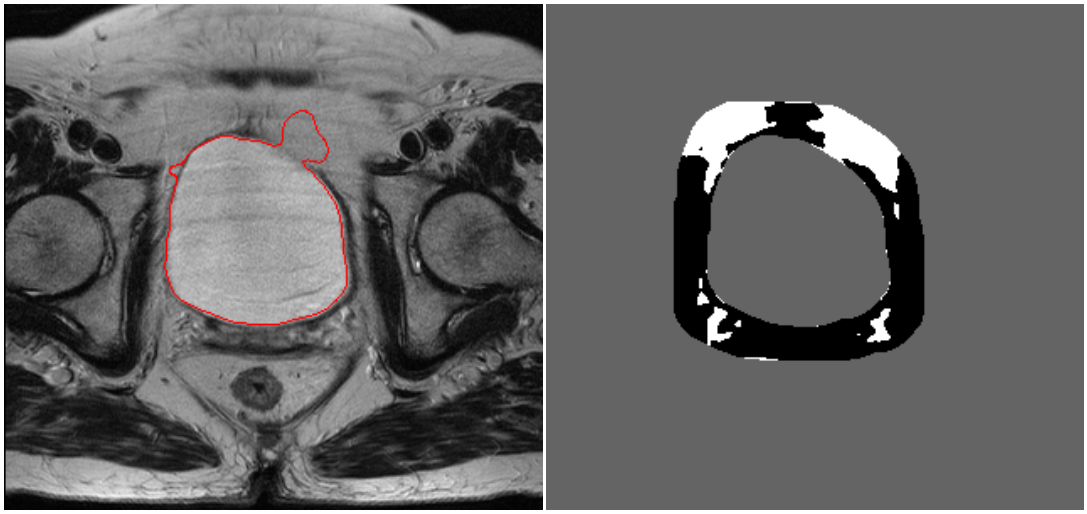

(a) (b)

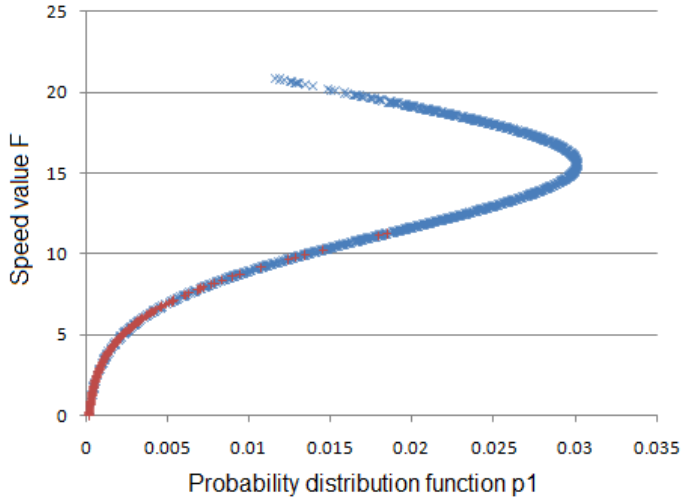

(c)

Figure 3: Leakage caused by the moving equation defined in Eq. (6): (a) the leaked contour; (b) the speed direction of a narrow band at the bladder boundary (in white: expanding regions, in black: retracting regions); (c) the scatter diagram of the pixels that are inside the neighboring band of the bladder boundary (r = 10), illustrating the relationship between the probability (horizontal axis) and the expanding speed values (vertical axis), with blue (red) marker stands for the pixels inside (outside) the boundary.

Compared with Eq. (3), the condition of the maximum operator requiring the competing contours to be close enough is discarded, and the first term is multiplied by the probability p_1 . As $p_1\left(e_1 - \max\left(e_2, e_3, e_1 - 1\right)\right) \to 0$ when $p_1 \to 0$, the multiplication guarantees that the contour will slow down when the contour arrives at the desired boundary where p_1 becomes small. In the maximum operator, the term $e_1 - 1$ is used, but has a different role to the one in Eq. (3): its function in Eq. (7) is to keep the expanding speed between 0 (zero) and 1 (one) so as to facilitate the parameter selection and make the contour movement stable. The second term

$\nabla p_1 \cdot \nabla \phi_1$ can attach the moving contour to the structure boundary, which was derived from $\nabla g \cdot \nabla \phi_1$ in the geodesic active contours by replacing the gradient-based function $g(I)$ with the region-based probability function $p_1(I)$. The replacement makes the calculation not only related to the neighboring pixels, but also with the intensity statistics of the whole bladder region. Therefore, the movement becomes less sensitive to intensity variations.

3.2 Vagina and rectum

When the images are severely influenced by noise, the vagina and the rectum cannot be segmented correctly only based on their imaging appearances. As such, shape guidance is critical for the segmentation of the two organs. In fact, a shape constraint can help the moving contours pass the unwanted inner boundaries and can also avoid leakages across the correct boundaries.

However, in a patient-specific study the prior shape knowledge of the vagina and the rectum is not always available before segmentation. Besides, the large shape variations of the two pelvic organs among individuals are significant obstacles for obtaining the prior shape information. These features imply that advanced techniques for incorporating prior shape constraints are not suitable for this application. In the segmentation of the vagina and the rectum, the algorithm introduced in Section 2.2.2 was adopted, which is a simple and straightforward way to incorporate a shape constraint. It should be noted that, even if the prior shape is not accurate, the force based on the shape constraint can help the contours pass the unwanted inner boundaries and avoid leakages.

3.2.1 Vagina

The appearance of the vagina can be easily distorted by noise, and the different layers have distinct appearances in T2-weighted MR images. Hence, besides handling the noise influence, the external forces should assure the bypass of the unwanted inner boundaries and drive the contour to the outer boundary.

As the shape of the vagina normally does not exhibit dynamic changes in the axial plane among the same image series, prior shape knowledge can be integrated to assist the segmentation. Meanwhile, given the different appearances between the organs and the surrounding tissues, the moving equation to segment the vagina is proposed as:

$$\frac{\partial \phi_2}{\partial t} = \delta(\phi_2)\left(p_2\left(e_2 - \max\left(e_1, e_3, e_2 - 1\right)\right) + \beta S_v + \gamma_2 \mathrm{div}\left(\frac{\nabla \phi_2}{|\nabla \phi_2|}\right)\right), \tag{8}$$

where δ, p_2, e_1, e_2, and e_3 are defined in Eq. (7), β is the weight to control the influence of the shape constraint, γ_2 is the weight used to control the effect of curvature in order to smooth the moving contour, and:

$$S_v = -\left(H\left(\phi_2(x)\right) - H\left(\phi_v\left(x - \mu_{\phi_2}\right)\right)\right) -$$

$$\frac{\left(x - \mu_{\phi_2}\right)^T}{\int H(\phi_2)\,dx} \times \int \left(H\left(\phi_2(x')\right) - H\left(\phi_v\left(x' - \mu_{\phi_2}\right)\right)\right)\delta\left(\phi_2(x')\right)\nabla\phi_2(x')\,dx'$$

with the level set function ϕ_v representing the prior shape of the vagina, and the remaining items defined the same as in Eq. (4).

In order to avoid possible leakage, the first term is multiplied by the probability p_2; also the additional term $e_2 - 1$ in the maximum operator is used to keep the movement stable. The final status of the moving contour by Eq. (8) is determined by two forces: one is from the imaging appearance and the other is from the prior shape knowledge. The guidance provided by the prior shape is necessary to obtain the correct boundary when the appearance of the vagina is interrupted by noise or when the multiple layers are clearly presented in the images.

Due to the distinct appearances of the layers, the mean intensity u_2 and the standard deviation σ_2 of the vagina region should be calculated carefully. Otherwise, the values may become larger due to the high signal intensity of the central strip, which can confuse the appearance comparison and lead to incorrect segmentation results. To solve this problem, the initial contours should be placed inside the vagina wall so that the possible bright central strip of the vagina will not be covered; and u_2 and σ_2 are calculated in the subset of Ω_2 defined as:

$$\Omega_2^* = \Omega_2 \cap \left\{(x, y) \middle| p_2(x, y) > p_1(x, y), p_3(x, y)\right\}. \tag{9}$$

This subset Ω_2^* excludes the high signal intensity pixels of the vaginal canal and the secretion. Hence, possible confusions caused by the miscalculation of the intensity statistics can be avoided.

3.2.2 Rectum

Like the vagina, the different layers of the rectum can be identified in T2-weighted MR images; therefore, the segmentation algorithm should handle the inhomogeneous intensities and assure the bypass of the inner rectal wall. The moving equation is then proposed as:

$$\frac{\partial \phi_3}{\partial t} = \delta(\phi_3)\left(\max(p_2, p_3) \cdot \left(e_3 - \max(e_1, e_3 - 1)\right) + \nu S_r + \gamma_3 \mathrm{div}\left(\frac{\nabla \phi_3}{|\nabla \phi_3|}\right)\right), \tag{10}$$

where δ, e_1, e_3, p_2, and p_3 are defined the same as in Eq. (7), ν and γ_3 are the weights with the same function as β and γ_2 in Eq. (8), and:

$$S_r = -\left(H(\phi_3(x)) - H\left(\phi_r\left(x - \mu_{\phi_3}\right)\right)\right) -$$
$$\frac{\left(x - \mu_{\phi_3}\right)^T}{\int H(\phi_3)\,dx} \times \int \left(H(\phi_3(x')) - H\left(\phi_r\left(x' - \mu_{\phi_3}\right)\right)\right) \delta(\phi_3(x')) \nabla \phi_3(x')\,dx',$$

with the level set function ϕ_r representing the prior shape of the rectum.

Due to the similar appearance between the rectal lumen and the vaginal wall, the terms in the maximum operator are changed to $\max(e_1, e_3 - 1)$. Therefore, the comparison is only between the bladder and the rectum. To avoid leakage the first term is multiplied by $\max(p_2, p_3)$, instead of p_3, so that the contour will not stop at the rectal lumen where p_3 is small but p_2 is large. Compared with the bladder, the appearance of the rectal lumen is more similar to the rectal wall. Hence, the contour can pass the inner boundary according to Eq. (10).

Likewise, due to the distinct appearances of the layers, most parts of the initial contour should be placed inside the rectal wall, and the mean intensity u_3 and the intensity standard deviation σ_3 are calculated in the subset of Ω_3 defined as:

$$\Omega_3^* = \Omega_3 \cap \left\{(x, y) \middle| p_3(x, y) > p_1(x, y), p_2(x, y)\right\}. \tag{11}$$

The subset Ω_3 excludes the pixels of the rectal lumen, and therefore avoids the possible confusions caused by the similar appearances between the rectal lumen and the vaginal wall. Otherwise, the mean intensity u_3 of the rectum can be close to the mean intensity u_2 of the vagina, which may affect the appearance comparison and lead to an incorrect segmentation.

3.3 Parameters and external forces

Initial contours should be placed well inside the boundary of each organ as aforementioned. Their locations can influence the final segmentation results, and the incorrect appearance comparison may lead to wrong segmentations: for the bladder, the initial contours should avoid the highly inhomogeneous regions; for the vagina and the rectum, the initial contours should be placed so that their major parts are outside the vaginal canal and the rectal lumen.

The parameters γ_i with $i = 1, 2, 3$ in the moving equations control the influence of the internal forces and a larger value can lead to a smoother boundary; the parameter α is the weight of the gradient field of the probability that helps to accelerate the contour movement and prevent leakage. Compared with the weights of the shape constraint, the four parameters only have minor influences on the segmentation results and can be selected easily and fixed when handling image series.

Given that the final boundaries are obtained under two external forces, the prior shape does not need to be accurate. With an inaccurate prior shape, the force derived by the prior shape energy can make the contour pass the possible local boundaries caused by noise or intensity variation. Then, once the boundaries in an image are correctly segmented, they are used as the prior shapes for the sequential slices, and the prior shape can be refined by averaging the obtained contours as suggested in [32]. The two external forces derived by the prior shape and the appearance comparison need to be well balanced. As the pelvic organs have normal shape variations in different slices, the main external force is the one derived from the appearance comparison. Hence, the influence of the appearance force is normally larger than the influence of the shape force. Nevertheless, if the images are severely distorted by noise or PVE, the shape force should be increased so that the moving contours are guided to the correct boundary. Therefore, the values of the weights β and ν are related to the image quality.

When the prior shapes of the vagina and rectum are unavailable, a rectangle is used as an approximate shape of the vagina and a circle for the rectum on the axial MR images. Then once the boundaries in an image are segmented correctly, they can be used as the prior shapes to assist the segmentation of the sequential slices; also, the approximate prior shapes can be refined by averaging the obtained contours as suggested in [32].

3.4 Intensity statistics

The mean intensity values and the intensity variance of the three organs are updated when the contours move forward. In the beginning phase, these values are obtained from local areas and may deviate from the true values. The imprecision can lead to miscalculation of the probability and cause dynamic changes of the speed function, which may affect the contour movement and lead to wrong results. To avoid this, the standard deviation is computed as $\sigma_i = \max(\sigma_i, \sigma_0)$, with $i = 1,2,3$, where σ_0 is a predefined value. Then, if σ_1 , σ_2, and σ_3 are smaller than σ_0, the intensity standard deviation of each region is assumed to be equal. The appearance comparison in the proposed approach is to compare the magnitude of $|I - u_i|$, with $i = 1,2,3$, which is the difference between the intensity of a pixel and the mean intensity of each region, a similar segmentation path as used in the k-means algorithm [35]. The value of σ_0 is also related to the image qualities; a larger σ_0 means a wider range in which the intensities of the pelvic organs are allowed to vary. The modification makes the segmentation less sensitive to the initial conditions and more flexible to handle the inhomogeneous intensities.

However, since the sizes and dimensions of the three pelvic organs are not equal, sometimes one or two organs are not visible on the images. In this case, since the coupling information between the moving contours is only the intensity statistics, the strategy adopted was that once an image is successfully segmented, the intensity statistics of each organ are stored. As such, if one or two organs are missing in the neighboring images, the stored statistical information is used.

3.5 Outline of the novel approach

The coupling approach changed the region competition algorithm in [20] into a new algorithm that can handle the segmentation of local image regions with the assistance of prior shape constraints. To conclude, the proposed approach integrates the three geometric deformable models:

$$\begin{cases} \dfrac{\partial \phi_1}{\partial t} = \delta(\phi_1)\left(p_1\left(e_1 - \max\left(e_2, e_3, e_1 - 1\right)\right) + \alpha \nabla p_1 \cdot \nabla \phi_1 + \gamma_1 \mathrm{div}\left(\dfrac{\nabla \phi_1}{|\nabla \phi_1|}\right)\right) \\ \dfrac{\partial \phi_2}{\partial t} = \delta(\phi_2)\left(p_2\left(e_2 - \max\left(e_1, e_3, e_2 - 1\right)\right) + \beta S_v + \gamma_2 \mathrm{div}\left(\dfrac{\nabla \phi_2}{|\nabla \phi_2|}\right)\right) \\ \dfrac{\partial \phi_3}{\partial t} = \delta(\phi_3)\left(\max\left(p_2, p_3\right) \cdot \left(e_3 - \max\left(e_1, e_3 - 1\right)\right) + \nu S_r + \gamma_3 \mathrm{div}\left(\dfrac{\nabla \phi_3}{|\nabla \phi_3|}\right)\right) \end{cases}, \quad (12)$$

where the level set function ϕ_1 is for the bladder, ϕ_2 is for the vagina and ϕ_3 is for the rectum. To further decrease the influence of noise, the intensity of a pixel $I(X_0)$ is changed to the average intensity of its *m*-connected neighbor set $N_m(X_0)$ as $\overline{I}(X_0) = \frac{1}{|N_m(X_0)|}\sum_{X \in N_m(X_0)} I(X)$; or one can choose to replace the probability $p_i(X_0)$ with the joint probability $\prod_{X \in N_m(X_0)} p_i(X)$ as in [30]. The initial contours need to be correctly defined inside the organ regions as stated above.

The proposed procedure can be summarized into the following three steps, with the application of the narrow band method [34] to improve the computational efficiency:

0. *Preprocessing*: Smooth the input image using a Gaussian kernel.

1. *Initialization:* Set $t = 0$, define the initial contours inside the organ regions and

(a) Build the level set functions ϕ_v and ϕ_r for the prior shape of the vagina and the rectum;

(b) For each organ, define a narrow band around each initial contour; and initialize the level set functions $\phi_i(x, y, 0)$ using the signed distance function, with $i = 1, 2, 3$;

(c) Calculate the mean u and the standard deviation σ of the intensity distributions of the region Ω_1, Ω_2^* and Ω_3^*.

2. *Iteration*: Set $t = t + 1$, update the level set values according to Eq. (12). Then update the values of u and σ for each region.

3. *Judgment:* Check whether the contours have stopped moving or whether the iteration time has reached a maximum threshold $t > T_{threshold}$ (in this situation the contours are considered to have reached stability). If neither case is true, return to Step 2; otherwise, stop the iteration process.

4. Experiments

Two image series are used here to illustrate the performance of the proposed approach. One was acquired from a symptomatic 63-year-old multiparous woman under a turbo-spin echo (TSE) sequence with a field strength of 1.5 T, TE: 103 ms, TR: 5230 ms, and an acquisition matrix of 320×272. This axial image series contains 28 image slices, and the spatial resolution of the axial images is 0.69×0.69×5.40 mm3. The other image series was from an asymptomatic nulliparous 20-year-old woman under a TSE sequence with a field strength of 1.5 T, TE: 98 ms, TR: 3980 ms, and an acquisition matrix of 320×192. This axial image series contains 40 image slices, and the spatial resolution of the axial images is 1.00×1.00×5.400 mm3.

The two-image-data were chosen because they are suitably representative to show the imaging features of the three pelvic organs on the axial MR images. Figure 4 illustrates nine images of the two series; on these images the different shapes of the bladder at different imaging positions and between individuals can be clearly verified; the distinct layers of the vagina can be seen on the images acquired from the younger woman, and the different layers of the rectum can be seen better on the images from the older woman. A rectangle of the dimensions equal to 5×70 (pixel size) was used as the prior shape of the vagina and a circle with radius equal to 18 (pixel size) for the rectum in Figure 4. To evaluate the segmentation results, the ground truth was obtained through averaging the manual segmentations performed separately by three experienced technicians, as proposed in [32]. Then, the boundaries segmented by the proposed algorithms (red contours) were overlapped with the ground truth (green contours) so that the deviations could be clearly depicted.

Despite the presence of noise and the PVE, the bladders were correctly segmented by the proposed solution. In Figures 4(a)-(c), the central high signal intensity strip of the vagina is almost invisible and the whole vagina region appears as a thin band with a blurred boundary due to the PVE. On the other hand, by adopting the proposed external forces, the moving contour kept the integrity and arrived at the correct boundary. In Figures 4(d)-(f), the images are of the upper third of the vagina, near to the cervix, and this part is rounder and narrower in appearance than the lower two thirds. Although the prior shape used was not accurate, the correct boundaries can still be segmented. In Figures 4(g)-(i), the distinct layers of the vagina are observed more clearly; with the proposed solution, the moving contour passed the central high

intensity strip and successfully arrived at the outer boundary. Likewise, the layers of the rectum are easily observed in the images. The inner boundary that enclosed the rectal lumen was passed by, and the outer boundaries were correctly segmented.

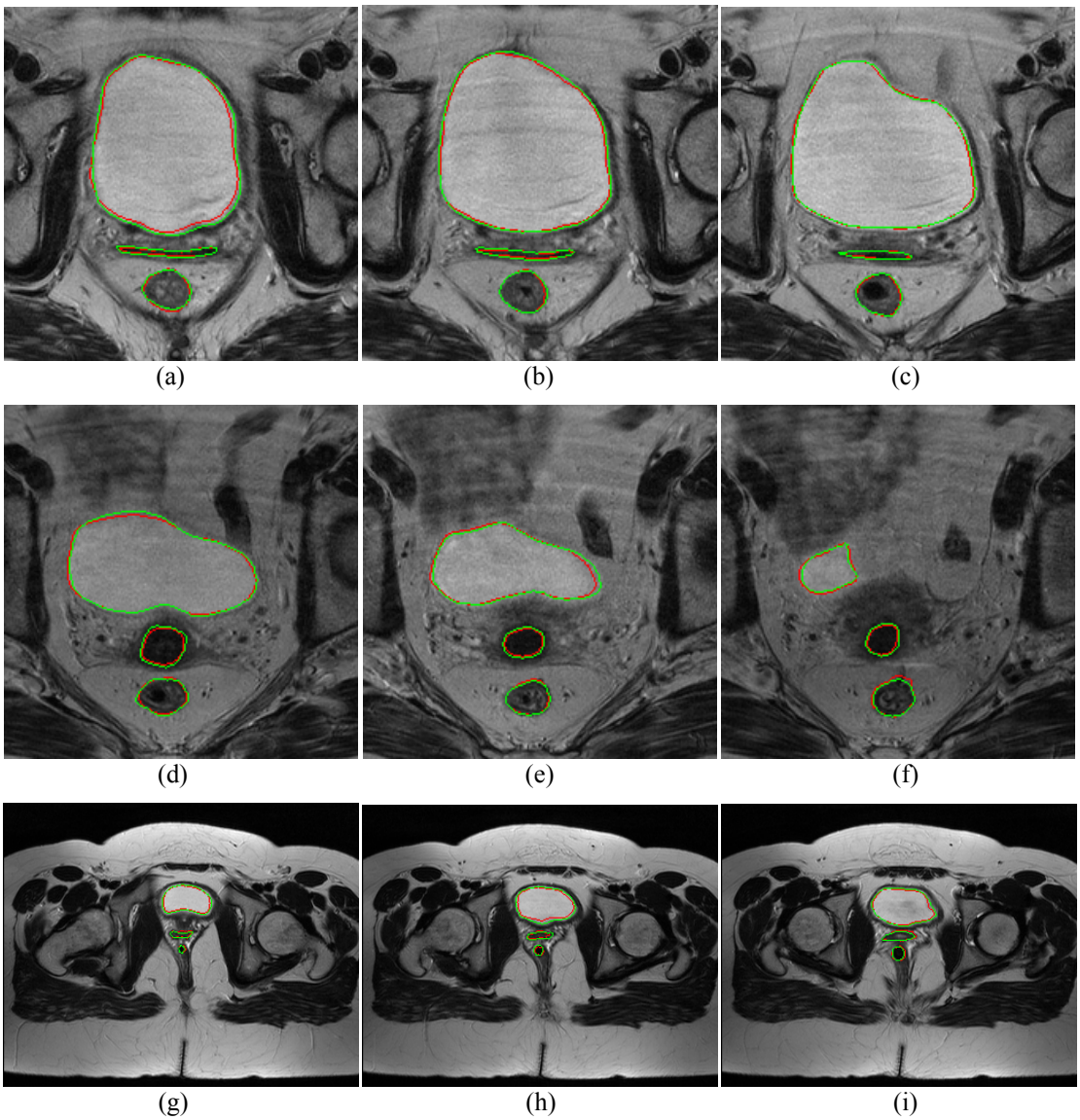

Figure 4: Segmentation results by the proposed approach (red contours) overlapped with the ground truth (green contours); from top to bottom, the organs segmented in each image are: bladder, vagina, and rectum. (Images from (a) to (f) are from the older woman and images from (g) to (i) are from the younger woman.)

To quantitatively evaluate the segmentation results, the Hausdorff distance was adopted. Supposing C_0 is the true boundary and C_1 is the contour segmented by the proposed algorithm, the Hausdorff distance is calculated as:

$$D(C_0, C_1) = \max\left(\max_{p \in C_0} D(p, C_1), \max_{p \in C_1} D(p, C_0)\right), \tag{13}$$

where the point-to-contour distance was defined as:

$$D(p,C)=\min_{p_1\in C} d(p,p_1), \tag{14}$$

and $d(p,p_1)$ is the Euclid distance between two points.

In addition, a measure similar to the average symmetric absolute distance error was used to check the overall point-to-point matching between the two contours:

$$AD(C_0,C_1)=\left(MD(p,C_0)+MD(p,C_1)\right)/2, \tag{15}$$

where $MD(p,C_0)$ is the average value of the distances $D(p,C_0)$ for point $p\in C_0$ and $MD(p,C_1)$ is the average value of the distances $D(p,C_1)$ for point $p\in C_1$.

Table 1 Comparison between the boundaries segmented by the proposed algorithms and the ground truth (HD: Hausdorff distance; AD: the average symmetric absolute surface distance defined in Eq. (15))

Figure 4	Bladder		Vagina		Rectum	
	HD (mm)	AD (mm)	HD (mm)	AD (mm)	HD (mm)	AD (mm)
a	2.48	1.02	1.54	0.39	1.38	0.52
b	1.54	0.66	1.54	0.45	1.38	0.32
c	1.38	0.39	0.69	0.21	0.69	0.37
d	2.06	0.54	1.54	0.83	1.54	0.51
e	2.48	0.64	0.97	0.72	0.97	0.35
f	1.38	0.66	1.38	0.70	1.94	0.57
g	2.00	0.86	2.00	0.66	1.00	0.40
h	3.61	1.51	3.00	0.90	2.00	0.78
i	2.83	0.90	2.24	0.57	1.41	0.62

Table 1 shows the comparison of the results of the images illustrated in Figure 4. Considering the imaging resolution, the average deviation from the ground truth is around 1 to 2 pixels. The average Hausdorff distance and the average symmetric distance for the illustrated two image series are shown in Table 2.

As can be seen from the illustrated images, the three novel coupling geometric deformable models handle the influences of noise and PVE successfully. The obtained boundaries are promising both qualitatively and quantitatively.

Table 2 Average values of the metrics for the illustrated two image series (HD: Hausdorff distance; AD: the average symmetric absolute surface distance defined in Eq. (15))

Series	Bladder		Vagina		Rectum	
	HD (mm)	AD (mm)	HD (mm)	AD (mm)	HD (mm)	AD (mm)
1	1.93	0.61	1.32	0.52	1.16	0.38
2	2.72	1.00	2.05	0.59	1.28	0.50

As an illustration, Table 3 presents the intensity statistics of the three pelvic organs in the images of Figure 4, from which one can see the large variances in the vagina and rectum due to their different layers. The values listed in parentheses are the ones calculated in the subset Ω_2^* and Ω_3^* defined in Eqs. (9) and (11) respectively; the differences between the values verifies the different intensity distribution of each organ, and also show the reason why the u_i and σ_i, $i = 2,3$ should be calculated on the subsets.

Table 3 The mean and standard deviation of the intensity in Figure 4 (SD: standard deviation, the values in parentheses were obtained by the proposed solution)

Figure 4	Bladder		Vagina		Rectum	
	Mean	SD	Mean	SD	Mean	SD
a	163.1	16.3	44.5 (40.9)	16.2 (9.1)	77.5 (77.7)	18.1 (13.2)
b	165.2	16.5	46.2 (41.6)	15.2 (6.9)	66.5 (69.1)	19.1 (17.7)
c	175.0	12.5	41.4 (40.1)	15.4 (9.8)	57.3 (65.4)	25.8 (16.3)
d	129.9	10.3	22.0 (21.2)	7.0 (4.5)	46.0 (47.0)	19.8 (17.2)
e	148.3	12.0	21.6 (21.1)	6.0 (3.5)	51.6 (55.1)	17.8 (15.1)
f	132.3	10.3	19.9 (19.2)	5.8 (3.6)	52.7 (43.7)	15.4 (11.4)
g	190.8	10.1	41.9 (43.8)	12.5 (6.0)	23.2 (28.1)	13.7 (12.0)
h	175.2	17.4	39.3 (39.8)	12.0 (5.4)	22.2 (15.0)	26.8 (10.2)
i	168.3	15.5	49.8 (53.9)	17.0 (14.5)	16.8 (11.7)	16.0 (3.9)

5. Conclusion

The novel geometric deformable models proposed in this paper can effectively handle the segmentation of pelvic organs in axial T2-weighted MR images. The different appearances between the organs and the prior shape knowledge are incorporated into a level set framework. The coupling between the moving contours is achieved through the intensity statistics of the three pelvic organs. The three pelvic organs can be segmented simultaneously and, with shape guidance, the approach is less sensitive to the influence of noise and partial volume effect.

The satisfactory performance of the coupling approach is based on the premises that the initial contours are properly defined, the acquired MR image data are not severely influenced by noise or partial volume effect, and the shapes of the vagina and the rectum are not seriously deformed due to specific conditions. Therefore, the proposed computational approach may not be fully satisfactory in some cases; for example, when the pelvic organs have suffered considerable deformations due to injuries or when their appearances are severely distorted by noise. In addition, one

may notice that the suggested solution requires that the three organs appear together in the input image. When this does not occur, statistical information from the processed images can be used, but the performance of the approach may be affected.
As the proposed approach is based on deformable models, the parameters should be selected suitable. Nevertheless, a fully automatic segmentation approach will be an even more valuable tool for medical applications, such as pelvic radiotherapy [36]. Hence, the future work aims to enhance the robustness and automation of the proposed approach and for that, the integration of available anatomical statistics, such as incorporating the distance between different structures or the anatomical atlas can be a potential solution. Also, algorithms that correct the inhomogeneity on MR images, such as the ones in [37, 38], can be potential ways to improve the performance and robustness of the segmentation and help to facilitate the parameter selection.

Conflict of interest statement

None Declared.

Acknowledgements

This work was partially done in the scope of the projects “Methodologies to Analyze Organs from Complex Medical Images – Applications to Female Pelvic Cavity”, “Aberrant Crypt Foci and Human Colorectal Polyps: mathematical modeling and endoscopic image processing” and “Cardiovascular Imaging Modeling and Simulation - SIMCARD”, with references PTDC/EEA-CRO/103320/2008, UTAustin/MAT/0009/2008 and UTAustin/CA/0047/2008, respectively, financially supported by Fundação para a Ciência e a Tecnologia (FCT), in Portugal.

The first author would like to thank FCT for his PhD grant with reference SFRH/BD/43768/2008.

References

[1] Handa VL, Harris TA, Ostergard DR. 1996. Protecting the pelvic floor: obstetric management to prevent incontinence and pelvic organ prolapse. Obstet Gynecol. 88(3):470-478.

[2] Buchsbaum GM, Duecy EE, Kerr LA, Huang LS, Guzick DS. 2005. Urinary incontinence in nulliparous women and their parous sisters. Obstet Gynecol. 106(6):1253-1258.

[3] Hutchinson E. 2010. Constipation and the pelvic floor. Nat Rev Gastroenterol Hepatol. 7(4):185-185.

[4] Fantl JA, Newman DK, Colling, J. et al. 1996. Urinary incontinence in adults: acute and chronic management. Clinical Practice Guideline, Clinical Practice Guideline, Rockville (MD): Agency for Health Care Policy and Research. Public Health Service, U.S. Department of Health and Human Services, No. 2.

[5] Olsen AL, Smith VJ, Bergstrom JO, Colling JC, Clark AL. 1997. Epidemiology of surgically managed pelvic organ prolapse and urinary incontinence. Obstet Gynecol. 89(4):501-506.

[6] Herschorn S. 2004. Female pelvic floor anatomy: the pelvic floor, supporting structures, and pelvic organs. Rev Urol. 6(Suppl 5):S2-S10.

[7] Margulies RU, Hsu Y, Kearney R, Stein T, Umek WH, DeLancey JO. 2006. Appearance of the levator ani muscle subdivisions in magnetic resonance images. Obstet Gynecol. 107(5):1064-1069.

[8] Paramasivam S, Proietto A, Puvaneswary M. 2006. Pelvic anatomy and MRI. Best Pract Res Cl Ob. 20(1):3-22.

[9] Klessen C, Rogalla P, Taupitz M. 2007. Local staging of rectal cancer: the current role of MRI. Eur Radiol. 17(2):379-389.

[10] Noakes KF, Bissett IP, Pullan AJ, Cheng LK. 2008. Anatomically realistic three-dimensional meshes of the pelvic floor & anal canal for finite element analysis. Ann Biomed Eng. 36(6):1060-1071.

[11] Alexandre F, El Sayed R, Mascarenhas T, Jorge RNM, Parente MP, Fernandes AA, Tavares JMRS. 3D reconstruction of pelvic floor for numerical simulation purpose. 1st ECCOMAS Thematic Conference on Computational Vision and Medical Image Processing, Porto, Portugal, October 2007, pp. 359-362.

[12] Collier DC, Burnett SS, Amin M, Bilton S, Brooks C, Ryan A, Roniger D, Tran D, Starkschall G. 2003. Assessment of consistency in contouring of normal-tissue anatomic structures. J Appl Clin Med Phys. 4(1):17-24.

[13] Ma Z, Tavares JMRS, Jorge RNM, Mascarenhas T. 2010. A review of algorithms for medical image segmentation and their applications to the female pelvic cavity. Comput Method Biomec. 13(2):235-246.

[14] Ma Z, Jorge RMN, Tavares JMRS. 2010. A shape guided C–V model to segment the levator ani muscle in axial magnetic resonance images. Med Eng Phys. 32(7):766-774.

[15] Rousson M, Khamene A, Diallo M, Celi JC, Sauer F. Constrained surface evolutions for prostate and bladder segmentation in CT images. Lecture Notes in Computer Science, 2005, Volume 3765/2005, pp. 251-260.

[16] Pasquier D, Lacornerie T, Vermandel M, Rousseau J, Lartigau E, Betrouni N. 2007. Automatic segmentation of pelvic structures from magnetic resonance images for prostate cancer radiotherapy. Int J Radiat Oncol. 68(2):592-600.

[17] Duan C, Liang Z, Bao S, Zhu H, Wang S, Zhang G, Chen J, Lu H. 2010. A coupled level set framework for bladder wall segmentation with application to MR cystography. IEEE T Med Imaging. 29(3):903-915.

[18] Joshi N, Bond S, Brady M. 2010. The segmentation of colorectal MRI images. Med Image Anal. 14(4):494-509.

[19] Adams R, Bischof L. 1994. Seeded region growing. IEEE T Pattern Anal. 16(6):641-647.

[20] Brox T, Weickert J. 2006. Level set segmentation with multiple regions. IEEE T Image Process. 15(10):3213-3218.

[21] Cremers D, Osher SJ, Soatto S. 2006. Kernel density estimation and intrinsic alignment for shape priors in level set segmentation. Int J Comput Vision. 69(3):335-351.

[22] Moore KL, Dalley AF. Clinically Oriented Anatomy, 4th ed., Lippincott Williams & Wilkins, Baltimore, 1999.

[23] Barnhart KT, Izquierdo A, Pretorius ES, Shera DM, Shabbout M, Shaunik A. 2006. Baseline dimensions of the human vagina. Hum Reprod. 21(6):1618-1622.

[24] Zaspel U, Hamm B. Vagina, in: B. Hamm, R. Forstner (Eds.), MRI and CT of the Female Pelvis, Springer, Berlin Heidelberg New York, 2007.

[25] Caselles V, Kimmel R, Sapiro G. 1997. Geodesic active contours. Int J Comput Vision. 22(1):61-79.

[26] Osher SJ, Sethian JA. 1998. Fronts propagating with curvature-dependent speed: algorithms based on Hamilton-Jacobi formulations. J Comput Phys. 79(1):12-49.

[27] McInerney T, Terzopoulos D. 1996. Deformable models in medical image analysis: a survey. Med Image Anal. 1(2):91-108.

[28] Niessen WJ, ter Haar Romeny BM, Viergever MA. 1998. Geodesic deformable models for medical image analysis. IEEE T Med Imaging. 17(4):634-641.

[29] Pham DL, Xu C, Prince JL. 2000. A survey of current methods in medical image segmentation. Ann Rev Biomed Eng. 2:315-338.

[30] Zhu SC, Yuille A. 1996. Region competition: unifying snakes, region growing, and Bayes/MDL for multiband image segmentation. IEEE T Pattern Anal. 18(9):884-900.

[31] Leclerc YG. 1989. Constructing simple stable descriptions for image partitioning. Int J Comput Vision. 3(1):73-102.

[32] Leventon ME, Grimson WEL, Faugeras O. Statistical shape influence in geodesic active contours, in: Proceedings of the 2000 IEEE Conference on Computer Vision and Pattern Recognition, IEEE Computer Society, South Carolina, USA, 2000, pp. 316-323.

[33] Riklin-Raviv T, Kiryati N, Sochen N, Unlevel-sets: geometry and prior-based segmentation, in: T. Pajdla, J. Matas (Eds.), Proceedings of 8th European Conference on Computer Vision, 3024, Springer, Berlin Heidelberg, New York, 2004, pp. 50-61.

[34] Adalsteinsson D, Sethian JA. 1995. A fast level set method for propagating interfaces. J Comput Phys. 118(2):269-277.

[35] Lloyd S. 1982. Least squares quantization in PCM. IEEE T Inform Theory. 28(2):129-137.

[36] Haas B, Coradi T, Scholz M, Kunz P, Huber M, Oppitz U, André L, Lengkeek V, Huyskens D, van Esch A, Reddick R. 2008. Automatic segmentation of thoracic and pelvic CT images for radiotherapy planning using implicit anatomic knowledge and organ-specific segmentation strategies. Phys Med Biol. 53(6):1751-1771.

[37] Bagci U, Udupa JK, Bai L. 2010. The role of intensity standardization in medical image registration. Pattern Recogn Lett. 31(4):315-323.

[38] Madabhushi A, Udupa JK. 2005. Interplay between intensity standardization and inhomogeneity correction in MR image processing. IEEE T Med Imaging. 24(5):561-576.

Part B – Article 3

A Shape Guided C-V Model to Segment the Levator Ani Muscle in Axial Magnetic Resonance Images

Zhen Ma, Renato Natal Jorge, João Manuel R. S. Tavares

Published in: Medical Engineering & Physics, 32(7): 766-774, 2010.

Abstract

This paper proposes a modified Chan-Vese model to segment levator ani muscles from axial magnetic resonance (MR) images. Intensity variances of the foreground and the background are used as the main segmentation clues. As in most cases the boundary of the rectum can be successfully segmented in axial MR images, it is assumed as a *priori* and is used to define the region of interest and the initial contour. In order to handle the complex influences of the connective tissues, a shape influence field is formed based on the shape information of the rectum and is integrated into the Chan-Vese model. Several segmentation examples are presented to show the effectiveness of the proposed method and the necessity of adding the shape influences.

Keywords: Image Segmentation; Deformable Model; Shape Influence Field; Medical Imaging; Pelvic Cavity; Pelvic Floor.

1. Introduction

Pelvic floor disorders are highly prevalent diseases that affect women of different ages. For example, it is estimated that 30 - 50% of women in Europe and the USA are affected by urinary incontinence [1]; about 11% - 15% of the population in New Zealand and 2.2 - 6.9% of population in the USA suffer from fecal incontinence [2-4]. However, a real understanding of the pathophysiology of pelvic floor disorders is still lacking. It seems that a clinical condition develops through a combination of various factors. Findings of epidemiologic studies, which are not designed to prove cause and affect relationships, are frequently inconsistent. Without an understanding of the true causes of pelvic floor disorders, efforts at prevention are futile and therapy can only be empiric, rather than directed at specific injuries or functional deficits. Unfortunately, surgery for pelvic floor disorders often fails. The organs and muscles of the pelvic floor have complex three-dimensional (3D) structures and interact in a complicated fashion to maintain continence. When they do not function properly, incontinence or prolapse occurs. Therefore, a thorough understanding of the physiological and biological functions of the pelvic floor is urgently needed from a

health and social point of view. In order to achieve this, precise geometrical 2D and 3D models are needed [5].

The first process to be carried out on the acquired image data is to sketch the organs presented in each 2D image slice. A correct segmentation of the levator ani muscles in each image slice is critical for the study of biomechanical behavior or medical diagnosis [6-8] later on. The levator ani is a broad thin muscle situated in the pelvic cavity and forms the main part of the pelvic floor. The main functions of levator ani are to give support to the pelvic viscera, maintain the anorectal angle, and control the evacuation of the urinary bladder and rectum. Anatomically, the levator ani is composed of iliococcygeus, pubococcygeus and puborectalis muscles [9]. Magnetic resonance imaging (MRI) is often a preferred imaging modality to study the levator ani muscles, because it can provide clearer views on the soft tissues when compared to other non-invasive modalities. However, it is often hard to identify the levator ani muscles due to the influence of noise and partial volume effect. Consequently, segmentation still relies on manual operations by trained medical technicians. In order to improve the time efficiency and decrease the intra-observer or inter-observer errors, an effective computer-aided algorithm is urgently demanded.

Deformable models are effective image segmentation techniques that have been intensively studied for medical image processing and analysis. Flexibility makes deformable models suitable for concrete applications [10]. In this paper, we propose a novel method to segment the levator ani muscles, based on the use of deformable models with topology preservation and a *priori* knowledge. The proposed method presents promising results. As far as the authors know, this is among the first automatic approaches to segment the levator ani muscles from 2D magnetic resonance images.

The paper is organized as follows: in Section 2, the features of the levator ani muscle are summarized and the Chan-Vese model is reviewed; in Section 3, the new method is introduced, through the definition of the region of interest (ROI) to be used in the segmentation process, the topology preservation constraint and the shape influence field; in Section 4, segmentation examples are shown and analyzed; and finally, we present the main conclusions.

2. Background review

2.1 Anatomical knowledge

To begin the introduction of the proposed algorithm, it is necessary to point out the main anatomical characteristics of the levator ani. The real-time status of this set of muscles is driven by the related physiological processes. For example, the contraction of the levator ani may be caused by the evacuation of bladder or rectum. Therefore, the shape of the levator ani has a direct relationship with the status of organs it supports. In our study, the axial MRI was chosen as the imaging modality because the pelvic floor is easier to be anatomically identified in this plane [11]. In the axial MR images, the appearances of the levator ani muscles are broad and thin with large variations on the thickness and the length in different positions. The three components are usually sketched together as illustrated in Figure 1. From this image, one can also see in the axial plane the arch-shaped boundary of the levator ani situated below the pelvic organs and surrounding the rectum.

From the view of image processing, the boundary of the levator ani is ill-defined, because the partial volume effect may confuse the appearances of the levator ani with other structures such as fats or connective tissues. In some cases, the levator ani may appear as discrete pixel clusters. These features make it hard to carry out a correct automatic or even manual segmentation. To keep the integrity of the boundary, the threshold-based algorithms such as edge detection or region growing algorithm may not be applicable [10]. Meanwhile, due to childbirth, age and physical training, or pathologies, such as urinary incontinence and genital prolapse, some of the main dimensions of the pelvic floor can vary significantly from patient to patient [12,13]. The large shape variation is an obstacle for algorithms that use the supervised or unsupervised learning techniques such as the active shape model [14] or the active appearance model [15].

Application of the current algorithms to segment the pelvic floor in MR images has been discussed in [10], from which the problems with the segmentation results can be classified into two aspects: incompleteness or leakage. The incompleteness of the boundary is related with the definition of the initial conditions or the regularizing effects by the internal forces; while the leakage of boundary is mainly caused by noise or partial volume effect that tends to confuse the appearances of the levator ani with other structures. Therefore, the boundary cannot be identified barely through gradient

information or the image appearances. Hence, an effective algorithm should handle the two aspects simultaneously.

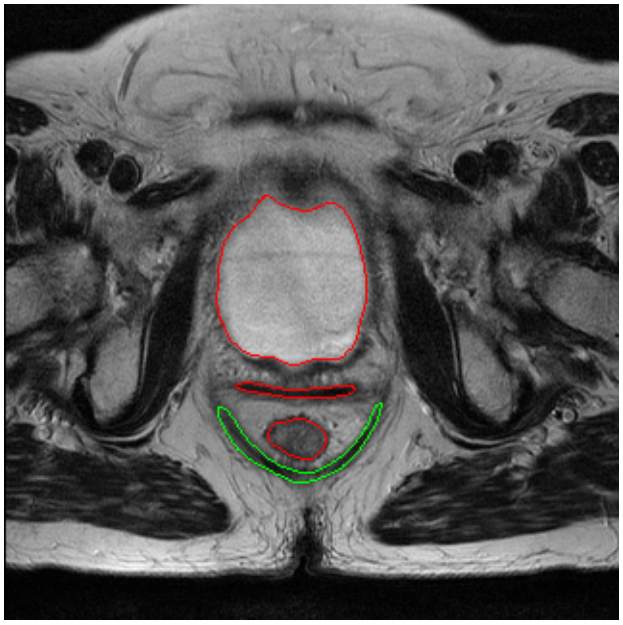

Figure 1: Axial view of pelvic cavity with the boundaries of different structures; from up to down: bladder, vagina, rectum, and the levator ani muscle.

Compared with other segmentation techniques, deformable models are flexible to be used for fulfilling a concrete requirement and *priori* knowledge can easily be incorporated to improve their performance [10]. Deformable models can be divided into parametric and geometric models. The difference depends on their ways of tracking: parametric models explicitly follow the movement of each sampled contour point, while geometric models implicitly embed the contour to a higher dimensional function and track its zero level set. Parametric models have higher computational efficiency, but may also have higher computational complexity due to the processes such as re-sampling or handling topological changes; geometric deformable models can naturally handle topological changes and have low computational complexity, especially when the moving equation is related to the calculation of geometric properties of the contour [10]. Both types have wide applications in the area of medical image processing. The selection of the model to be used depends on concrete requirements. We chose the geometric deformable model because of its simple computational complexity. The Chan-Vese model [16] was chosen as our base model because its characteristics meet several requirements of our application. Following, we review the level set method and then the Chan-Vese model.

2.2 Level set method

The geometric models are based on the application of the level set method, which was initially proposed to handle the topological changes during the curve evolution [17]. The main idea of the level set method is to add a time variable to the contour representation and implicitly embed the moving contour into the zero level set of the higher dimensional level set function. Then, instead of tracking the contour points, one can track the zero level set of the level set function. The implicit embedding can naturally handle the topological changes. Also, using the implicit representation, the geometric properties of the contour, such as curvature and normal vector, can be calculated easily. And so, the computational complexity is considerably decreased. A typical level set equation in the 2D plane is:

$$\phi_t + F\left|\nabla\phi\right| = 0\,, \tag{1}$$

$$\phi(x, y, 0) = 0\,,\ (x, y) \in L_0 \tag{2}$$

where ϕ is the level set function; F is the speed function and L_0 represents the initial contour. To apply the level set method to the image processing requires a proper defined speed function so that the stable status of the moving contour corresponds to the boundary of the desired structure. There are two ways to define the speed function: one is to define it directly, like the algorithm proposed in [18]; the other is to derive it through energy functional, like in the geodesic active contour model (GAC) [19]. The geometric deformable models have simple computational complexity and are flexible to incorporate a *priori* knowledge.

2.3 Chan-Vese model

The Chan-Vese model (C-V model) is a geometric deformable model. The model does not use the information of image gradient, but instead uses the intensity variations of foreground and background as the segmentation clue. The energy functional of C-V model is defined as follows:

$$E = \mu \cdot \text{Length}(C) + \nu \cdot \text{Area}\left(inside(C)\right) + \lambda_1 \int_{inside(C)} \left|I(x, y) - c_1\right|^2 dxdy + \lambda_2 \int_{outside(C)} \left|I(x, y) - c_2\right|^2 dxdy \tag{3}$$

where C represents the moving contour; I is the intensity function; $\mu, \nu \geq 0$; $\lambda_1, \lambda_2 > 0$ are the weights of each corresponding item; c_1 and c_2 are the mean of intensity

values inside and outside the moving contour. The first two items are called the internal energy, which is used to regularize the geometric properties of the moving contour. The last two items are called the external energy, which is used to attract the contour to the correct position. Through the Euler-Lagrange equation of the functional, the moving equation is derived as:

$$\frac{\partial \phi}{\partial t} = \delta_\varepsilon(\phi)\left[\mu \cdot \mathrm{div}\left(\frac{\nabla \phi}{|\nabla \phi|}\right) - \nu - \lambda_1 \left(I(x,y) - c_1\right)^2 + \lambda_2 \left(I(x,y) - c_2\right)^2\right], \tag{4}$$

$$\phi(x,y,0) = \phi_0(x,y), \text{ in } \Omega, \tag{5}$$

$$\frac{\delta_\varepsilon(\phi)}{|\nabla \phi|}\frac{\partial \phi}{\partial \vec{n}} = 0, \text{ on } \partial\Omega \tag{6}$$

where δ is the Dirac function; $\partial\phi/\partial\vec{n}$ denotes the normal derivative of ϕ at the boundary; Ω is the image region. The average intensities c_1 and c_2 can be calculated as:

$$c_1 = \frac{\int_\Omega I(x,y) H\left(\phi(x,y)\right) dxdy}{\int_\Omega H\left(\phi(x,y)\right) dxdy}, \text{ if } \int_\Omega H\left(\phi(x,y)\right) dxdy > 0, \tag{7}$$

$$c_2 = \frac{\int_\Omega I(x,y)\left(1 - H\left(\phi(x,y)\right)\right) dxdy}{\int_\Omega 1 - H\left(\phi(x,y)\right) dxdy}, \text{ if } \int_\Omega 1 - H\left(\phi(x,y)\right) dxdy > 0, \tag{8}$$

where H is the Heaviside function.

One of the advantages of C-V model is that it can segment structures with ill-defined boundaries that cannot be identified only through the image gradient. This feature meets the requirement of our segmentation problem. The C-V model was later extended to multi-phase level set frame, which can segment multi-regions in an image [20]. However, the calculation of the C-V model is related to the intensities inside and outside the moving contour, which means the C-V model is sensitive to the region of interest. If this region is not defined properly, the segmented boundary may be completely wrong. Besides, the segmentation result depends on the initial position of the contour, because there is no guidance for which structure is wanted. Therefore, the C-V model should be modified in order to be suitable for our application.

3. Proposed Method

In our algorithm, the rectum boundary is assumed to be a *priori* knowledge. The reason is that organs, such as the rectum and bladder, usually appear clearly in the MR images. In most cases, the rectum boundary can be successfully segmented using deformable models or threshold-based algorithms, such as region growing or watershed algorithms [21, 22]. The process can even be fully automatic if the algorithm combines the spatial relationship between image slices and the appearance continuity [23-25]. With this *priori* knowledge, the automatic segmentation of levator ani in MR images becomes feasible.

The proposed algorithm is based on the C-V model, but the moving equation is defined directly and the shape influence field is integrated like in the gradient vector flow algorithm [26]. Since a proper region of interest is critical for a successful implementation of the C-V model, the proposed algorithm starts with the definition of this region.

3.1 Region of interest

Although the soft tissues have greater contrast in MR images than in other imaging modalities, different tissues may still have similar appearances due to the imaging process. Hence, the entire image region cannot be used as the region of interest. A proper region should cover the whole region of the levator ani and meanwhile should keep the background as simple as possible. According to the location of the rectum, an approximated region that covers the muscles can be concluded in each image slice, given the spatial anatomy relationship between the two structures.

In our model, the boundary of the rectum is divided into the anterior part and the posterior part by the horizontal line that passes through the center point of the boundary contour. The shape of posterior boundary can indicate a trend of the shape of the levator ani. Therefore, after sampling the posterior boundary, a second order polynomial can then be used to fit the sampled points, which will generate a parabola that opens upward. Denoting the polynomial as $y = a_0 x^2 + b_0 x + c_0$, the region of interest Ω_0 is defined as a closed set:

$$\Omega_0 = \left\{ p = (x, y) \left| \begin{array}{c} a_0 x^2 + b_0 x + c_{\min} \le y \le a_0 x^2 + b_0 x + c_{\max}, \\ D(p, C_0) \ge D_{\min},\ y_{\min} \le y \le y_{\max} \end{array} \right. \right\} \tag{9}$$

where C_0 represents the boundary of the rectum; $c_{\min}, c_{\max}, y_{\min}, y_{\max}, D_{\min}$ are parameters used to define the region with $c_{\max} > c_{\min} > c_0, D_{\min} > 0$; D is a signed distance function that is defined as:

$$D(p,C) = \begin{cases} \min d(p,p_0), & p \text{ is outside the curve } C \\ -\min d(p,p_0), & p \text{ is inside the curve } C \end{cases}, \quad p_0 \in C \tag{10}$$

where C is a closed contour, $\min d(p,p_0)$ is the distance between the point p and the contour C. The definition of distance assigns negative values to the points that are inside the contour.

The first restriction in the definition of Ω_0 is to locate the ROI between the two parabolas that are close to the posterior boundary of the rectum; the second restriction is on the distance function so that the set can exclude the points that belong to the rectum region; the third restriction, which is on the vertical coordinates, is to form the ROI as an arch-shaped area, so that it will not include other organs or structures, such as vagina or bladder, which are situated above the rectum in the axial view plane. The selection of parameters should assure a simple background and a complete cover of the levator ani. An example of a region of interest is illustrated in Figure 2.

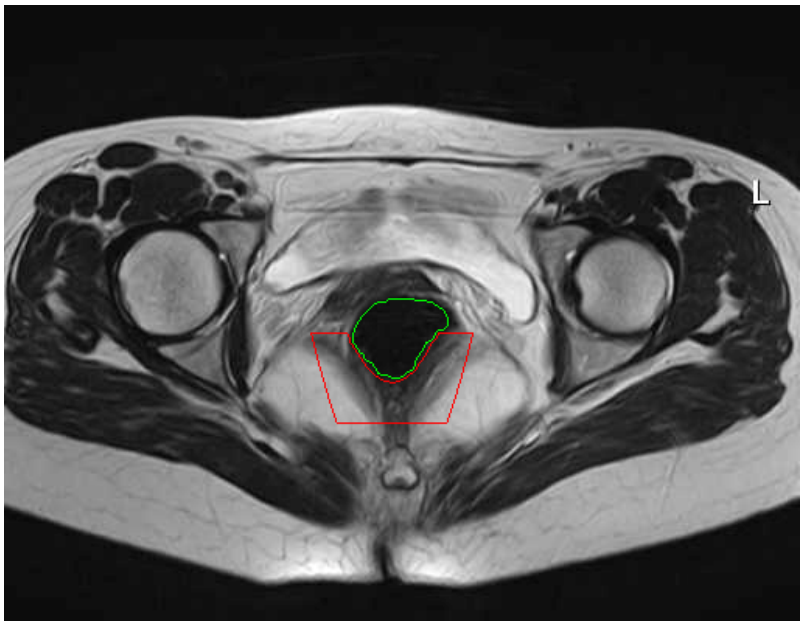

Figure 2: Region of interest (enclosed by the red line) defined by the boundary of rectum (green line).

It is worth pointing out that there are a lot of ways to define a region of interest around the rectum. However, to cover the whole region of levator ani, one should notice that the bottom part of the muscles can be close to the anococcygeal body and

the upper part can reach near the obturator canal [27]. One principle is to cover the complete region and keep the background as simple as possible. The region of interest defined above can be divided into three parts: the levator ani muscles, the connective tissues in the gap between rectum and levator ani, and the rest of the tissues. The levator ani is the darkest part compared with the other two parts. If the images are clear and the influence of connective tissues is not appreciable, the muscles can be successfully segmented by the modified C-V model like in the later illustrated examples. Nevertheless, under most cases the appearance of the levator ani is corrupted by noises or partial volume effect; images in Figure 5 are typical examples. Consequently, the connective tissues between the gap of the rectum and the muscle may have a similar dark appearance as the levator ani. In these cases, traditional algorithms will lead to wrong segmentation. To eliminate the influence of noise and partial volume effects while keeping the integrity of the boundary, a topological preserve technique is used and a shape influence field is introduced to the C-V model.

3.2 Topology preservation

The level set method was used in the C-V model because it can decrease the computational complexity. However, the topology of the moving contour may change during the evolution as the level set method cannot preserve topology. This is not desired for our application, because the influence of noise and fiber tissues may break the continuity of the moving contour. Consequently, the boundary of the levator ani may break into several pieces. To guarantee the integrity of the boundary while keeping the low computational complexity of the level set method, topology preserving techniques should be used. Many algorithms have been proposed to handle this problem [28, 29]. In our model, the algorithm proposed in [28] was chosen because of its simplicity.

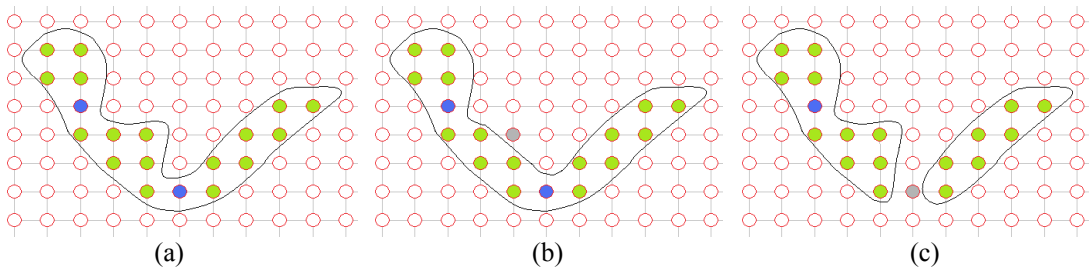

Figure 3: A contour defined in digital topology with simple points (in green) and non-simple points (in blue): (a) original contour; (b) when the contour passes a simple point; (c) when the contour passes a non-simple point.

Han's algorithm is based on the digital topology theories proposed in [30, 31]. In the digital space, a point whose removal does not change the topology of the image is called a simple point (see Figure 3). In order to preserve topology, points that are not simple should not be removed. The following proposition gives a criterion to judge whether a point is simple or not [30]:

Proposition: Suppose x is a point, X is a set and $x \in X$, then x is a n-simple point if and only if $T_n(x, X) = 1$ and $T_{\bar{n}}(x, \bar{X}) = 1$, where T_n and $T_{\bar{n}}$ are the topological numbers defined by the n-connected neighbor of point x in X.

For the 2D images considered in our case, we only need to focus on the case $n = 4$ and $\bar{n} = 8$. Therefore, if we denote the internal region of the moving contour as Ω_1 and the external region as Ω_2:

$$\Omega_1 = \left\{ p = (x, y) \middle| p \in \Omega_0,\ \phi(x, y) \geq 0 \right\},\ \Omega_2 = \Omega_0 \setminus \Omega_1 . \tag{11}$$

Then, we get the following corollary for our model:

Corollary: Let $p \in \Omega_0$, then p is a simple point if and only if $N_4^2(p, \Omega_1)$ is 4-connected and $N_8^1(p, \Omega_2)$ is 8-connected,

where $N_4^2(p, \Omega_1) = \cup \left\{ N_4(y) \cap N_8^*(p) \cap \Omega_1,\ y \in N_4^*(p) \cap \Omega_1 \right\}$,

$N_8^1(p, \Omega_2) = N_8^*(p) \cap \Omega_2$, with $N_m(p)$ the m-connected neighbor set of p in Ω_0 and $N_m^*(p) = N_m(p) \setminus \{p\}$, $m = 4, 8$.

When a point is simple, the removal from its current point set will not change the topology of the image. In our case, when the sign of the new level set value is different to the old one, the corollary is used to identify whether the point is simple or not. If yes, the level set value at the point will be updated; otherwise, a small value with unchanged sign will be assigned. Using this procedure, the topology can be preserved.

The adopted topology preserving technique assures an unchanged topology during the curve movement. Nevertheless, the initial contour should be carefully defined in this case, because the segmented boundary may be incomplete if the initial contour does not cover the whole region of the levator ani muscles, and the influences of noise and connective tissues interrupt the continuity of the appearance. To handle this problem, the initial contour is defined according to the region of interest as follows:

$$L_0 = \left\{ p = (x, y) \middle| p \in \Omega_0,\ D(p, \partial\Omega_0) = -\varepsilon \right\} \tag{12}$$

where ε is a small positive threshold, D is the signed distance function defined in Eq. (10) and $\partial\Omega_0$ is the boundary of the region of interest. The segmentation then becomes a contraction movement of the initial contour until it reaches the boundary of the levator ani.

3.3 Shape influence

When the influence of the connective tissues is appreciable, the selection of parameters in Eq. (4) can be problematic: if λ_1 is too small, the segmented region will cover the connective tissues; if λ_1 is too big, the segmented boundary may not be complete. In other words, the similar appearances of the levator ani and the connective tissues may lead to an expanded boundary, while enforcing the intensity homogeneity inside the contour may lead to an incomplete boundary. Given the appearances of the levator ani and the connective tissues, the topology preserving C-V model will combine the boundaries of two structures. This also indicates that the upper boundary is close to the rectum. A pushing force is needed to let the contour pass the connective tissues, and at the same time avoid affecting the segmentation result when the influence of the connective tissues is not appreciable.

As already discussed, the status of the levator ani is related to the pelvic organs. The deformation of the muscles may be caused by pressure from the organs it supports or the forces it gives to the organs. However, to determine the deformation through force analysis is impossible under such a complex environment. Nevertheless, the shape of rectum in each image slice can be a valuable clue to show the main trend of the deformations. Using this information, we define the shape influence field as follows:

$$S(x, y) = \frac{1 + \alpha\kappa_0}{D(p, C_0)} \cdot \vec{n}_0,\ p = (x, y) \in \Omega_0 \tag{13}$$

where $D(p, C_0)$ is the signed distance function defined in Eq. (10); $\alpha > 0$ is a parameter which controls the influence of curvature; κ_0 and $\vec{n}_0$ are the curvature and the outward normal vector at the point p_0, which satisfies $p_0 \in C_0$ and $d(p, p_0) = D(p, C_0)$. The value of α should guarantee the nominator is positive.

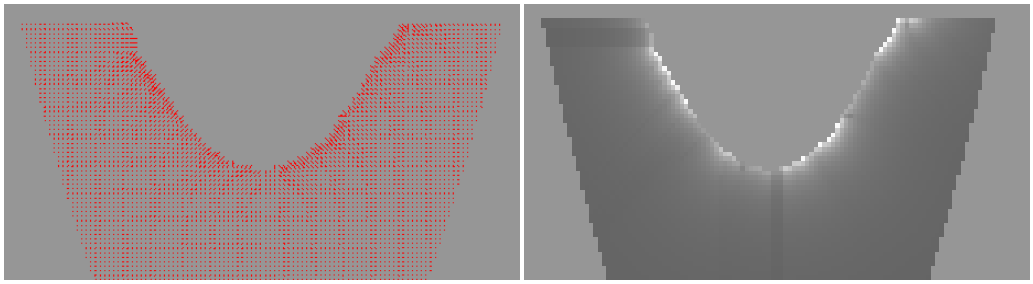

(a) (b)

Figure 4: Shape influence field: (a) vector; (b) its magnitude.

The shape influence field extends the gradient vector field of C_0 to the whole region of interest. The distance item in the denominator of Eq. (13) gives a spatial distribution that decreases with the distance: the closer the moving contour is to the rectum, the larger the influence is. The definition also assures that the influence becomes stronger when the curvature increases because a higher curvature of contour normally indicates a larger deformation of the levator ani muscles. Figure 4 illustrates the shape influence field with its magnitude shown in the gray scale. Then, when the levator ani and the connective tissues cannot be separated through the intensity difference, a pushing force will be added to the moving contour under the shape influence field. The wrong upper boundary will move downward under this force and pass the connective tissue until the boundary reaches a more homogeneous region where the influence of the main external force will stop it.

The shape influence field is integrated into the moving equation like in the gradient vector flow algorithm. Nevertheless, the shape influence field is not like the gradient vector flow field in GVF, because the influence field in our model only provides a direction guidance to pass the false boundary of the levator ani, while the gradient vector flow field provides a global guidance to the boundary, which is not feasible for our application due to the influence of noise and partial volume effect. The shape influence field improves the performance of the C-V model when the connective tissues corrupt the appearance of the levator ani muscles. It also provides shape guidance to the moving direction. The pushing force decreases when the boundary moves farther away. Therefore, when the influence of connective tissues is not appreciable, the addition of shape influence field does not affect the segmentation result, because using the modified C-V model, the upper boundary is not near the rectum and the shape influence is small. Hence, the main external force is determined by the intensity variances of the foreground and background.

3.4 Moving equation

Since in the region of interest the levator ani has the darkest appearance, the internal average intensity c_1 in Eq. (4) can be changed to a fixed value c_1^* so that the movement becomes more targeted and less dynamic. Additionally, it can also facilitate the selection of parameters. The value of c_1^* does not need to be accurate, but should be smaller than the average value of the background. Like in the C-V model, only the curvature item is used in the moving equation to regularize the boundary. Combining the internal forces, the external forces, the shape influence field and the region of interest, the moving equation is defined as:

$$\frac{\partial \phi}{\partial t} = \delta(\phi)\left[\mu \cdot \mathrm{div}\left(\frac{\nabla \phi}{|\nabla \phi|}\right) - \lambda_1 \left(I(x,y) - c_1^*\right)^2 + \lambda_2 \left(I(x,y) - c_2\right)^2 - \beta S(x,y) \cdot \nabla \phi\right],$$

$$\phi(x,y,0) = 0\,,\ (x,y) \in L_0 \tag{14}$$

where ϕ is the signed distance function with positive (negative) value inside (outside) the contour; δ is the Dirac function; $\mu, \beta, \lambda_1, \lambda_2 \geq 0$ are the weights of each item; c_1^* is the *priori* intensity value of the levator ani; c_2 is the average intensity value outside the moving contour; $S(x,y)$ is the shape influence field defined in Eq. (13); Ω_0 is the region of interest defined in Eq. (10); and L_0 is the initial contour defined in Eq. (12).

The algorithm proposed in [32] was chosen to extend the speed function to the region of interest, because under this extension the level set function remains a signed distance function. Explicit finite difference methods can be used to solve the Eq. (14). With the proposed moving equation, the incompleteness of the boundary and the influences of partial volume effects are solved by the topology preserving C-V model with proper defined initial conditions and the shape influence fields. For 3D reconstruction, the segmented boundary can be further smoothed using a post-processing algorithm such as moving window average or Savitzky-Golay's algorithm [33].

3.5 Computational procedure

To conclude our method, the algorithm developed can be summarized as follows:

1. *Initialization*: Set $t = 0$; based on the boundary of rectum C_0:

(a) Form the region of interest Ω_0 and the initial contour L_0;

(b) Form the level set function $\phi(x, y, 0)$;

(c) Form the shape influence field $S(x, y)$.

2. *Update*: Set $t = t + 1$, for every point $p \in \Omega_0$ updated the level set value $\phi(p, t)$ to $\phi(p, t+1)$, according to Eq. (14). If $\phi(p, t) * \phi(p, t+1) \le 0$, then use the corollary in Section 3.2 to check whether p is simple. If no, change the value to $\phi(p, t+1) = sign(\phi(p, t)) * \varepsilon$.

3. *Test:* Check whether $t > T_{threshold}$ and whether the contour has stopped moving. If either of them is true, stop the iteration and go to Step 4; otherwise, return to Step 2.

4. *Post-processing:* Refine the contour using a smoothing algorithm.

4. Experiments and Analysis

In Figures 5 and 6 we illustrate three examples to test the proposed scheme and show the effects of the shape influence field. The images included in these figures were acquired under T2-weighted axial MRI of a symptomatic nulliparous woman. In Figure 5, the levator ani and the connective fiber tissues have similar appearances. One can see that without the shape influence field the boundary covers the levator ani and the connective tissues; while with the shape influence the contour passed the wrong boundary and moved to a more homogeneous region. The incorporation of shape influence field gives the moving contour a pushing force when the intensity difference cannot separate the levator ani muscles and the connective tissues, which leads the contour to the correct position. In Figure 6, the influence of connective tissues is not appreciable. One can see that the segmentation results are not very different with the ones without the shape influence. This is because the distance function is defined as the denominator in the shape influence field. When the contour reaches the correct boundary, it should be far from the rectum so that the shape influence is small and the main external force becomes the intensity variances.

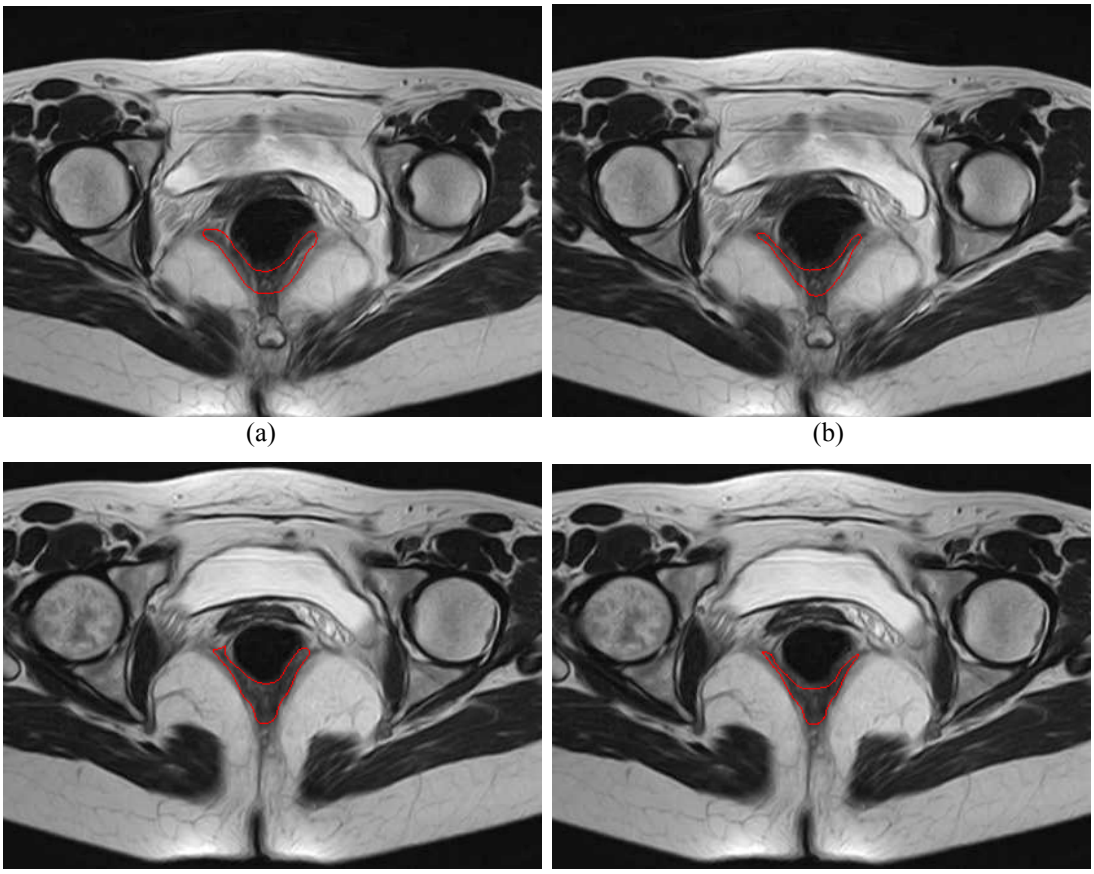

(a) (b)

(c) (d)

Figure 5: Segmentation result when the influences of connective tissues are appreciable: (a) and (c) without shape influence; (b) and (d) with shape influence.

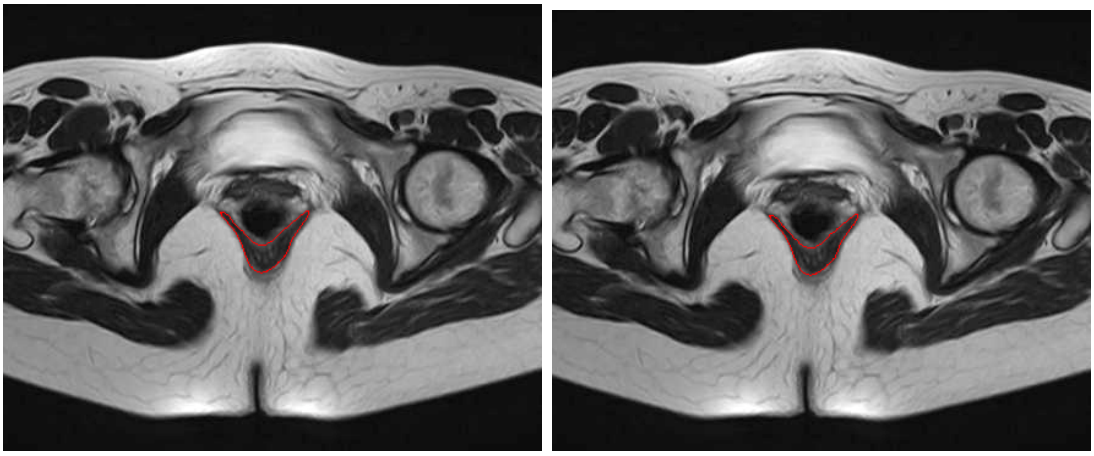

(a) (b)

Figure 6: Segmentation result when the influences of connective tissues are not appreciable: (a) without shape influence; (b) with shape influence.

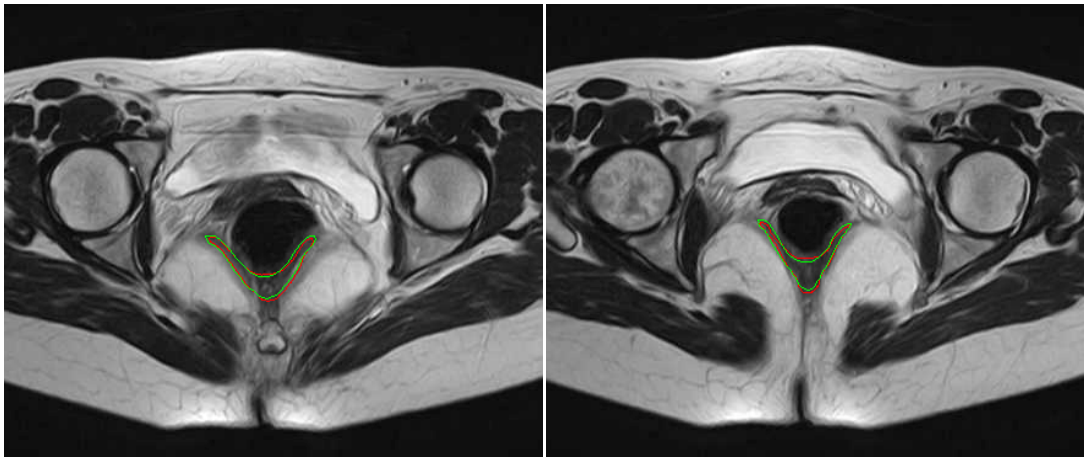

(a) (b)

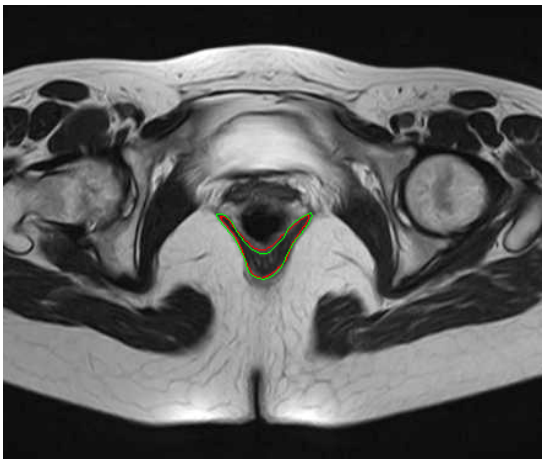

(c)

Figure 7: Overlap of the mean contour (in green) with: (a) results of Figure 5b; (b) results of Figure 5d; (c) results of Figure 6b.

Comparison with the manual segmentations also gives promising results. For each image, manual segmentations were carried out by three technicians. To make the analysis reasonable and minimize the intra-observer errors, a mean contour was obtained by averaging the signed distance functions generated by the manual contours [34]. In Figure 7, we overlapped the mean contour with the results of the proposed algorithm to show the difference. In Table 1 we also give a quantitative analysis of the results, taking the cross-sectional area (CSA) as the measure which is frequently used to study the organ prolapsed (for example, in [7, 8]). The lengths of the contours are also presented as a comparison, from which one can see that the proposed algorithm normally gives a shorter contour because of the smoothing effect of the internal forces. In both cases the algorithm gives a reasonable segmentation both visually and quantitatively.

The proposed algorithm belongs to geometric deformable models, with the main external forces derived from region-based energies and so its performance is less

sensitive to the influence of noise. One common problem for deformable models is the selection of parameters. In our case, besides the parameters that are the same as those in the C-V model, the ones used to define the ROI may change the shape of the initial contour. Nevertheless, if the levator ani is completely covered by the region of interest and the backgrounds of the ROI remain simple, the results will not be influenced appreciably.

The algorithm also has some limitations. The smoothing effect from the internal forces may erase small details of the boundary. Also, there are some cases when the algorithm may not perform well, for example, when the appearance of the levator ani muscle is largely affected by noise or the muscle suffers a huge deformation due to age or severe injury. Therefore, the performance of the proposed algorithm, like most segmentation algorithms, depends on the quality of the image and the patients' state of health. Future work aims to enhance the robustness to handle these problems and decrease parameter dependency in order to make the algorithm more automatic.

Table 1 Comparison on the mean contours obtained by manual and computational segmentations.

Segmentation	Figure 5b		Figure 5d		Figure 6b	
	Area (cm^2)	Length (cm)	Area (cm^2)	Length (cm)	Area (cm^2)	Length (cm)
Manual	2.53	12.63	2.20	12.16	2.62	11.97
Computational	2.49	12.28	2.19	11.63	2.60	10.99

5. Conclusions

Based on the Chan-Vese's model, the method proposed in this paper uses the intensity information and shape influence to segment the levator ani muscles presented in axial MR images. The *priori* knowledge on shape and position of the rectum in each 2D image slice is used to define the initial conditions and forms the shape influence field. The proposed algorithm can improve the accuracy of the segmentation result when the levator ani and the connective tissues have similar appearances. Discussions on the initial conditions, the internal forces and the external forces were presented. Experiments showed the effectiveness of the proposed method.

One may notice that the premise for a successful implementation of the proposed method is to know in advance the boundary of the rectum. However, even when the boundary of rectum cannot be successfully segmented automatically, the algorithm is still practical for use after the manual segmentation of the rectum.

Acknowledgements

This work was partially done in the scope of the projects "BIOPELVIC-Study of Female Pelvic Floor Disorders", "Methodologies to Analyze Organs from Complex Medical Images – Applications to Female Pelvic Cavity", "Aberrant Crypt Foci and Human Colorectal Polyps: mathematical modelling and endoscopic image processing" and "Cardiovascular Imaging Modeling and Simulation - SIMCARD", with references PTDC/SAU-BEB/71459/2006, PTDC/EEA-CRO/103320/2008, UTAustin/MAT/0009/2008 and UTAustin/CA/0047/2008, respectively, financially supported by FCT - Fundação para a Ciência e a Tecnologia of Portugal.

The first author would like to thank FCT for his PhD grant with reference SFRH/BD/43768/2008.

Conflict of interest

None.

References

[1] Buchsbaum GM, Duecy EE, Kerr LA, Huang LS, Guzick DS. 2005. Urinary incontinence in nulliparous women and their parous sisters. Obsete Gynecol. 106(6):1253-1258.

[2] Drossman DA, Li Z, Andruzzi E. 1993. U.S. householder survey of functional gastrointestinal disorders: prevalence, sociodemography, and Health Impact. Dig Dis Sci. 38(9):1569-1580.

[3] Nelson R, Norton N, Cautley E, Furner S. 1995. Community based prevalence of anal incontinence. J Amer Med Assoc. 274(7):559-561.

[4] Macmillan AK, Merrie AEH, Marshall RJ, Parry BR. 2004. The prevalence of fecal incontinence in community-dwelling adults: a systematic review of the literature. Dis Colon Rectum. 47(8):1341-1349.

[5] Noakes KF, Pullan AJ, Bissett IP, Cheng LK. 2008. Subject specific finite elasticity simulations of the pelvic floor. J Biomech. 41(14):3060-3065.

[6] Parente MPL, Jorge RMN, Mascarenhas T, Fernandes AA, Martins JAC. 2008. Deformation of the pelvic floor muscles during a vaginal delivery. Int Urogynecol J Pelvic Floor Dysfunct. 19(1):65-71.

[7] Hsu Y, Chen L, Huebner M, Ashton-Miller JA, DeLancey JL. 2006. Quantification of levator ani cross-sectional area differences between women with and those without prolapse. Obstet Gynecol. 108(4):879-883.

[8] Chen L, Hsu Y, Ashton-Miller JA, DeLancey JOL. 2006. Measurement of the pubic portion of the levator ani muscle in women with unilateral defects in 3-D models from MR images. Int J Gynecol Obstet. 92(3):234-241.

[9] Hamm B, Forstner R. 2007. MRI and CT of the female pelvis. NJ: Springer-Verlag.

[10] Ma Z, Tavares J, Jorge R, Mascarenhas T. 2010. A review of algorithms for medical image segmentation and their applications to the female pelvic cavity. Comput Method Biomec. 13(2):235-246.

[11] Margulies RU, Hsu Y, Kearney R, Stein T, Umek WH, DeLancey JO. 2006. Appearance of the levator ani muscle subdivisions in magnetic resonance images. Obstet Gynecol. 107(5):1064-69.

[12] Stoker J, Taylor SA, DeLancey JOL. 2008. Imaging pelvic floor disorders. Springer.

[13] Tunn R, Delancey JO, Howard D, Ashton-Miller JA, Quint LE. 2003. Anatomic variations in the levator ani muscle, endopelvic fascia, and urethra in nulliparas evaluated by magnetic resonance imaging. Am J Obstet Gynecol. 188(1):116-21.

[14] Cootes TF, Hill A, Taylor CJ, Haslam J. 1994. The use of active shape models for locating structures in medical images. Image Vision Comput. 12(6): 355-366.

[15] Cootes TF, Edwards GJ, Taylor CJ. 2001. Active appearance models. IEEE T Pattern Anal. 23(6): 681-685.

[16] Chan TF, Vese LA. 2001. Active contour without edges. IEEE T on Image Processing. 10(2):266-277.

[17] Osher S, Sethian JA. 1988. Fronts propagating with curvature dependent speed: algorithms based on Hamilton-Jacobi formulations. J Comput Phys. 79(1):12-49.

[18] Malladi R, Sethian JA, Vemuri B. 1993. A topology independent shape modeling scheme. Proceedings of the SPIE Conference on Geometric Methods in Computer Vision II; San Diego, California, USA.

[19] Caselles V, Kimmel R, Sapiro G. 1997. Geodesic active contours. Int J Comput Vision. 22(1):61-79.

[20] Vese LA, Chan TF. 2002. A multiphase level set framework for image segmentation using the Mumford and Shah model. Int J Comput Vision. 50(3):271-293.

[21] Vincent L, Soille P. 1991. Watersheds in digital spaces: an efficient algorithm based on immersion simulations. IEEE T Pattern Anal. 13(6):583-598.

[22] Adams R, Bischof L. 1994. Seeded region growing. IEEE T Pattern Anal. 16(6):641-647.

[23] Mazonakis M, Damilakis J, Varveris H, Prassopoulos P, Gourtsoyiannis N. 2001. Image segmentation in treatment planning for prostate cancer using the region growing technique. Br J Radiol. 74 (2001):243-248.

[24] Iordanescu G, Pickhardt PJ, Choi R, Summers RM. 2005. Automated seed placement for colon segmentation in computed tomography colonography. Acad Radiol. 12(2):182-190.

[25] Pasquier D, Lacornerie T, Maximilien V, Jean R, Eric L, Nacim B. 2007. Automatic segmentation of pelvic structures from magnetic resonance images for prostate cancer radiotherapy. Int J Radiat Oncol Biol Phys. 68(2):592-600.

[26] Xu CY, Prince JL. 1998. Snakes, shapes, and gradient vector flow. IEEE T Image Process. 7(3):359-369.

[27] Decherney AH, Nathan L. 2003. Current obstetric & gynecologic diagnosis & treatment, 9th ed. New York: McGraw-Hill Medical.

[28] Han X, Xu CY, Prince JL. 2003. A topology preserving level set method for geometric deformable models. IEEE T Pattern Anal. 25(6):755-768.

[29] Guyader CL, Vese LA. 2008. Self-repelling snakes for topology-preserving segmentation models. IEEE T on Image Processing. 17(5):767-779.

[30] Bertrand G. 1994. Simple points, topological numbers and geodesic neighborhoods in cubic grids. Pattern Recogn Lett. 15(10):1003-1011.

[31] Bertrand G, Everat JC, Couprie M. 1997. Image segmentation through operators based on topology. J Electron Imaging. 6(4):395-405.

[32] Gomes J, Faugeras OD. 2000. Reconciling distance functions and level sets. J Vis Commun Image R. 11(2):209-223.

[33] Press WH, Flannery BP, Teukolsky SA, Vetterling WT. 1992. Numerical recipes in C: the art of scientific computing, 2nd ed. Cambridge University Press.

[34] Leventon ME, Grimson WL, Faugeras O. 2000. Statistical shape influence in geodesic active contours. Proceedings of IEEE Conference on Computer Vision and Pattern Recognition; Hawaii, USA.

Part B – Article 4

Novel Approach to Segment the Inner and Outer Boundaries of the Bladder Wall in T2-weighted Magnetic Resonance Images

Zhen Ma, Renato Natal Jorge, T. Mascarenhas, João Manuel R. S. Tavares

Published in: Annals of Biomedical Engineering, 39(8): 2287-2297, 2011.

Abstract

Diagnosis of bladder-related conditions needs critical measurements which require the segmentation of the inner and outer boundaries of the bladder wall. In T2-weighted MR images, the low-signal-intensity bladder wall can be identified due to the large contrast with the high-signal-intensity urine and perivesical fat. In this paper, two deformable models are proposed to segment the bladder wall. Based on the imaging features of the bladder, a modified geodesic active contour is proposed to segment the inner boundary. This method uses the statistical information of the bladder lumen and can handle the intensity variation in MR images. Having obtained the inner boundary, a shape influence field is formed and integrated with the Chan-Vese model to segment the outer boundary. The shape guided C-V model can prevent the overlapping between the two boundaries when the appearance of the bladder wall is blurred. Segmentation examples are presented and analyzed to demonstrate the effectiveness of this novel approach.

Keywords: Biomedical Engineering; Medical Imaging; Image Analysis; Image Segmentation; Shape Influence Field; Imaging Appearance.

1. Introduction

Bladder wall thickness is an important measurement for medical diagnosis such as bladder tumours, bladder outlet obstruction, endometriosis and voiding dysfunctions. The normal bladder wall is thin and smooth with a thickness of around 2 mm when moderately distended [1]. Various imaging modalities have been used to visualize the bladder. Cystoscopy is the conventional way to monitor the bladder but it is painful for the patients and only the inner bladder surface can be observed. As an improvement, CT cystoscopy uses helical computed tomography scans to reduce the invasiveness and achieves promising results in detecting bladder lesions and tumours [2-4]. Non-invasive imaging modalities are often used to follow the extravesical extension of the tumours and distant metastasis [3]. Magnetic resonance imaging (MRI) is preferred in many cases, because a reliable detection of pathology requires a clear visualization of the soft tissues [5-9]. Successful applications of MRI to detect

bladder-related conditions have been reported in many articles in the literature [1, 10-12].

T1- and T2-weighted MRI are two basic scans for imaging the bladder, where T1 is the spin-lattice relaxation time and T2 is the spin-spin lattice relaxation time. Different tissues have distinct T1 and T2 values, and the difference can be detected under an electromagnetic field by applying specific pulse sequences. Based on the acquired MR signals, images can be formed to visualize the contrast between tissues. An image where most of the contrast is caused by the differences in the T1 values is called a T1-weighted image; and an image where the contrast is mainly caused by the differences in the T2 values is called a T2-weighted image. Although the bladder and relevant structures can be visualized clearly using MRI, information from the sequential images is neither continuous nor intuitive. In order to carry out further analyses and assist the clinical diagnosis, the bladder wall in each image slice needs to be segmented, which implies the segmentation of the inner and outer boundaries of the bladder wall. The bladder has distinct appearances in T1- and T2-weighted MR images. The differences can be seen in the image in Figure 1. On unenhanced T1-weighted images, the bladder wall appears as a strip with low signal intensity, while the perivesical fat has high signal intensity; therefore, the outer bladder wall can be seen easily. Nevertheless, due to the urine in the bladder lumen which also has low signal intensity, the inner bladder wall is difficult to be discerned especially on heavily T1-weighted images when the bladder is considerably distended [13]. On T2-weighted MR images, the bladder walls have low signal intensities while both the urine and the perivesical fat have high signal intensities; hence, the bladder wall is clearly seen. In this paper, we focus on the segmentation of the bladder wall in T2-weighted MR images.

As the shape of the bladder varies considerably among different individuals, there is no prior shape information to assist the segmentation. The bladder wall appears as a thin strip in the images and its imaging appearance is frequently distorted by noise and partial volume effect. Consequently, satisfied results cannot be attained by using traditional segmentation algorithms. Deformable models have been studied intensively in the area of medical image processing. The flexibility of being able to incorporate various segmentation clues enables them to handle concrete requirements in different applications [9]. Two geometric deformable models are proposed to handle the segmentation of the inner and outer boundaries of the bladder wall. Based

on the imaging appearances of the bladder lumen and the bladder wall, the intensity statistics is used to segment the inner boundary of the bladder wall; and then the location and the shape of the inner boundary are used as guidance to assist the segmentation of the outer boundary. In the following sections, the anatomy of the bladder and the geometric deformable models are reviewed; and afterwards the proposed algorithms are introduced with detailed explanations; experiments are then carried out to testify their performance along with the discussions concerning the algorithms; finally, in the last section, the conclusions and future works are pointed out.

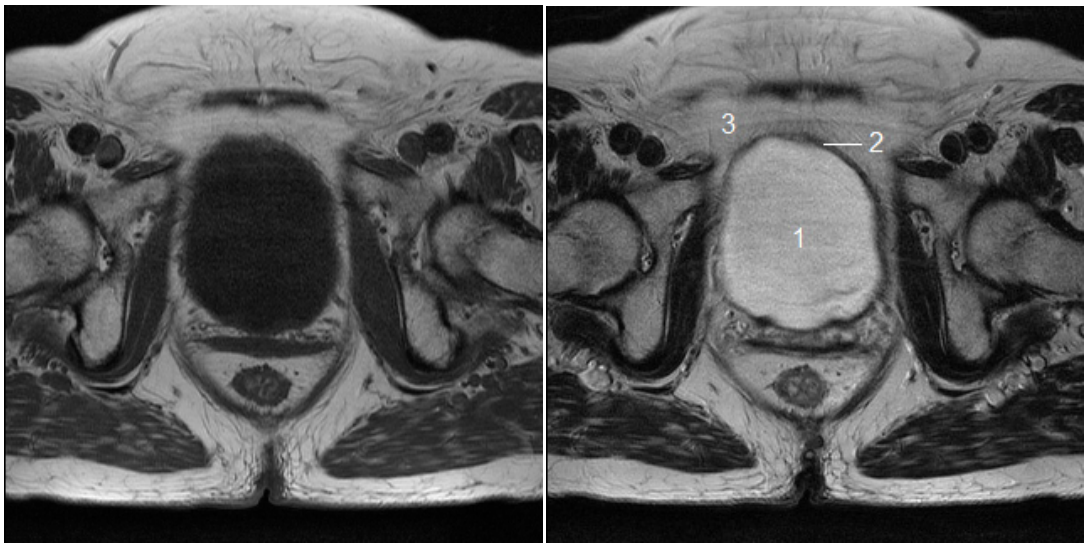

(a) (b)

Figure 1: Imaging appearances of the bladder in unenhanced T1-weighted (a) and T2-weighted (b) MR images (Labels: 1 - bladder lumen; 2 - bladder wall; 3 - perivesical fat). The bladder wall and the urine within the bladder lumen have similar low signal intensity in T1-weighted images, but distinct appearances in T2-weighted images.

2. Materials

In this section, we first review the anatomy and the imaging appearance of the bladder, which are both critical for the segmentation; and then the two geometric deformable models used in the proposed approach are discussed.

2.1 Anatomy and imaging appearance

The urinary bladder is a hollow distensible organ located on the pelvic floor. It is normally modelled as a sphere, with its shape closely related to its contents and neighbouring organs [14]. The bladder wall varies greatly in thickness and shape among individuals. A normal bladder wall comprises four layers: mucosa, submucosa, muscularis propria, and serosa, with the first three forming the main part. Figure 1(b)

shows the bladder wall in T2-weighted images as a low signal intensity band surrounded by the high signal intensity urine and perivesical fats. The lateral walls are well delineated in axial images, while the dome and base of the bladder are better seen from sagittal and coronal views [6]. The imaging appearances of the bladder can vary considerably due to the strength of the magnetic field and the influence of noise and partial volume effect.

2.2 Geometric deformable models

Segmentation performed by geometric deformable models is based on contour evolutions. Proper modelling is required so that the stable status of the moving contour corresponds to the object boundary. The moving equation of a geometric deformable model is a level set equation [15] with its typical formula as:

$$\frac{\partial \phi}{\partial t} + F\left|\nabla \phi\right| = 0,$$

$$\phi(X,0) = 0, \tag{1}$$

where $\phi(X,t)$ is the level set function at time t, X is the Cartesian coordinates, and $F(X,t)$ is the speed function. The level set function embeds the moving contour to its zero level set. With the implicit representation, topological changes are allowed, and the geometric properties of the contours can be calculated easily. Correspondingly, the computational complexity is decreased. The initial level set value is commonly defined as the signed distance to the initial contours, with positive (negative) signs inside (outside) the contour. The definition of the speed function is flexible and can incorporate various clues for segmentation.

2.3 Geodesic active contours

Segmentation using geodesic active contours is based on the large intensity gradient at the object boundary. The energy functional related to this model was defined in [16] as:

$$E(C) = \int_0^1 g\left(\left|\nabla I\left(C(s)\right)\right|\right)\left|C'(s)\right| ds, \tag{2}$$

where C is a contour parameterized by the variable $s \in [0,1]$ and g is a positive decreasing function of the image gradient normally defined as $g = \dfrac{1}{1+\left|\nabla G_\sigma * I\right|^p}$

where p is a parameter, * is the convolution operator, and G_σ is the Gaussian kernel with the width σ.

The functional in Eq. (2) calculates the weighted length of a contour C, and can be minimized by the object boundary. To find the boundary, the moving equation is derived based on the Euler-Lagrange equation of Eq. (2):

$$\frac{\partial \phi}{\partial t} = g(I)\kappa|\nabla\phi| + \nabla g(I)\cdot\nabla\phi, \tag{3}$$

where $\kappa = \mathrm{div}\left(\frac{\nabla\phi}{|\nabla\phi|}\right)$ is the curvature.

The Gaussian filter in the definition of g can smooth the image and decrease the influence of noise. The value of σ should be selected according to the noise level: a larger value of σ corresponds to a smoother image. However, since the Gaussian filter also blurs the object boundary, σ should not be very large, especially when the object has a weak-gradient boundary. Following Eq. (3), the contour moves along the vector field ∇g to the object boundary under the smoothness constraint. However, the initial contours are required to be placed near the object boundary. To overcome this restriction, a constant speed was added in [16] and the moving equation became:

$$\frac{\partial \phi}{\partial t} = g(c+\kappa)|\nabla\phi| + \nabla g\cdot\nabla\phi, \tag{4}$$

where c is the constant speed. With the addition of the constant speed, the initial contours can be placed away from the object boundary; hence, the segmentation becomes less sensitive to the initial conditions. The value of c affects the convergence speed of the moving contour to the boundary. Besides, if there are local boundaries with large intensity gradients caused by noise or intensity variation, a large constant speed can act as a "balloon" force to drive the contours beyond these unwanted boundaries.

The speed function of the geodesic active contours depends on the intensity gradient. In the MR images, the partial volume effect can blur the boundaries between different structures and decrease the intensity gradient; besides, the inhomogeneous intensity distribution can also cause large intensity gradients and cause unwanted boundaries. Hence, modifications are required to make this model suitable for our application.

2.4 Chan-Vese model

The intensity gradient is not always a reliable clue for segmentation, especially for medical images where the imaging appearances of structures are frequently influenced by noise and partial volume effect. Sometimes, the object boundary cannot be identified through the intensity gradient. Chan-Vese (C-V) model [17] provides an effective way to handle the segmentation in these cases. Instead of using the intensity gradient, the C-V model is based on the difference between the intensities of the object and the background; the main idea is to minimize the intensity variations of the regions inside and outside the moving contour. Hence, the energy functional of the C-V model was proposed as:

$$E(C)=\mu\cdot\text{Length}(C)+\nu\cdot\text{Area}\left(inside(C)\right)+\lambda_1\int_{inside(C)}\left|I(x,y)-c_1\right|^2 dxdy+\lambda_2\int_{outside(C)}\left|I(x,y)-c_2\right|^2 dxdy, \quad (5)$$

where C is a contour; I is the intensity; $\mu,\ \nu\geq 0,\ \lambda_1,\ \lambda_2>0$ are the weights; c_1 and c_2 are the mean intensity values inside and outside the contour. The first two items are the internal energy that restrict the geometric regularity of the moving contour and help to prevent leakage. The last two terms are the external energy that defines the object boundary as the one that minimizes the functional. Based on Eq. (5), the moving equation of the C-V model is derived as:

$$\frac{\partial\phi}{\partial t}=\delta(\phi)\left[\mu\cdot\text{div}\left(\frac{\nabla\phi}{|\nabla\phi|}\right)-\nu-\lambda_1\left(I(x,y)-c_1\right)^2+\lambda_2\left(I(x,y)-c_2\right)^2\right], \quad (6)$$

$$\frac{\delta(\phi)}{|\nabla\phi|}\frac{\partial\phi}{\partial\vec{n}}=0,\ \text{on}\ \partial\Omega, \quad (7)$$

where δ is the Dirac function; $\partial\phi/\partial\vec{n}$ denotes the normal derivative of ϕ at the image boundary; Ω is the image region; and the mean intensity values can be calculated as:

$$c_1=\frac{\int_\Omega I(x,y)H\left(\phi(x,y)\right)dxdy}{\int_\Omega H\left(\phi(x,y)\right)dxdy},\ \text{if}\ \int_\Omega H\left(\phi(x,y)\right)dxdy>0;$$

$$c_2=\frac{\int_\Omega I(x,y)\left(1-H\left(\phi(x,y)\right)\right)dxdy}{\int_\Omega 1-H\left(\phi(x,y)\right)dxdy},\ \text{if}\ \int_\Omega 1-H\left(\phi(x,y)\right)dxdy>0, \quad (8)$$

where H is the Heaviside function defined as $H(x)=1$, when $x\geq 0$ and $H(x)=0$, when $x<0$. The values of λ_1 and λ_2 should be defined and balanced according to the

image contents; a larger value of the weight means a stronger constraint on the homogeneity of the intensity distribution of the associated region.

The C-V model can correctly segment the object boundary when the image gradient at the boundary is weak or the object appears as pixel clusters. However, one can see the calculation of C-V model is related to the moving contour and the image background. Therefore, a proper computational region is needed, and modifications are required to make this model suitable for our application.

3. Methods

Effective algorithms should be able to segment the boundaries with the influence of noise and partial volume effect. As the tissues around the bladder form a complex background, the outer boundary of the bladder wall is harder to be segmented than the inner boundary; hence, the inner boundary is segmented first, and then this information is used to assist the segmentation of the outer boundary.

3.1 Segmentation of the inner boundary

In T2-weighted MR images, the bladder wall has low signal intensity and its appearance is appreciably different to the high signal intensity urine and fat. If the images are not severely influenced by noise, the inner boundary can be identified correctly based on the large intensity gradient using the geodesic active contour. Nevertheless, image gradient is not a reliable segmentation clue because it only reflects the local intensity changes. As intensity variation is inevitable in MR images, inhomogeneous intensities can cause a large intensity gradient and lead to false boundaries; meanwhile, the partial volume effect can smooth intensity changes and decrease gradient magnitude. Both cases can lead to unwanted results; a case in point can be seen in Figure 2. In Figure 2 (a) and (b), the moving contour stopped at places where there were large gradients, which were caused by the intensity variation, even though the intensities there were still inside the normal range. To handle this case, a large constant expanding speed should be used to inflate the contour passing the false boundaries; or the weight of the internal force should be increased so that interruptions and leakages can be eliminated by the smoothness constraint. However, adjusting these parameters may cause new problems. For example, in Figure 2(c) the contour passed the local boundaries with a large constant expanding speed, but leaked outside at the boundaries with weak gradient.

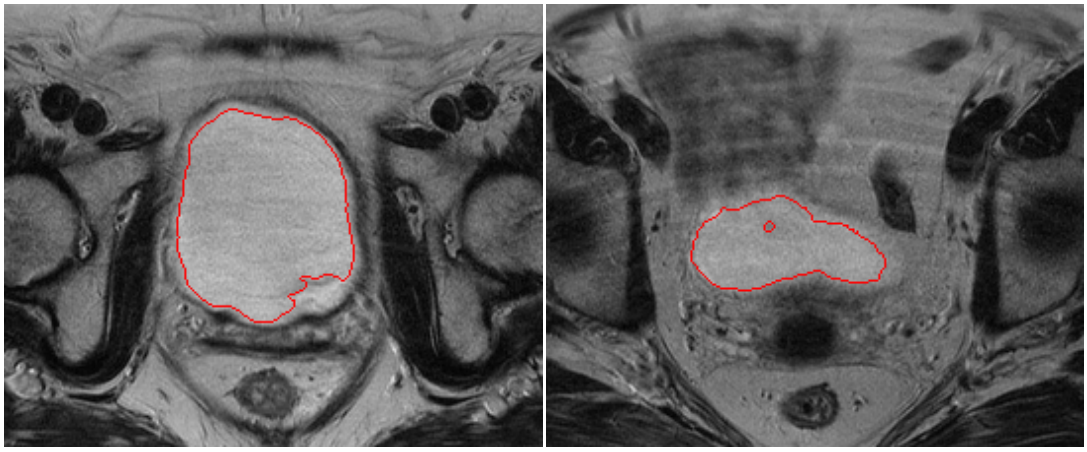

(a) (b)

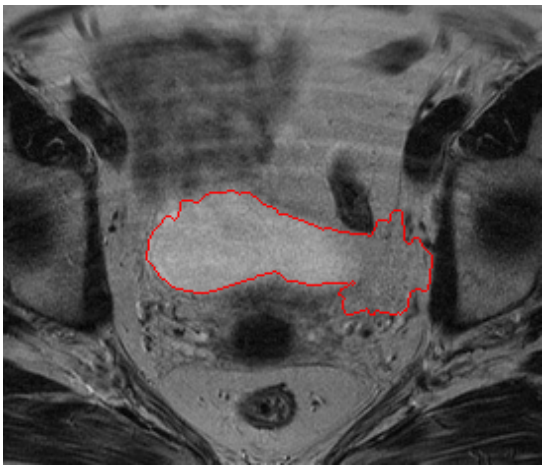

(c)

Figure 2: Problems when using the geodesic active contour: contour cannot arrive at the correct position because of noise influence and the smooth constraint (a); inner boundary in the bladder lumen that cannot be eliminated by a small constant speed (b); contour passed the inner boundary but leaked outside at the weak boundary due to a large constant speed (c).

For the geodesic active contour, the speed function is based on the intensity gradient in a neighbourhood area around the moving contour; therefore, the calculation only concerns the intensity difference between the neighbouring pixels. An appreciable difference between the intensities of these pixels can cause a large intensity gradient, similar to the influence of noise. If the inhomogeneous regions in the bladder lumen have considerable size and area, the influence caused by intensity variation cannot be eliminated through Gaussian smoothing. On the other hand, the partial volume effect in MR images can decrease the intensity gradient at the boundaries and cause leakage. In order to avoid inner boundaries and leakages caused by local intensity variations, region information should be used.

A proper speed function should guarantee that its value changes smoothly when the intensity varies in a normal range but decreases quickly when outside that range.

We then assume that the intensity of the bladder lumen follows the Gaussian distribution and define the function g in Eq. (4) as:

$$g(I) = p(I) = \frac{1}{\sqrt{2\pi}\sigma^*} \exp\left(-\frac{(I-\mu)^2}{2\sigma^{*2}} \right), \tag{9}$$

where μ and σ^* are the mean and the modified standard deviation of the intensity I that are calculated in Eq. (11). Like the one defined in the geodesic active contours, the function $g(I) \in [0,1]$, but its value changes smoothly when I varies around the mean value, and diminishes quickly when I is outside the normal range. The modified geodesic active contour is then proposed as:

$$\frac{\partial \phi}{\partial t} = p(I)(1+\kappa)|\nabla \phi| + \lambda \nabla p(I) \cdot \nabla \phi, \tag{10}$$

where λ is the weight and the rest of the parameters are defined as in Eq. (4). Using the level set representation, the μ and σ^* in Eq. (9) can be calculated as:

$$\mu = \frac{\int_\Omega H(\phi(x,y)) I(x,y)\, dxdy}{\int_\Omega H(\phi(x,y))\, dxdy},$$

$$\sigma^* = \max\left(\sqrt{\frac{\int_\Omega H(\phi(x,y))(I(x,y)-\mu)^2\, dxdy}{\int_\Omega H(\phi(x,y))\, dxdy}}, \sigma_0 \right), \text{ if } \int_\Omega H(\phi(x,y))\, dxdy > 0, \tag{11}$$

where σ_0 is a predefined value and H is the Heaviside function defined in Eq. (8). Initial contours should be defined inside the bladder lumen. Therefore, the inner boundary of the bladder wall is obtained by the expansion of the moving contours.

The speed function in Eq. (10) is changed from gradient-based to region-based. The probability distribution function acts as a criterion to judge whether the contour should move forward or should stay still. If the contour moves outside the bladder lumen, where the intensities are beyond the normal range, the speed deceases quickly and correspondingly slows down the contour. Then, even if the intensity changes gradually and appears as a weak boundary, the contour can stop at the boundary. The standard deviation of the intensity is calculated as follows: when this value is smaller than σ_0, it is set to σ_0. The modification is to make the proposed algorithm less sensitive to the initial conditions. Since the intensity statistics of the bladder lumen is related to the moving contour, the values obtained in the beginning phase may derivate from the real ones and lead to wrong segmentation results. For example, if

the initial contour is placed at a region where the local intensity variance is small, when the contour arrives at other regions where the intensities are appreciably different to the ones of the initial region, the contours may stop moving due to the quick decrease of the speed function. Nevertheless, with the modified calculation, when this case happens, the standard deviation is set to σ_0; hence, the tolerance of the intensity variation is extended and the contour can move forward to arrive at the correct boundary. The value of σ_0 should be defined according to the intensity distribution of the bladder lumen. A larger σ_0 means a bigger range to allow intensity variation; therefore, the modification makes the algorithm more flexible.

There are two external forces in the proposed algorithm, balanced by the parameter λ. One is generated by the multiplication of the probability with the constant expanding speed; the other is based on the gradient of the probability. Unlike the geodesic active contours in Eq. (4), the main external force in Eq. (10) is the expanding force controlled by the probability, while the second part can accelerate the movement and attach the contour to the boundary. Based on the region-based external forces and the large appearance contrast between the bladder wall and the bladder lumen, the proposal algorithm can easily handle the local boundaries and leakages caused by intensity variation and partial volume effect; meanwhile, its time efficiency can be improved by the narrow band method [18]. An example of segmentation can be seen in Figure 3(a)-(b).

3.2 Segmentation of the outer boundary

The neighbouring tissues of the bladder form a complex background and the partial volume effect may further blur the appearance of the bladder wall, which can cause difficulties to segment the outer boundary. Nevertheless, since the inner boundary of the bladder wall has been segmented, the spatial and anatomical relationship between the two boundaries can be used to assist the segmentation. In the following section, these clues are combined and a shape guided algorithm is proposed to segment the outer boundary.

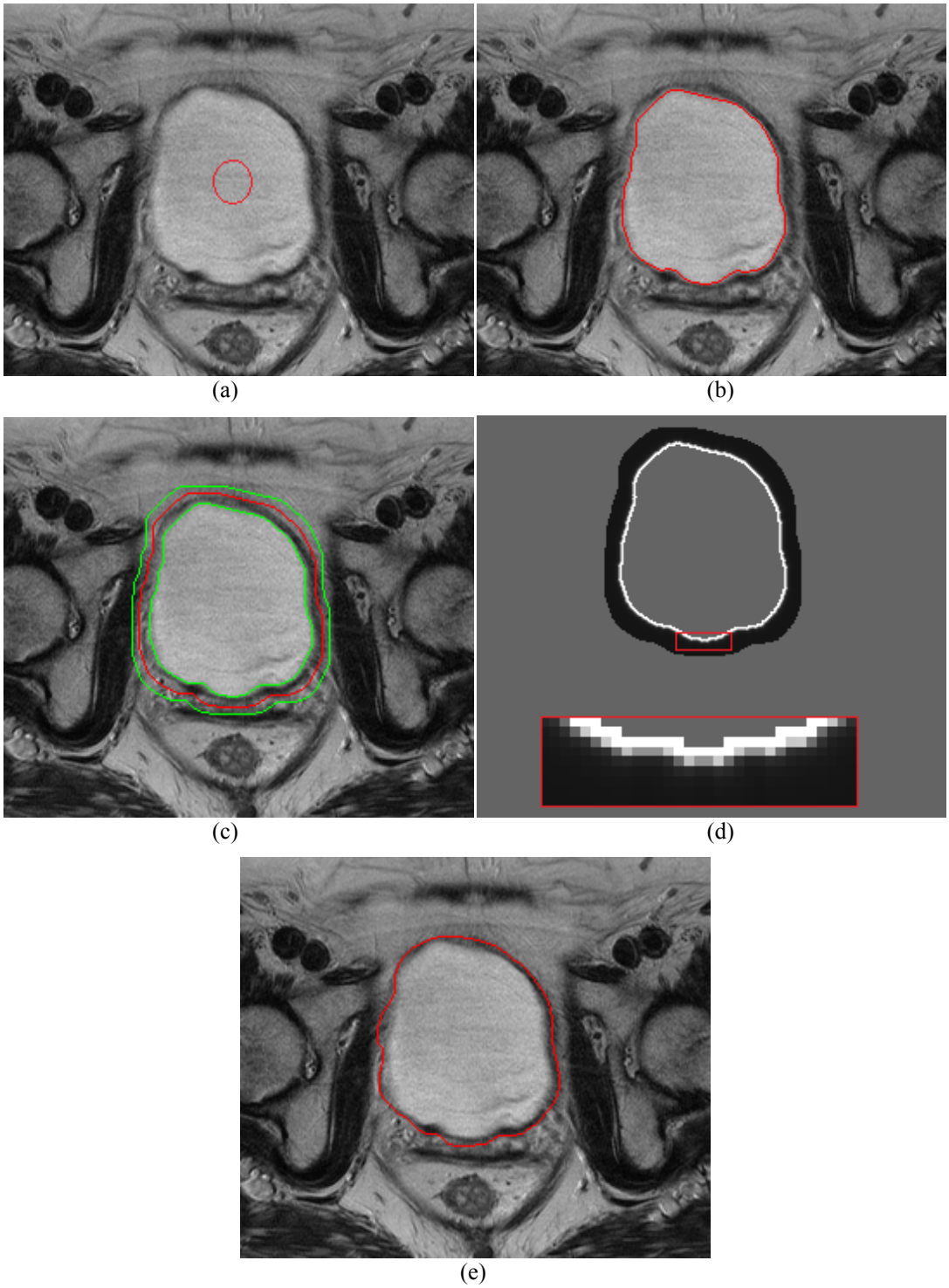

Figure 3: Segmentation procedure using the proposed algorithms: place the initial contour inside the bladder lumen (a); the inner boundary segmented by the modified geodesic active contour algorithm (b); the region of interest (enclosed by the green lines) and the initial contour (red line) (c); the shape influence field in the region of interest shown in gray scales (The region enclosed by the red rectangle is amplified below) (d); the outer boundary segmented by the shape-guided C-V model (e).

Intensity gradient is not a reliable clue for the segmentation of the outer boundary. When the bladder is distended, the bladder wall is thin and its imaging appearance can be distorted easily by noise and partial volume effect; sometimes parts of the outer

boundary may appear as pixel clusters. As we aforementioned, the Chan-Vese model is effective to handle these cases. Nevertheless, the C-V model is related to the computational region that is defined by the internal and external region of the moving contour. The complex imaging background in T2-weighted MR images cannot be used as the computational region. Hence, a region of interest (ROI) should be defined to exclude the influence of the neighbouring tissues. Given the location of the inner boundary, the ROI is defined as:

$$\Omega_0 = \left\{ p = (x, y) \middle| 0 \le D(p, C_0) \le D_{\max} \right\}, \tag{12}$$

where C_0 is the inner bladder wall; $D_{\max}$ is a threshold, and $D(p, C_0)$ is the distance between the point p to the contour C_0 defined as:

$$D(p, C_0) = \begin{cases} \min\limits_{p_0 \in C_0} d(p, p_0), p \text{ is outside } C_0 \\ -\min\limits_{p_0 \in C_0} d(p, p_0), p \text{ is inside } C_0 \end{cases}, \tag{13}$$

with $d(p, p_0)$ the Euclidean distance between the two points.

The ROI defined in Eq. (12) is a ring band next to the inner boundary of the bladder wall. The value of $D_{\max}$ in the definition should guarantee that the outer bladder wall is completely covered in ROI and the low signal intensity bladder wall can be well discerned from the high signal intensity background.

There is no requirement for the initial contours in the C-V model. Nevertheless, as topological changes are allowed during the movement, the continuity of the moving contour can be broken. In order to keep the segmented boundary as a continuous closed contour, the initial contour is defined near the outer edge of the ROI as:

$$L_0 = \left\{ p = (x, y) \middle| p \in \Omega_0,\ D(p, C_0) = D_{\max} - \varepsilon \right\}, \tag{14}$$

where ε is a small positive value.

If the appearance of the bladder wall is not severely influenced by noise and partial volume effect, the outer boundary of the bladder wall can be segment correctly by using C-V model in the ROI. However, when the bladder is distended, the appearance of the bladder wall is frequently blurred and some parts may even become invisible due to the diffusion. Consequently, the outer boundary segmented by the C-V model may cross the outer boundary and overlap with the inner boundary. A pushing force is then needed to keep the two boundaries separated. Meanwhile, the blurred parts of the outer boundary should be inferred based on the smoothness

constraint and the shape similarity between the inner and outer boundaries. Given these considerations, the thickness information of the bladder wall is incorporated and a shape influence field is defined as:

$$S(x,y)=\frac{1+\alpha\kappa_0}{\left(D(p,C_0)-1/r\right)^2+\varepsilon}\cdot\vec{n}_0,\ p=(x,y)\in\Omega_0, \tag{15}$$

where α is the weight; ε is a small positive value to avoid 0 (zero) denominator; $r\times r$ is the spatial resolution of the image (mm×mm); κ_0 and $\vec{n}_0$ are the curvature and the outward normal vector at the point $p_0\in C_0$ that satisfies $d(p,p_0)=D(p,C_0)$. A thickness of 1 mm is assumed as the minimum tolerance of the bladder wall thickness based on the reports in [1, 19]. The value $1/r$ maps the minimal thickness to the Euclidean point distance on the image. The irregularity of the inner boundary also affects the field; the larger the curvature is, the higher the possibility for the moving contour to deform is.

The shape influence field defined in Eq. (15) extends the gradient field of the inner boundary to the ROI Ω_0. The magnitude of the shape influence field decreases with the distance when $D(p,C_0)>1/r$. During the movement, the closer the contour approaches to the bladder wall, the larger the shape influence field is. The magnitude of the shape influence field becomes largest when the contour is 1 mm from the inner boundary of the bladder wall; therefore, the moving contour cannot move forward after arriving there and the overlapping is avoided naturally. The quick decease of the shape influence field along with the distance guarantees that when the outer boundary is far from the inner boundary, the segmentation result will not be influenced appreciably by this field. Figure 3(d) illustrates the shape influence field of the image in Figure 3(c) where its magnitude is represented by the gray scale, from which one can see a quick decrease of the shape influence with the increasing distance. Hence, the shape influence field can reflect the shape of the inner boundary and provide shape guidance to the moving contour. Then, the shape influence field is incorporated to the C-V model and the moving equation is proposed as:

$$\frac{\partial\phi}{\partial t}=\mu\cdot\mathrm{div}\left(\frac{\nabla\phi}{|\nabla\phi|}\right)-\lambda_1\left(I(x,y)-c_1^*\right)^2+\lambda_2\left(I(x,y)-c_2\right)^2+S(x,y)\cdot\nabla\phi, \tag{16}$$

where the internal mean intensity c_1 is changed to a predefined value c_1^*, and the remaining parameters are defined as in Eq. (6). The mean external intensity c_2 is calculated as:

$$c_2 = \frac{\int_{\Omega_0} I(x,y)\left(1-H\left(\phi(x,y)\right)\right)dxdy}{\int_{\Omega_0} 1-H\left(\phi(x,y)\right)dxdy}, \text{ if } \int_{\Omega_0} 1-H\left(\phi(x,y)\right)dxdy > 0, \quad (17)$$

where the integral region is changed from the whole image to the ROI Ω_0 defined in Eq. (12), and H is the Heaviside function defined in Eq. (8).

With the incorporation of the shape influence field, the original balance achieved by the C-V model through intensity contrast is affected. If the moving contour approaches too close to the inner boundary of the bladder wall, it will be pushed back by the force derived by the shape influence field. The shapes of the blurred parts are determined by the smoothness constraint on the moving contour and the shape guidance provided by the shape influence field. With the quick decrease of the shape influence along with the distance, the segmentation results are not much affected when the bladder wall has a clear appearance and the outer boundary is not close to the inner boundary.

The speed function in Eq. (16) is extended to the ROI using the method proposed in [20]. The extension of the speed function makes the algorithm focus on the movement of the initial contours, and therefore it avoids the possible inner boundaries when the appearance of the bladder wall is affected. The mean intensity value of the internal region is fixed in order to make the segmentation more reliable and less dynamic; as sometimes the perivesical fats that are near the bladder wall have similar appearances to the bladder wall itself due to the partial volume effect, they become included in the outer boundary based on their large intensity contrasts to the high signal intensity background. In this case, a fixed value of the internal mean intensity can drive the contour to a more homogeneous region and arrive at the correct outer boundary. The value of c_1^* does not need to be accurate but should be sufficiently lower than the background to exclude possible influences. An example of the segmentation process of the outer boundary is shown in Figure 3(d)-(e).

3.3 Procedure outline

As an outline of the proposed approach, we list the full segmentation procedures as follows:

0. Smooth the image to reduce the influence of noise.

1. To segment the inner boundary of the bladder wall:

(a) Set the initial contours inside the bladder lumen and form a narrow band around each initial contour;

(b) Calculate the initial level set values in the narrow bands based on the signed distance function; and then calculate the mean intensity value μ and the modified intensity variance σ^* of the bladder lumen using Eq. (11).

(c) Update the level set values according to Eq. (10) and correspondingly the values of μ, σ^* and the narrow bands, until the contours stop moving or the iteration times exceed the threshold.

2. To segment the outer boundary of the bladder wall:

(a) Define the ROI based on the inner boundary of the bladder wall using Eq. (12), and then form the shape influence field using Eq. (15);

(b) Set the initial contour defined in Eq. (14) and calculate the initial level set values in the ROI, based on the signed distance function;

(c) Update the level set values according to Eq. (16) and correspondingly the value of c_2 by Eq. (17) until the contour stops moving.

4. Results and Discussions

We selected two representative image series with no contrast enhancement to test the performance of the proposed algorithms. The first series was acquired under a two-dimensional (2D) T2-weighted turbo-spin echo (TSE) sequence with field strength: 3.0 T, TE: 83 ms, TR: 3650 ms, bandwidth: 260 Hz/pixel, FOV: 225×250 mm^2, acquisition matrix: 202×320 and flip angle: 150°. The second series was acquired under a two-dimensional 2D TSE sequence with field strength: 1.5 T, TE: 103 ms, TR: 5239 ms, bandwidth: 130 Hz/pixel, FOV: 220×220 mm^2, acquisition matrix: 272×320 and flip angle: 150°. The bladder wall can be clearly seen in the first image series; while its appearance is blurred by the partial volume effect in the second image series. The two image groups tested the performance of the proposed algorithms in different situations.

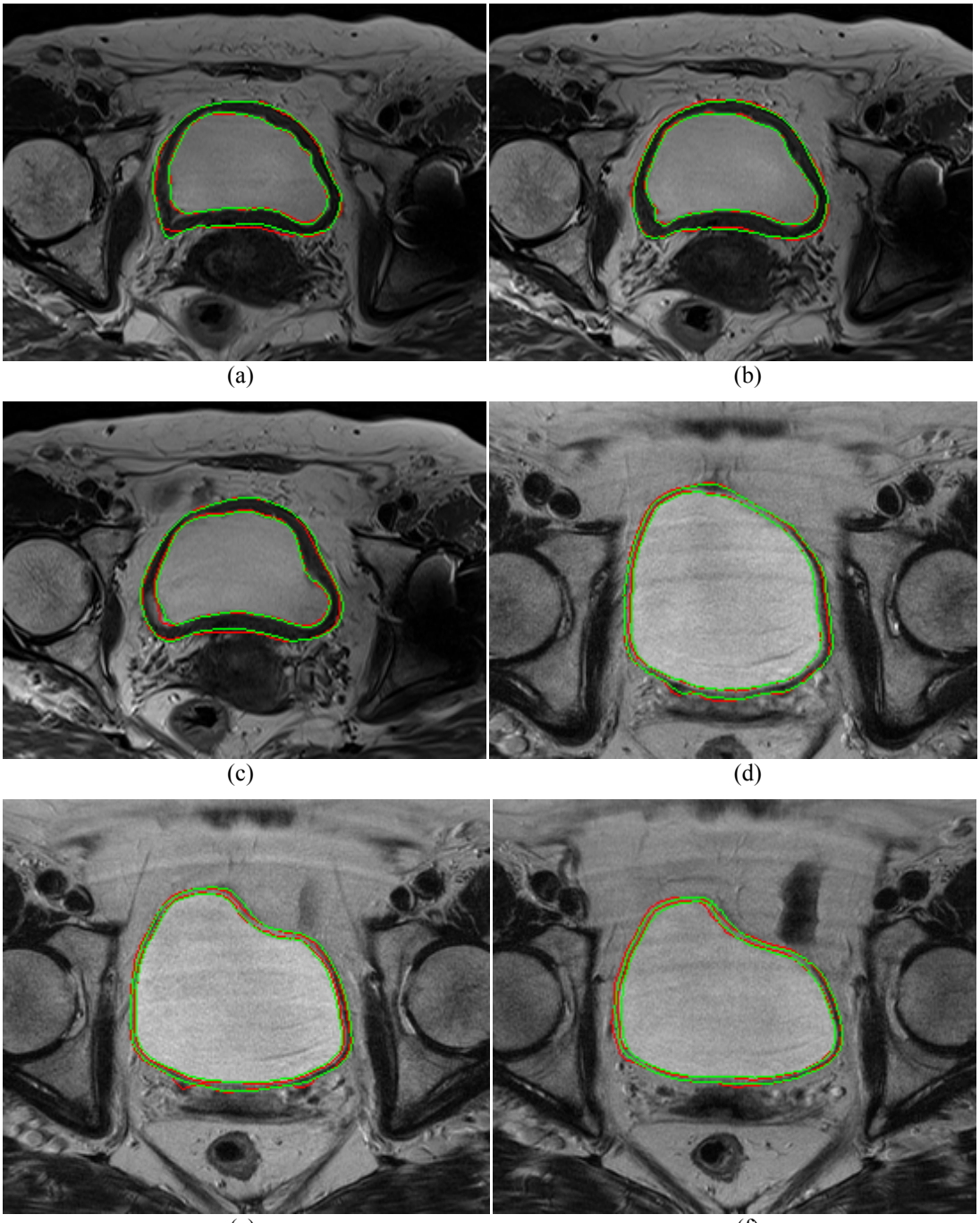

Figure 4: Segmentation results (red lines) overlapped with the ground truth (green lines).

Figure 4 illustrates several examples. To show the deviations of the results intuitively, we overlap them with the ground truth. The ground truth was defined as the mean shape of the manual segmentations performed separately by three experienced technicians through averaging the signed distance functions generated by these manually segmented boundaries [21]. One can see that the inner boundaries are correctly segmented despite the presence of noise and partial volume effect. Compared with the geodesic active contour, the proposed algorithm is not sensitive to

the local intensity variation and the moving contour can stop at the boundaries where the image gradient is weak. The statistical information of the bladder lumen determines whether the contour should move forward or should stay still. For the segmentation of the outer boundary, with the ROI defined nearby the inner boundary, the moving contours are less affected by the tissues surrounding the bladder. The segmented outer boundary is continuous and closed, and did not overlap with the inner boundary even when the appearance of the bladder wall is blurred; and the shapes of the blurred parts in Figure 4(d)-(f) are inferred by the shape influence field and the smoothness of the contour. One can see the segmentation is qualitatively satisfied.

To quantitatively evaluate the point-to-point matching of the segmentation results, we adopted three indices. The Hausdorff measure is used to reflect the largest derivation between the points of the two contours. Hence, the distance between a point p and a contour C is calculated as:

$$D(p,C) = \min_{p_1 \in C} d(p, p_1), \tag{18}$$

where $d(p, p_1)$ is the Euclidean distance between two points; and the Hausdorff distance between two contours is then calculated as:

$$D(C_0, C_1) = \max\left(\max_{p \in C_0} D(p, C_1), \max_{p \in C_1} D(p, C_0) \right), \tag{19}$$

where C_0 is the contour from the ground truth and C_1 is the contour obtained by the algorithm. Besides the conventional Hausdorff distance, the mean and the standard derivation of $D(p, C_1)$, $p \in C_0$ are used to show the overall derivation of the results; the statistics of the point-to-contour distance can indicate the average point matching. Table 1 presents these indices of the images illustrated in Figure 4.

Table 1 Comparison between the results by the algorithms and the ground truth. (HD – Hausdorff Distance; STDV – Standard Deviation; SR – Spatial Resolution)

Figure 4	HD (mm)		Mean (mm)		STDV (mm)		SR (mm×mm)
	Inner	Outer	Inner	Outer	Inner	Outer	
a	1.56	3.22	0.37	0.67	0.41	0.65	0.78×0.78
b	1.10	1.75	0.33	0.59	0.39	0.41	
c	2.34	1.75	0.59	0.61	0.48	0.52	
d	1.38	1.54	0.37	0.48	0.39	0.41	0.69×0.69
e	1.38	2.83	0.62	0.56	0.33	0.47	
f	2.06	2.06	0.61	0.61	0.49	0.50	

In order to show the influence of the segmentation results on the quantitative analysis, Table 2 gives the percentage of the difference in the cross-sectional areas of the bladder lumen, the bladder wall and the region covered by the outer boundary. The area of the bladder lumen A_{bl}, the area of the bladder wall A_{bw} and the area covered by the outer boundary A_{bo} are calculated as:

$$A_{bl} = \text{Area}\left(inside\left(C_{inner}\right)\right),\ A_{bo} = \text{Area}\left(inside\left(C_{outer}\right)\right),$$

$$A_{bw} = A_{bo} - A_{bl}, \tag{20}$$

where C_{inner} stands for the inner boundary and C_{outer} stands for the outer boundary; and the coverage ratio CR and the percentage difference PD are defined as:

$$CR\left(C_0, C_1\right) = \frac{\text{Area}\left(inside\left(C_0\right) \cap inside\left(C_1\right)\right)}{\text{Area}\left(inside\left(C_0\right) \cup inside\left(C_1\right)\right)}, \tag{21}$$

$$PD\left(C_0, C_1\right) = \frac{\left|\text{Area}\left(inside\left(C_0\right)\right) - \text{Area}\left(inside\left(C_1\right)\right)\right|}{\text{Area}\left(inside\left(C_0\right)\right)}, \tag{22}$$

where C_0 is the contour from the ground truth and C_1 is the contour obtained by the algorithm.

These measurements are based on the regions covered by the inner and outer boundaries of the bladder wall, and show the region matching and the influence of the segmentation accuracy on the quantitative analysis. From the comparisons one can see the results are also quantitatively satisfied.

Table 2 Comparison of the quantitative measures (PD – Percentage Difference in the area defined in Eq. (22); CR – Cover Ratio defined in Eq. (21); PDBW – Percentage Difference in the area of the Bladder Wall)

Figure 4	Inner		Outer		PDBW (%)
	PD (%)	CR	PD (%)	CR	
a	0.95	0.97	0.10	0.96	0.87
b	0.21	0.98	2.36	0.97	0.18
c	2.28	0.96	0.65	0.97	2.18
d	1.92	0.98	0.19	0.98	1.91
e	3.34	0.97	0.20	0.97	3.30
e	3.34	0.97	0.20	0.97	3.30
f	2.37	0.96	1.44	0.97	2.34

Satisfied results can be obtained using the proposed algorithms when the bladder wall is not severely influenced by noise and partial volume effect. For the inner boundary, the modified calculation of the intensity statistics in Eq. (11) makes the

algorithm less sensitive to the initial conditions; it also makes the algorithm flexible to handle the influence of noise. For the outer boundary, the background in ROI needs to be simple, because the surrounding tissues may have similar appearances to the bladder wall. A large $D_{\max}$ in Eq. (12) may deviate the moving contour from the correct position and cover unwanted structures. Sometimes, manual intervention is needed in order to exclude the influence of other tissues. One may also notice that small shape disturbances of the boundaries are erased in the results of the proposed algorithms; this smoothing effect is carried out by the internal forces to obtain a smooth curve and eliminate the influence of noise.

The proposed algorithms are computationally efficient. For the inner boundary of the bladder wall, the narrow band method we adopted has the time complexity of $O(nk)$, where n is the pixel number of the moving contour and k is the band width; for the outer boundary of the bladder wall, since the computation is in the ROI, the time complexity is $O(Nk_1)$, where N is the number of inner boundary pixels and k_1 is the width of the ROI. Hence, for both segmentations, the calculations are performed in a local band and therefore the segmentation is efficient. Nevertheless, a common problem for the deformable model is that parameters need to be selected properly and this process can sometimes be time-consuming.

5. Conclusion

The approach proposed in this paper can handle the segmentation of the inner and outer boundaries of the bladder wall effectively. The imaging features of the bladder wall in MR images are incorporated into a level set framework. The shape influence field prevents the two boundaries from overlapping with each other even if the appearance of the bladder wall is affected by noise and partial volume effect.

Nevertheless, there are some cases in which the algorithms developed cannot perform well; for example, if the appearance of the bladder lumen is severely influenced by noise or if the bladder suffers physical deformities such as tumour, there may be a heavy intensity bias inside the bladder lumen, which can influence the intensity statistics and lead to incorrect segmentation. Manual interventions are then needed to handle these cases. For the outer boundary of the bladder wall, when the neighbouring tissues are close to the bladder wall, manual intervention is also needed to exclude their influence in the region of interest. Also, the T2-weighted MRI is

recommended to assess tumour invasion into the muscle layer of the bladder wall and prostate5, 7. How to improve the robustness of the segmentation algorithms with the presence of a tumour or carcinoma is an important aspect for our future work as well as improving the robustness and automation of the algorithms.

Acknowledgements

This work was partially done in the scope of the projects "Methodologies to Analyze Organs from Complex Medical Images – Applications to Female Pelvic Cavity", "Aberrant Crypt Foci and Human Colorectal Polyps: mathematical modeling and endoscopic image processing" and "Cardiovascular Imaging Modeling and Simulation - SIMCARD", with references PTDC/EEA-CRO/103320/2008, UTAustin/MAT/0009/2008 and UTAustin/CA/0047/2008, respectively, financially supported by FCT - Fundação para a Ciência e a Tecnologia, in Portugal.

The first author would like to thank FCT for his PhD grant with reference SFRH/BD/43768/2008.

Conflict of interest statement

The authors report no conflicts of interest.

References

[1] Paramasivam S, Proietto A, Puvaneswary M. 2006. Pelvic anatomy and MRI. Best Pract Res Cl Ob. 20(1):3-22.

[2] Vining DJ, Zagoria RJ, Liu K, Stelts D. 1996. CT cystoscopy: an innovation in bladder imaging. Am J Roentgenol. 166(2):409-410.

[3] Song JH, Francis IR, Platt JF, Cohan RH, Mohsin J, Kielb SJ, Korobkin M, Montie JE. 2001. Bladder tumor detection at virtual cystoscopy. Radiology. 218(1):95-100.

[4] Jaume S, Ferrant M, Macq B, Hoyte L, Fielding JR, Schreyer A, Kikinis R, Warfield SK. 2003. Tumor detection in the bladder wall with a measurement of abnormal thickness in CT scans. IEEE T Bio-med Eng. 50(3):383-390.

[5] Barentsz JO, Jager GJ, Witjes JA, Ruijs JHJ. 1996. Primary staging of urinary bladder carcinoma: the role of MRI and a comparison with CT. Eur Radiol. 6(2):129-133.

[6] Cheng D, Tempany CMC. 1998. MR imaging of the prostate and bladder. Semin Ultrasound CT. 19(1):67-89.

[7] Tekes A, Kamel I, Imam K, Szarf G, Schoenberg M, Nasir K, Thompson R, Bluemke D. 2005. Dynamic MRI of bladder cancer: evaluation of staging accuracy. Am J Roentgenol. 184(1):121-127.

[8] Ma Z, Jorge RNM, Tavares JMRS. 2010. A shape guided C–V model to segment the levator ani muscle in axial magnetic resonance images. Med Eng Phys. 32(7):766-774.

[9] Ma Z, Tavares JMRS, Jorge RNM, Mascarenhas T. 2010. A review of algorithms for medical image segmentation and their applications to the female pelvic cavity. Comput Method Biomec. 13(2):235-246.

[10] Barentsz JO, Engelbrecht MR, Witjes JA, de la Rosette JJ, van der Graaf M. 1999. MR imaging of the male pelvis. Eur Radiol. 9(9):1722-1736.

[11] Lammle M, Beer A, Settles M, Hannig C, Schwaibold H, Drews C. 2002. Reliability of MR imaging-based virtual cystoscopy in the diagnosis of cancer of the urinary bladder. Am J Roentgenol. 178(6):1483-1488.

[12] Dimopoulos J, Schirl G, Baldinger A, Helbich TH, Pötter R. 2009. MRI assessment of cervical cancer for adaptive radiotherapy. Strahlenther Onkol. 185(5):282-287.

[13] Nicolas V, Beyersdorff D. "The urinary bladder." In: MR Imaging of the Abdomen and Pelvis, edited by B. Hamm, G. P. Krestin, M. Laniado, V. Nicolas, and M. Taupitz. New York: Georg Thieme Verlag, 2010, pp. 209-217.

[14] Margot SD, Steven LL. 1995. The effect of urinary bladder shape on its mechanics during filling. J Biomech. 28(6):725-732.

[15] Osher S, Sethian JA. 1998. Fronts propagating with curvature-dependent speed: algorithms based on Hamilton-Jacobi formulations. J Comput Phys. 79(1):12-49.

[16] Caselles V, Kimmel R, Sapiro G. 1997. Geodesic active contours. Int J Comput Vision. 22(1):61-79.

[17] Chan TF, Vese LA. 2001. Active contour without edges. IEEE T Image Process. 10(2):266-277.

[18] Adalsteinsson D, Sethian JA. 1995. A fast level set method for propagating interfaces. J Comput Phys. 118(2):269-277.

[19] Jequier S, Rousseau O. 1987. Sonographic measurements of the normal bladder wall in children. Am J Roentgenol. 149(3):563-566.

[20] Gomes J, Faugeras O. 2000. Reconciling distance functions and level sets. J Vis Commun Image R. 11(2):209-223.

[21] Leventon ME, Grimson WEL, Faugeras O. Statistical shape influence in geodesic active contours. Proceedings of the 2000 IEEE Conference on Computer Vision and Pattern Recognition, IEEE Computer Society, South Carolina, 2000, pp. 316-323.

Part B – Article 5

Segmentation of Female Pelvic Cavity in Axial T2-weighted MR Images towards the 3D Reconstruction

Zhen Ma, Renato Natal Jorge, T. Mascarenhas, João Manuel R. S. Tavares

Published in: International Journal for Numerical Methods in Biomedical Engineering, 28(6-7): 714-726, 2012.

Abstract

The anatomies of pelvic structures are critical for the diagnosis of pelvic floor dysfunctions. However, due to the complex background, the imaging appearances of pelvic organs and muscles are frequently distorted by noise and partial volume effect. Magnetic resonance imaging with its clear imaging quality of the female pelvic cavity is preferred for many studies. As such, correct segmentations of the pelvic structures on MR images are required for accurate diagnoses. Effective algorithms for axial T2-weighted MR images have been proposed, which are based on the imaging features of different structures and various image clues. In this paper, we review these algorithms and evaluate their performance, and discuss implementation issues and aspects towards constructing the three-dimensional models.

Keywords: Medical Imaging, Image Segmentation, Deformable Models, Bladder, Vagina, Rectum, Levator Ani Muscle.

1. Introduction

Pelvic floor (PF) dysfunctions include a series of conditions that affect a large number of women. Common symptoms include urinary incontinence, fecal incontinence, pelvic organ prolapse, etc. Many works including biomechanical simulations and clinical studies have been carried out to reveal the causes of these symptoms [1-7]; in such studies, imaging techniques have an important role.

The detection of pathology relies on a clear visualization of the soft tissues [6-8]. Magnetic resonance (MR) imaging is preferred in many studies due to its superior imaging quality of soft tissues, and MR images have been of noteworthy assistance in clinical diagnoses. However, MR images of pelvic cavity can only provide information on cross-sectional planes; the shapes and anatomy of the pelvic organs are neither continuous nor intuitive. Accordingly, one needs to segment the relevant structures from each image slice so as to carry out further diagnoses. Hence, accurate segmentation becomes a very important procedure.

The bladder, vagina, rectum, and levator ani muscle are the pelvic structures that are frequently involved in the PF dysfunctions [1, 2]. Due to the complex anatomy, segmentation of these structures is usually performed by manually. However,

effective algorithms can be employed to improve the time efficiency of the process and meanwhile eliminate the intra- and inter-observer errors. An effective segmentation algorithm should be based on the geometrical features and imaging appearances of the relevant structures [9]. Algorithms along these lines have been proposed to handle the segmentations of the pelvic structures on axial T2-weighted MR images [10, 11]. The algorithm in [10] is a coupling approach that can segment the three pelvic organs simultaneously based on their different imaging appearances; the algorithm in [11] is a shape-guided Chan-Vese model that can segment the levator ani muscle with the assistance of the rectum boundary. Both algorithms achieved satisfactory segmentation results. Nevertheless, these algorithms are still in an incipient phase. Detailed tests with these algorithms can help to further their development. In this paper, we first review these algorithms, and then evaluate their performances using a case study, from which we discuss the aspects that need to be improved with the aim to construct the three-dimensional (3D) models of the female pelvic structures.

The paper is organized as follows: in Section 2, the relevant background knowledge is presented, including deformable models and pelvic organs, and the algorithms used are described. Then in Section 3, the algorithms are tested on MR image series and the implementation details are outlined and discussed. In Section 4, the quantitative analysis of the segmentation results are presented and the performance of the algorithms are discussed. In the last section, the conclusions are highlighted and perspectives of future work are pointed out.

2. Methodology

The algorithms to be evaluated include a coupling approach that is composed of three deformable models and a shape guided Chan-Vese model. In order to facilitate the discussions, we first review the geometric deformable models, and then introduce the algorithms.

2.1 Geometric deformable models

Deformable models refer to the algorithms that perform the image segmentations based on curve evolutions [9]. According to the way of contour tracking, the deformable models are classified into parametric or geometric models. The latter

models are based on the level set method [12] and are the basis of the algorithms under comparison.

The level set method was initially proposed to allow topological changes during curve evolution. The moving contour is embedded in a higher-dimensional level set function $\phi(X,t)$ as its zero level set $\phi(X,t)=0$, where X stands for the contour coordinates and t is the time; then, instead of tracking the movement of the contour points, one can implicitly track the zero level set of $\phi(X,t)$. The standard form of a level set equation is:

$$\frac{\partial \phi}{\partial t} + F|\nabla \phi| = 0, \tag{1}$$

where $\phi(X,t)$ is the level set function, and F is the speed function. The initial level set function $\phi(X,0)$ is normally defined as the distance function to the initial contours, with positive/negative signs inside/outside the contours. The implicit tracking of the contour movement decreases the computational complexity and facilitates the calculations of the geometric properties of the moving contours.

The moving equation of the geometric deformable models should be defined so that the final status of the moving contour corresponds to the object boundary. In this process, various image clues can be incorporated into the models for segmentation. Reviews and recent advances of the algorithms based on the level set method can be found in [9, 13, 14]. The flexibility of the geometric deformable models makes them suitable to be used on T2-weighted MR images of the pelvic cavity [9].

2.2 Pelvic organs

The bladder, vagina and rectum have distinct imaging appearances on T2-weighted MR images: the bladder lumen has a high signal intensity appearance due to the urine within it; the vagina has medium-low signal intensity, but may have a high signal intensity central strip due to secretions; the rectum has low signal intensity that is distinct to the bladder and vagina, and its multiple layers have different appearances. On T2-weighted MR images, the appearances of the pelvic organs are frequently influenced by noise and partial volume effect; as such, the intensity gradient is not a reliable clue for segmentation. A considerable number of operations are needed to handle the intensity variations if the organs are to be segmented separately. Alternatively, the algorithm in [10] used the differences between the intensity

distributions of the pelvic organs; and based on appearance comparisons, the bladder, vagina, and rectum can be segmented simultaneously. The main segmentation clues used are the appearance similarities between the different layers of the pelvic organs. For example, compared with the high signal intensity bladder lumen, the bladder wall has a low signal intensity that is similar to the appearance of the muscular layer of the rectum; therefore, if the initial contours are placed inside the bladder lumen, they can expand until reaching the bladder wall where the appearances are more like the vagina and rectum. For the vagina and rectum, their surrounding tissues have comparably high signal intensity appearances that are more like the bladder lumen; similar movements can be applied to the two organs. Hence, segmentation is carried out through the appearance comparisons among the three pelvic organs. Following this idea, a coupling approach was proposed in [10] as:

$$\begin{cases} \dfrac{\partial \phi_1}{\partial t} = \delta(\phi_1)\left(p_1\left(e_1 - \max\left(e_2, e_3, e_1 - 1\right)\right) + \alpha_1 \nabla g \cdot \nabla \phi_1 + \gamma_1 \mathrm{div}\left(\dfrac{\nabla \phi_1}{|\nabla \phi_1|}\right)\right) \\ \dfrac{\partial \phi_2}{\partial t} = \delta(\phi_2)\left(p_2\left(e_2 - \max\left(e_1, e_3, e_2 - 1\right)\right) + \alpha_2 \nabla g \cdot \nabla \phi_2 + \beta S_2 + \gamma_2 \mathrm{div}\left(\dfrac{\nabla \phi_2}{|\nabla \phi_2|}\right)\right), \\ \dfrac{\partial \phi_3}{\partial t} = \delta(\phi_3)\left(\max\left(p_2, p_3\right)\left(e_3 - \max\left(e_1, e_3 - 1\right)\right) + \alpha_3 \nabla g \cdot \nabla \phi_3 + \nu S_3 + \gamma_3 \mathrm{div}\left(\dfrac{\nabla \phi_3}{|\nabla \phi_3|}\right)\right) \end{cases} \tag{2}$$

where δ is the Dirac function, ϕ_1 is the level set function for the segmentation of the bladder, ϕ_2 for the vagina, and ϕ_3 for the rectum; $e_i = \log(p_i)$ where $p_i = \dfrac{1}{\sqrt{2\pi}\sigma_i} \exp\left(-\dfrac{(I-u_i)^2}{2\sigma_i^2}\right)$ is the intensity distribution function of the pelvic organs with u_i and σ_i as the mean intensity and intensity variance; α_i, β, ν, γ_i are the weights of each item, with $i = 1, 2, 3$; $g = \dfrac{1}{1+|\nabla I|^2}$ where I is the image intensity; and:

$$S_i = -\left(H\left(\phi_i(x)\right) - H\left(\phi_i^*\left(x - \mu_{\phi_i}\right)\right)\right) - \frac{\left(x - \mu_{\phi_i}\right)^T}{\int H(\phi_i)\,dx} \times \int \left(H\left(\phi_i(x')\right) - H\left(\phi_i^*\left(x' - \mu_{\phi_i}\right)\right)\right) \delta\left(\phi_i(x')\right) \nabla \phi_i(x')\,dx' \quad \text{, with } i = 2, 3, \tag{3}$$

where ϕ_2^* and ϕ_3^* are the level set functions defined as the signed distance functions to the prior shapes of the vagina and rectum, H is the Heaviside function, and μ_{ϕ_i} is the center of gravity of the moving contour. The curvature $\mathrm{div}\left(\frac{\nabla\phi_i}{|\nabla\phi_i|}\right)$ is the internal force that constrains the geometric properties of the moving contours.

The coupling approach is a modified region competition algorithm initially proposed in [15]. The initial contours are required to be defined inside each pelvic organ so as to avoid the influence of the neighboring pelvic tissues. Therefore, the three pelvic organs are segmented through the expanding of the initial contours, and the intensity statistics are updated along with the contour movement. Moreover, since the vagina and rectum have layers with distinct appearances, the mean intensity and intensity variance of the two organs should be properly calculated; and the calculations are on the subset of the internal region of the moving contours as:

$$\Omega_2^* = \left\{(x,y)\middle|\phi_2(x,y,t)\geq 0; p_2\left(I(x,y)\right) > p_1\left(I(x,y)\right), p_3\left(I(x,y)\right)\right\};$$

$$\Omega_3^* = \left\{(x,y)\middle|\phi_3(x,y,t)\geq 0; p_3\left(I(x,y)\right) > p_1\left(I(x,y)\right), p_2\left(I(x,y)\right)\right\}.$$

Moreover, the standard deviation of the image intensity is modified as $\sigma_i = \max(\sigma_i, \sigma_0)$, where σ_0 is a predefined value, in order to decrease the sensitivity of the performance to the initial contours; hence, even if the value of intensity variance is not accurate, the movement of the contours in the beginning phase will not be affected appreciably.

For the vagina, due to its thin appearance on the axial images, its boundary can be easily distorted by the partial volume effect. Also, the distinct layers of the rectum can lead to unwanted inner boundaries. In order to solve these problems, a second external force S_i was added to the moving equations of the two organs, which was derived from the prior shapes and can provide guidance for the contour movement. The main reason of adding this force is based on the fact that although the shapes of the vagina and rectum vary appreciably among individuals, a shape constraint can help the contour pass the unwanted inner boundaries and can also avoid leakages across the correct boundaries, even if the prior shape is not accurate. As such, the segmentation can be assisted when the contours do not arrive at the correct positions only based on the imaging appearances of the vagina and rectum.

Consequently, there are two external forces in the moving equations to segment the vagina and rectum. The main external force is the one from the appearance comparisons and is reflected by the logarithms of the probabilities. However, as the objects to be compared are limited to the three pelvic organs, inaccurate results may happen. For example, the intensity variance of the bladder lumen is comparably small, which means the normal intensity only varies in a narrow range; if the imaging appearance of the bladder wall is distorted by noise and partial volume effect, the moving contour may leak outside once it passes the boundary. This is because the perivesical fats around the bladder have appearances more similar to the bladder than to the vagina and rectum, and according to the region competition algorithm in [15], the moving speed is not insignificant. Consequently, although the contour moves to a region where the appearance is already quite different to the bladder, the contour cannot stop at the bladder boundary. In order to handle this situation, the item derived by the appearance comparison was multiplied by the probability p_1 ; since $p_1 e_1 \le p_1\left(e_1 - \max\left(e_2, e_3, e_1 - 1\right)\right) \le p_1$, one gets $p_1\left(e_1 - \max\left(e_2, e_3, e_1 - 1\right)\right) \to 0$ when $p_1 \to 0$. Therefore, even when the contour leaks outside where the intensity is beyond the normal range, the movement is quite slow and tends to stop due to the small value of p_1 . Based on the same reasoning, in the moving equation for the vagina and rectum, the items derived from the appearance comparisons were multiplied by the probabilities. For the rectum, as the rectal lumen has a similar appearance to the vagina, the comparison is only between the bladder and the rectum so as to avoid inner boundaries; and correspondingly, in the moving equation the multiplier p_3 was replaced by $\max\left(p_2, p_3\right)$ in order to let the contour pass the rectal lumen where p_3 is small. Additionally, the item $\nabla g \cdot \nabla \phi_i$ was added to accelerate the convergence and attach the contour to the boundary [16].

2.3 Levator ani muscle

The levator ani muscle constitutes the main part of the pelvic floor muscles. It appears as a thin strip under the rectum with a “V” shape on the axial plane. The status of levator ani muscle is closely related to the pelvic organs; the actual shape of this muscle varies greatly with the individual’s physical condition and health status. Accordingly, there is no accurate prior shape available to assist the segmentation.

Moreover, the imaging appearance of the muscle is frequently distorted by noise and partial volume effect on T2-weighted MR images. These features make the levator ani muscle difficult to be segmented.

Since the levator ani muscle has a low signal intensity appearance that is appreciably different to its surrounding tissues, the problem can become an easier two-phase segmentation if the segmentation is done inside a small neighborhood region. Therefore, with the location of the pelvic organs defined, a region of interest (ROI) can be selected to facilitate the segmentation and help to exclude the influence of the surrounding tissues. As the levator ani muscle sometimes appears as pixel clusters on the axial plan, the intensity gradient is not a suitable clue for segmentation. The Chan-Vese model proposed in [17] provided an effective way to handle the segmentation in this case; the algorithm tries to find the boundary of the object by minimizing the total intensity variations inside and outside the moving contour. If the image is not severely influenced by noise and partial volume effect, the levator ani muscle can be segmented successfully by using this model. Nevertheless, the connective tissues between the rectum and the levator ani muscle may also have similar low signal intensity appearances due to the blur on images; consequently, some parts of these tissues tend to be included by the boundary segmented by the Chan-Vese model, especially when the posterior part of the rectum is near to the levator ani muscle. A push force is then needed to keep the moving contour away from the rectum, and at the same time not affect the movement when the contour is not near the rectum.

The main function of the levator ani muscle is to give support to the pelvic organs; the deformation of the muscle can be a result of the status of these organs. Based on the three segmented organs, the shape of the rectum, especially its low posterior part, is valuable to predict the deformation trend of the muscle. Hence, a shape influence field $S(x, y)$ was introduced and defined as:

$$S(x,y) = \frac{1+\alpha\kappa_0}{D(p,C_0)} \cdot \vec{n}_0 , \ p = (x,y) \in \Omega_0 , \tag{4}$$

where Ω_0 is the ROI; $\alpha > 0$ is a parameter; $D(p,C_0)$ is the distance between the point p to the rectum boundary C_0; κ_0 and $\vec{n}_0$ are the curvature and the outward normal vector at the point p_0 which satisfies $p_0 \in C_0$ and $d(p,p_0) = D(p,C_0)$.

The field defined in Eq. (4) is a spatial extension of the external normal field of the rectum boundary, with its magnitude decreasing when the point is away from the rectum. It mimics the pushing force that the rectum gives to the levator ani muscle and therefore provides shape guidance for the muscle. Using this shape influence field, the contour is guided to contract when it leaks outside and near to the rectum; besides, the spatial decreasing property assures that the movement will not be influenced much when the contour is away from the rectum. Therefore, a push force generated by this shape influence field meets the segmentation requirements. Then, a shape-guided Chan-Vese model was proposed as [11]:

$$\frac{\partial \phi}{\partial t} = \delta(\phi)\left[\mu \cdot \mathrm{div}\left(\frac{\nabla \phi}{|\nabla \phi|}\right) - \lambda_1 \left(I(x,y) - c_1^*\right)^2 + \lambda_2 \left(I(x,y) - c_2\right)^2 - \lambda_3 S(x,y) \cdot \nabla \phi\right], \quad (5)$$

where δ is the Dirac function; ϕ is the level set function; μ and λ_i (≥ 0), with $i = 1, 2, 3$, are the weights of each item; c_1^* is the predefined intensity value of the levator ani muscle; and c_2 is the mean intensity value outside the moving contour in the ROI.

As the imaging appearance of the levator ani muscle can be easily distorted, the continuity of the segmented boundary can be interrupted. In order to avoid the sensitivity to the initial conditions, the initial contour L_0 was defined next to the boundary of the ROI:

$$L_0 = \left\{ p = (x,y) \middle| p \in \Omega_0,\ D(p, \partial\Omega_0) = -\varepsilon \right\},$$

where Ω_0 is the ROI and ε is a small positive value. Then, the segmentation is performed by the contract of the initial contour. Topology preservation strategy was applied to further keep the moving contour as a simply connected curve. The mean intensity of the levator ani muscle is fixed as c_1^* so as to make the movement less dynamic and its value does not need to be accurate but should be sufficiently lower than the intensity of the background in the ROI. According to Eq. (5), when the contour moves into the connective tissues, the force generated by the shape influence field can push the contour backward and lead the contour to a position under the shape guidance.

3. Segmentation

An axial T2-weighted image series was used to evaluate the performance of the segmentation algorithms. The image data was acquired from a 68-year-old woman under a turbo-spin echo (TSE) sequence with the field strength 3.0 T, echo time (TE): 83 ms, repetition time (TR): 3650 ms, and acquisition matrix: 202×320. The spatial resolution of the axial images is 0.6875mm×0.6875mm×5.400mm. The prior shapes of vagina and rectum were unavailable before segmentation.

Among the 28 axial images, there were twelve in which the pelvic organs and the levator ani muscle could be identified clearly; and accordingly, we assessed the algorithms mainly on these images. The images were numbered sequentially following the order from the inferior end to the superior end of the human body. Given that the boundary of the rectum is treated as prior information in the segmentation of the levator ani muscle, the three pelvic organs were segmented first, and then the levator ani muscle.

3.1 Initial conditions

The segmentation started from the first image in which the three organs appeared simultaneously. We adopted the strategy that once an image is successfully segmented, the intensity statistics of each organ are stored. As such, if some organs did not appear on the neighboring images, the stored statistical information could be used when applying the coupling approach. Since the prior shapes were not available, in the experiments a rectangle of the dimensions equal to 5×70 (pixel size) was used as the prior shape of the vagina and a circle with radius equal to 18 (pixel size) for the rectum. The segmented boundaries had different shapes to the prior shape, while from the results one could see that the inaccuracy of the shape constraints did not influence the correctness of the results appreciably.

Due to the complex anatomy of the pelvic organs, there is no automatic way to define the initial contours. The modification of the intensity variance can help to decrease the sensitivity to the initial contours; the initial contours used for the vagina should be placed so that their major parts are outside the vaginal canal, and the initial contours for the rectum should keep the main part away from the rectal lumen in order to avoid unwanted results caused by incorrect intensity statistics. For the segmentation of the levator ani muscles, a proper ROI is critical for the two-phase segmentation.

The ROI should guarantee that the levator ani muscle is covered completely, and the background should be as simple as possible. However, the two aspects are hard to be achieved simultaneously due to the variable shapes of the muscle and the neighboring tissues. In the experiments, we defined the ROI as the following region:

$$\Omega_0 = \left\{ p=(x,y) \left| \begin{array}{c} \nu_1 a_0 \left(x + \frac{b_0}{2a_0} \right)^2 + c_{\min} - \frac{b_0^2}{4a_0} \le y \le \nu_2 a_0 \left(x + \frac{b_0}{2a_0} \right)^2 + c_{\max} - \frac{b_0^2}{4a_0}, \\ D(p, C_b) > 0, D(p, C_v) > 0, D(p, C_r) > 0, y_{\min} \le y \le y_{\max} \end{array} \right. \right\}, \quad (6)$$

where a_0, b_0 and c_0 are the coefficients of the parabola $y = a_0 x^2 + b_0 x + c_0$ that was used to fit the posterior part of the rectum boundary; ν_1, ν_2, $c_{\min}$, $c_{\max}$, $y_{\min}$, and $y_{\max}$ are parameters that satisfy ν_1, $\nu_2 > 0$, $c_{\max} > c_{\min} > c_0$; C_b, C_r and C_v are the boundaries of bladder, vagina and rectum, respectively. The ROI defined in Eq. (6) is a band next to the rectum with its steepness controlled by the parameters ν_1 and ν_2, and its apexes are controlled by the parameters $c_{\min}$ and $c_{\max}$. The condition $y_{\min} \le y \le y_{\max}$ defines the upper and lower ends of the band, and the conditions $D(p, C_i) > 0$ exclude the three pelvic organs from the ROI.

Given the anatomical relationship between the rectum and the levator ani muscle, using Eq. (6) to define a ROI is flexible. Normally, ν_1 and ν_2 are set to be 1 (one), while the addition of the steep controls is important when the parabola $y = a_0 x^2 + b_0 x + c_0$ is not accurate to reflect the actual shape of the muscle. Figure 1 illustrates the segmentation process of the 5th image referred to in Tables 1-3.

3.2 Parameters

The narrow band method [18] was adopted to improve the computational efficiency when implementing the coupling approach in Eq. (2); hence, the calculations are limited inside a narrow band around each moving contour. For the levator ani muscle, the segmentation is performed inside the ROI that is a narrow band next to the rectum boundary. Therefore, both segmentation algorithms are time efficient. However, as the performances of both algorithms are sensitive to parameters, the time-consuming step is the selection of proper parameters. Nevertheless, the selection is easier when segmenting an image series, as a structure tends to have continuous imaging appearances in the sequential images; and if one can obtain satisfactory results using a

group of parameters, only a small adjustment is required to apply them on the neighboring images. This feature can be verified in Table 1.

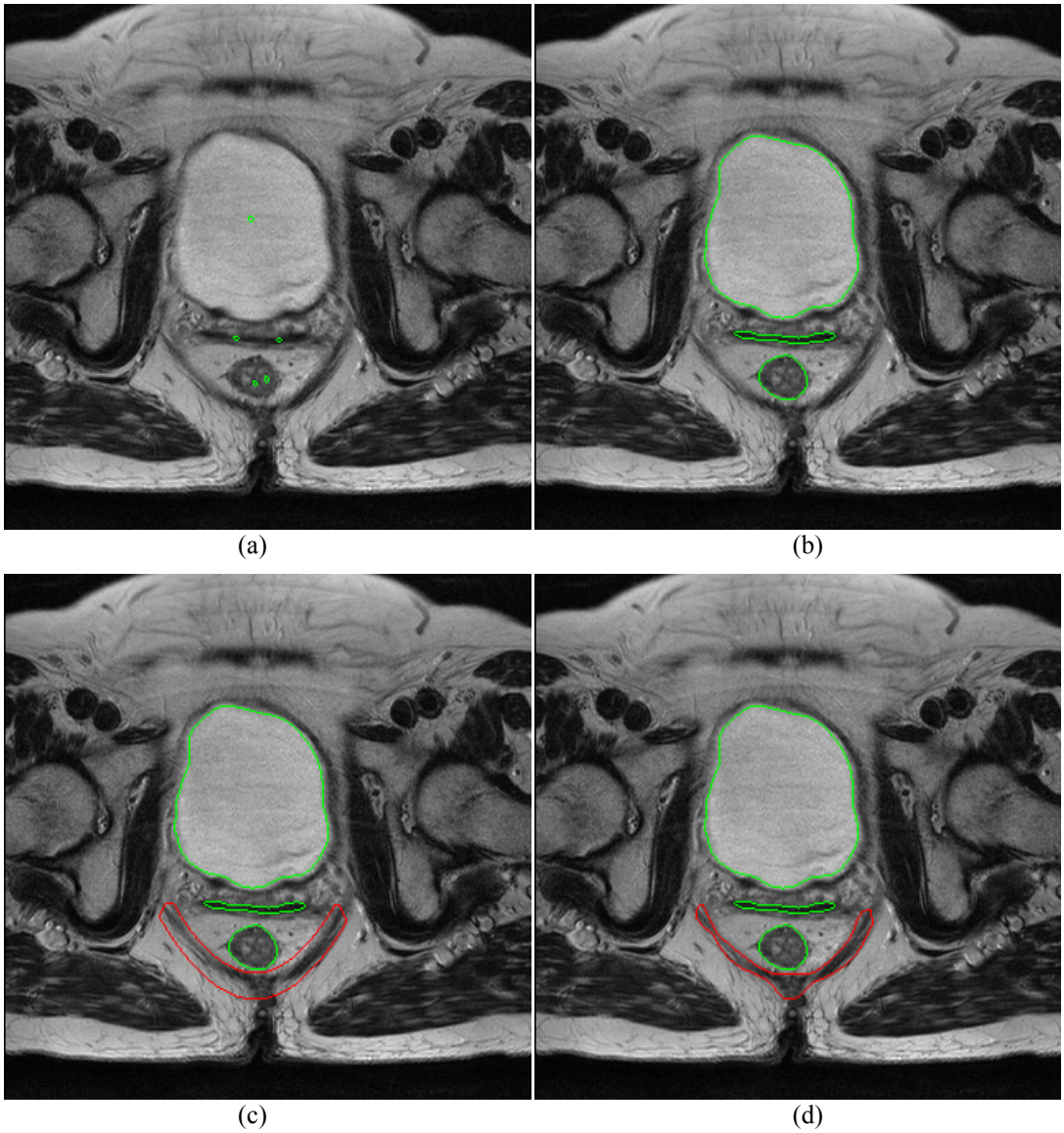

Figure 1: (a) The initial contours (green) placed inside the organs; (b) The contours moved inside the organs and stopped at the organ boundaries. From up to down: bladder, vagina, and rectum; (c) The ROI (enclosed by the green contour) is defined based on the boundaries of the pelvic organs, and the initial contour is defined as the boundary of the ROI (the green contour); (d) The contour moved inside the ROI and stopped at the boundary of the levator ani muscle.

There is no efficient automatic way to select the parameters involved in the algorithms. For the pelvic organs, the parameters γ_i, with $i = 1, 2, 3$, in Eq. (2) affect the smoothness of the moving contours; the parameters α_i play the role of assisting the segmentations. Therefore, the six parameters have minor influence on the contour movement, and their values were fixed as $\alpha_i = -0.1$ and $\gamma_i = -1$ in the experiments. The parameters that influence the segmentation appreciably are the parameters β and

ν, which control the balance between the forces derived from appearance comparison and prior shape guidance. As discussed in Section 2, the weight for shape influence should not be too large since normal shape variation is allowed; but if an image was severely distorted, the weight of shape influence should be increased to assist the contours to move to the correct positions. For example, starting from the 5th image to the 8th image in the series, the appearances of the vagina were blurred due to the partial volume effect; therefore, the weights of the prior shape influence we used were larger than other images. Table 1 shows the values of parameters used in the experiments, together with the mean intensity values of the pelvic organs and the levator ani muscle, from which one can check the different intensity distributions of the structures.

Table 1 Parameters used in the segmentation and the mean intensities of the pelvic structures (LA: levator ani; N: data not available)

Figure	β	ν	λ_3	Mean Intensity			
				Bladder	Vagina	Rectum	LA Muscle
1	0.5	0.8	2	N	34.6	61.2	60.5
2	1	1	2	107.4	46.6	76.8	75.4
3	1	1	2	197.0	51.2	87.2	71.1
4	1	1	2	164.3	36.7	70.1	61.5
5	1	1	2	163.1	44.5	77.5	76.0
6	1	0.8	1	165.2	46.2	66.5	82.1
7	1	0.8	1	175.0	41.4	57.3	84.4
8	1	0.8	1	154.2	29.7	49.7	62.7
9	0.5	0.8	1	142.6	36.8	47.3	59.4
10	0.5	0.8	1	129.9	22.0	46.0	51.5
11	0.5	0.8	1	148.3	21.6	51.6	57.9
12	0.5	0.8	1	132.3	19.9	52.7	52.8

For the levator ani muscle, the mean intensity of the levator ani muscle was fixed as $c_1^* = 60$. Due to the wide range of the intensity values, the magnitudes of the intensity variations inside and outside the moving contour are normally much larger than those of the contour curvature and shape influence field. Correspondingly, the parameters λ_1 and λ_2 are quite small compared to μ and λ_3. The selection of λ_1 and λ_2 depends on the image contents; here, as the background of the ROI had a large intensity variation, parameter λ_2 should be smaller than λ_1; their values were fixed as $\lambda_1 = 0.001$ and $\lambda_2 = 0.0002$ in the experiments. The values of λ_3 used in the

experiments are shown in Table 1; as the images are blurred appreciably, and the levator ani muscles were close to the rectum on the 1st image to the 5th image, the weights of the shape influence field were set to be larger than in the rest of the images.

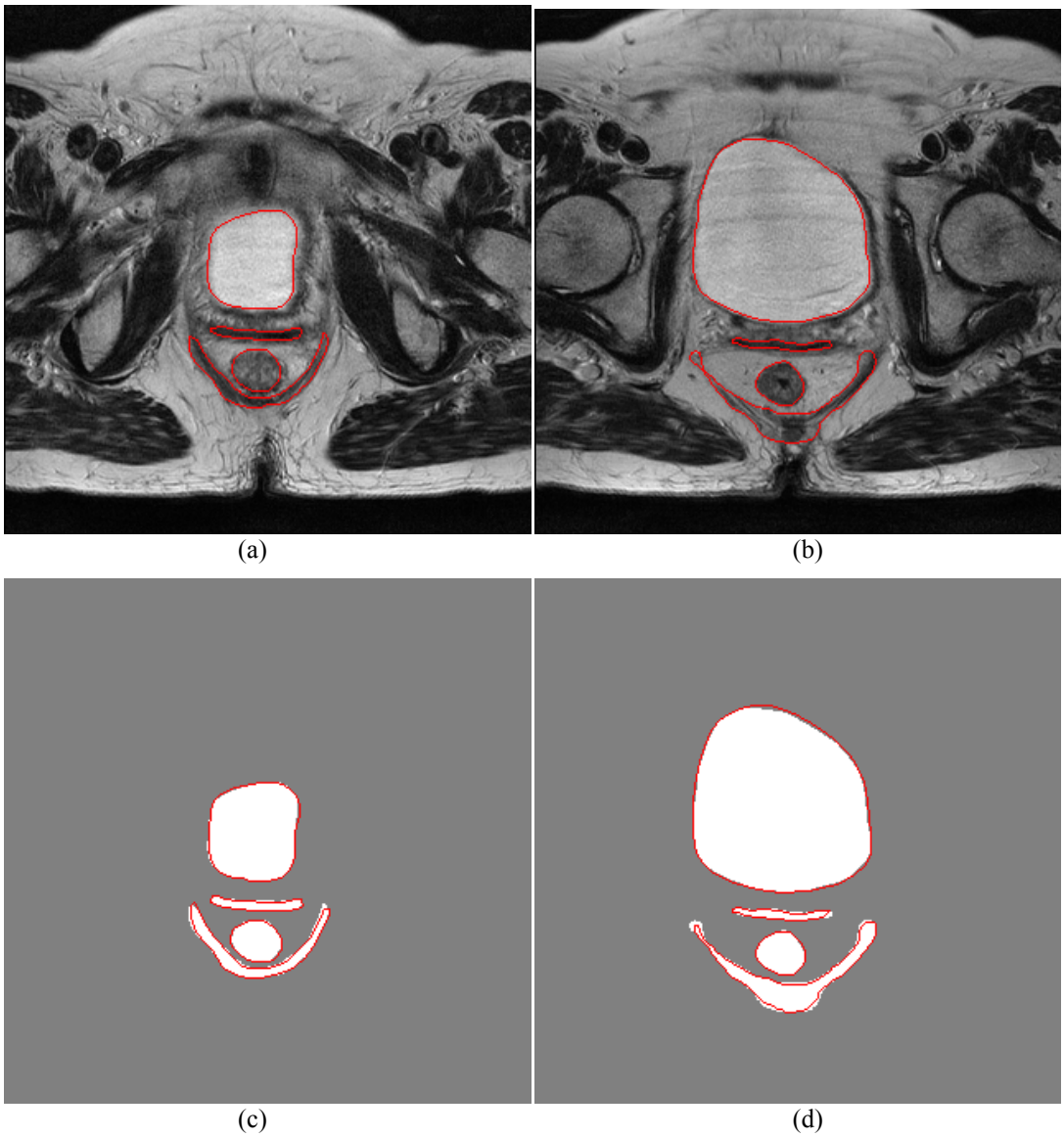

(a) (b)

(c) (d)

Figure 2: (a) and (b): Segmentation results using the algorithms, from up to down: bladder, vagina, rectum, and levator ani muscle; (c) and (d): Segmentation results (with white color representing the internal region of the contours) overlapped with the ground truths (red contours).

4. Results

The image series used in the experiment were not severely affected by noise; however, the intensity variation of each pelvic structure was appreciable. Figures 2(a) and (b) illustrated two segmentation results (corresponding to the 3rd and 6th images referred to in the Tables). For the bladder, the moving contours passed the regions with large intensity variations and stopped at the blurred parts of the boundary where the

intensity gradients were weak. Hence, the inhomogeneous intensity distributions of the pelvic organs were well handled by the coupling approach through the region-based external forces. For the vagina, the central high intensity strips were almost invisible on most of the images; as a result, the vagina appeared as a thin strip with parts of its boundary distorted by noise and partial volume effect. Only based on the appearance comparisons would have led to incorrect segmentations. The prior shape is then critical to guide the contour to the boundary, and the algorithm achieved satisfactory results. For the rectum, the different layers with distinct appearances can be clearly seen on the images. Nevertheless, the moving contours passed the inner boundaries and moved to the correct boundaries under the two external forces. With the boundaries of the pelvic organs, the levator ani muscles were also efficiently segmented by using the shape guided C-V model; the obtained boundary is a single connected curve, and its upper part excludes the connective tissues.

4.1 Analysis

To evaluate the performance of the algorithms, the segmentation results were compared against the manual segmentations. In Figures 2(c) and (d), the boundaries of the pelvic structures in Figures 2 (a) and (b) are overlapped with the ground truths in order to show the deviations intuitively. In order to compare the obtained boundaries with the ground truths, the Hausdorff distance $D(C_0, C_1)$ and the mean value of distance $D(p, C_1)$ were used, where C_0 is the ground truth, C_1 is the segmented boundary, and $p \in C_0$. The point-to-contour distance was calculated as:

$$D(p, C_1) = \min_{p_1 \in C_1} d(p, p_1), \tag{7}$$

where $d(p, p_1)$ is the Euclid distance between two points; and the Hausdorff distance is calculated as:

$$D(C_0, C_1) = \max\left(\max_{p \in C_0} D(p, C_1), \max_{p \in C_1} D(p, C_0) \right). \tag{8}$$

The Hausdorff distance can reflect the maximum deviation of the segmentation result, while the mean value of the distance in Eq. (7) can reflect the average point-to-point matching between the two contours.

Additionally, the region coverage ratio (*CR*) was used to indicate the region matching between the results and the ground truth, which was defined as:

$$CR(C_0, C_1) = \frac{\text{Area}\left(inside(C_0) \cap inside(C_1)\right)}{\text{Area}\left(inside(C_0) \cup inside(C_1)\right)}. \quad (9)$$

The value of $CR(C_0, C_1)$ can show whether the segmented regions are correct or not, and also reflects the influence on the calculation of the cross-sectional areas of the relevant pelvic structures. The results of the comparison of the 12 images are presented in Tables 2 and 3.

Table 2 Quantitative analysis of the segmentation results using point-to-point matching (HD: Hausdorff distance; Mean: the mean value of the point-to-contour distance; LA: levator ani; N: data not available)

No.	Bladder		Vagina		Rectum		LA Muscle	
	HD (mm)	Mean (mm)	HD (mm)	Mean (mm)	HD (mm)	Mean (mm)	HD (mm)	Mean (mm)
1	N	N	1.94	0.64	1.38	0.36	0.97	0.33
2	N	N	0.69	0.13	0.97	0.44	1.94	0.61
3	1.38	0.41	0.97	0.14	0.97	0.39	2.17	0.30
4	2.48	0.51	0.69	0.09	1.38	0.37	2.17	0.46
5	3.07	1.07	0.69	0.07	1.38	0.50	0.97	0.23
6	2.06	0.70	0.69	0.12	0.97	0.29	2.17	0.26
7	1.38	0.57	0.69	0.04	0.97	0.33	2.06	0.24
8	1.38	0.47	0.69	0.37	0.69	0.18	6.81	0.30
9	2.75	0.49	2.17	0.48	0.69	0.25	5.37	0.34
10	4.01	0.81	2.75	0.63	1.54	0.53	1.54	0.36
11	3.44	0.70	1.54	0.68	0.97	0.35	1.94	0.26
12	1.54	0.89	1.38	0.65	1.94	0.53	4.61	0.30

4.2 Pelvic organs

The bladder did not appear on the first image; instead, the urethra with a low signal intensity appearance was presented with the vagina, rectum and levator ani muscle. Hence, the coupling approach could not be used directly. However, based on the intensity statistics of the bladder in the 3rd image, the vagina and the rectum were still segmented successfully. The 2nd image was acquired at the base of the bladder where the bladder connects to the urethra. The central region of the bladder has low signal intensities; therefore, the segmented bladder boundary is not correct. Nevertheless, the vagina and rectum were segmented successfully. For the other 10 images, the three pelvic organs were segmented effectively by the coupling approach, and the results are quantitatively satisfactory. From Tables 2 and 3, one may verify the coverage ratio of the bladder on the last image which was lower than the others. This is because the

image was acquired at the upper end of the urinary bladder. Accordingly, the region and area is smaller than other parts; a small disturbance will cause large deviation to the coverage ratio defined in Eq. (9). Similar cases happened to the vagina and levator ani muscle. Due to the prior shape guidance, the thin appearance of the vagina and the multilayer of the rectum did not appreciably interrupt the completeness and continuity of the segmentation results. On the 1st image, parts of the vagina boundary were erased due to the thin appearances of its left and right sides, which caused a low region coverage ratio of this image. In the 12th image, the intensity of the muscular layer of the rectum varies too much, and caused a deviation of the obtained boundary; therefore, the quantitative measurements of this image were not as good as the others. On the whole, the segmentation results of the pelvic organs were satisfactory.

Table 3 Quantitative analysis of the segmentation results using region matching (CR: region coverage ratio defined in Eq. (9); N: data not available)

No.	CR			
	Bladder	Vagina	Rectum	Levator Ani Muscle
1	N	0.69	0.93	0.90
2	N	0.94	0.92	0.80
3	0.96	0.92	0.93	0.87
4	0.96	0.93	0.93	0.83
5	0.94	0.95	0.90	0.92
6	0.96	0.91	0.94	0.91
7	0.97	0.98	0.94	0.93
8	0.98	0.87	0.97	0.87
9	0.97	0.90	0.95	0.86
10	0.94	0.86	0.90	0.85
11	0.93	0.85	0.92	0.90
12	0.85	0.84	0.88	0.82

4.3 Levator ani muscle

Both the ROI and the shape influence field in the segmentation algorithm are related to the organ boundaries. Therefore, the segmentation of the levator ani muscle is affected by the correctness of the segmented organ boundaries. For the tested images, the segmentation of the muscle also achieved satisfactory results. The only problem was that the parameters in Eq. (6) needed to be adjusted frequently in order to exclude the influence of neighboring tissues, and at the same time keep the simplicity of the ROI. The large Hausdorff distances on the 8th, 9th, and 12th images in Table 2 were due to the low resolution of the middle posterior ends of the muscle on the axial plane

bundles; the thin muscle bundles were erased due to the smoothing effect of the internal force of the algorithm.

4.4 3D reconstruction

Based on the two-dimensional (2D) contours obtained from the 12 images, polygonal meshes were generated using the marching cubes algorithm [19] and smoothed by the Laplacian filter. The partial built 3D models of the pelvic organs and the levator ani muscle are depicted in Figure 3, from which one can see intuitively the spatial relationships between the pelvic structures, the deformation of the vagina under the pressure of the bladder, and their anatomical properties.

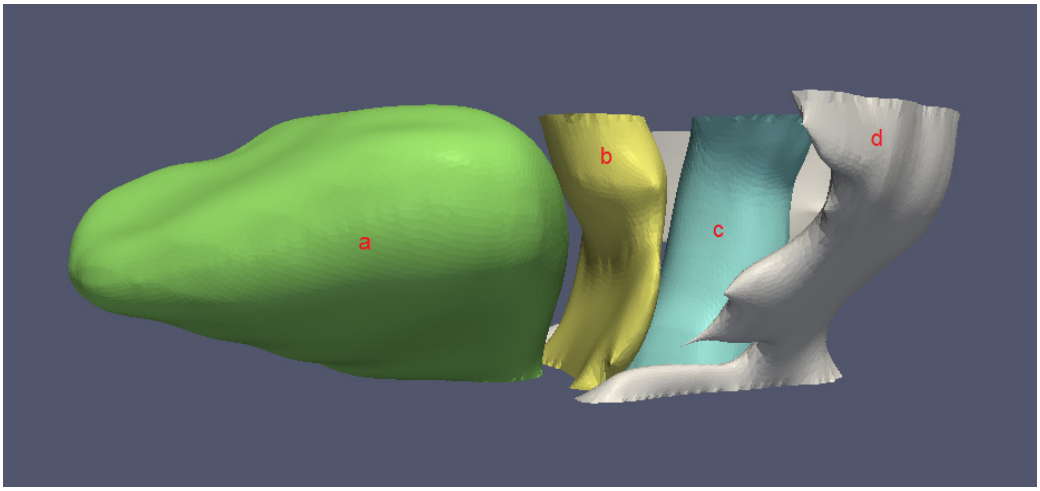

(a)

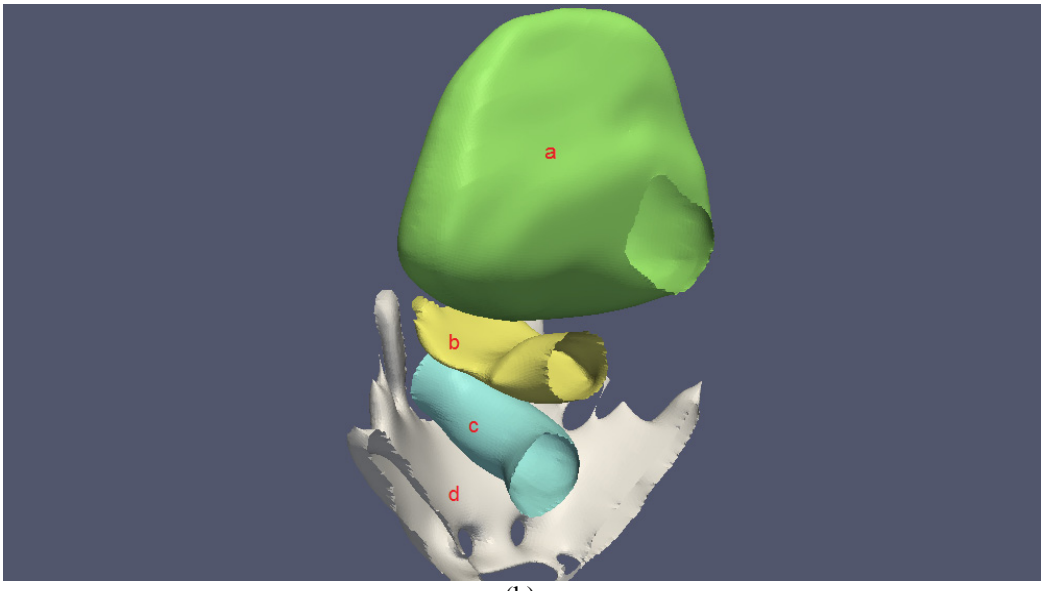

(b)

Figure 3: The 3D models of the pelvic organs and levator ani muscle built from the 12 images. (Labels: a – Bladder, b – Vagina, c – Rectum, and d – Levator ani muscle.)

In order to verify the influences of 2D contours on the 3D reconstruction, the partial volume and surface area of each structure were calculated, as they are frequently involved in the diagnoses and evaluations as, for example, in [20, 21]. Table 4 indicates the two indices of the 3D models built from the results of algorithms and from the manual segmentation, and one can verify that the two measurements of the reconstructed 3D models are also satisfactory.

Table 4 Quantitative analysis of the 3D models (ALG – 3D Model based on the segmentation algorithms; MAN – 3D Model based on the manual segmentation; V – Volume; SA – Surface Area; LA – Levator Ani)

	Bladder		Vagina		Rectum		LA Muscle
	V (cm^3)	SA (cm^2)	V (cm^3)	SA (cm^2)	V (cm^3)	SA (cm^2)	SA (cm^2)
ALG	173.45	161.17	11.95	41.33	15.64	35.19	129.18
MAN	175.21	162.21	11.12	40.37	15.26	34.85	125.33

5. Conclusion

Using the algorithms proposed in [10, 11], the contour movements were not sensitive to the local image intensity variation. For the pelvic organs, the movement of each contour depends on the appearance comparison and the guidance of the prior shapes; the initial contours were defined inside the organs, so that the movement was not affected by the neighboring tissues. For the levator ani muscle, the segmentation using the shape guided C-V model is based on the difference between the imaging appearances of the muscle and the background; the anatomical relationship between the organs and muscle is used to assist the segmentation. The current segmentation algorithms provide effective ways to segment the female pelvic cavity on axial T2-weighted MR images. If images are not distorted severely by noise and partial volume effect, these algorithms can obtain satisfactory results.

On the other hand, one can see that the complex anatomy of female pelvic cavity is a great challenge for automatic segmentation. The comparative results shown in Tables 1-4 indicate that although the algorithms achieved a satisfactory performance for most of the images, there are still many aspects that need to be improved. For example, how to improve the reliability of the algorithms when processing images in which the imaging appearances or shapes of the relevant pelvic structures are changed due to diseases; and how to set the parameters automatically and make the algorithms less sensitive to the parameters. Future works should focus on these aspects, and also

to study how the quality of the segmented 2D contours affects the biomechanical simulations that are based on the 3D models of the pelvic structures.

Acknowledgements

This work was partially done in the scope of the projects "Methodologies to Analyze Organs from Complex Medical Images – Applications to Female Pelvic Cavity", "Aberrant Crypt Foci and Human Colorectal Polyps: mathematical modelling and endoscopic image processing" and "Cardiovascular Imaging Modeling and Simulation – SIMCARD", with references PTDC/EEA-CRO/103320/2008, UTAustin/MAT/0009/2008 and UTAustin/CA/0047/2008, respectively, financially supported by Fundação para a Ciência e a Tecnologia (FCT) in Portugal.

The first author would like to thank FCT for his PhD grant with reference SFRH/BD/43768/2008.

References

[1] Jelovsek JE, Maher C, Barber MD. 2007. Pelvic organ prolapse. Lancet. 369(9566):1027-1038.

[2] Weidner AC, Barber MD, Visco AG, Bump RC, Sanders DB. 2000. Pelvic muscle electromyography of levator ani and external anal sphincter in nulliparous women and women with pelvic floor dysfunction. Am J Obstet Gynecol. 183(6):1390-1401.

[3] Buchsbaum GM, Duecy EE, Kerr LA, Huang LS, Guzick DS. 2005. Urinary incontinence in nulliparous women and their parous sisters. Obstet Gynecol. 106(6):1253-1258.

[4] Nelson R, Norton N, Cautley E, Furner S. 1995. Community based prevalence of anal incontinence. J Am Med Assoc. 274(7): 559-561.

[5] Macmillan AK, Merrie AEH, Marshall RJ, Parry BR. 2004. The prevalence of fecal incontinence in community-dwelling adults: a systematic review of the literature. Dis Colon Rectum. 47(8):1341-1349.

[6] Barentsz JO, Jager GJ, Witjes JA, Ruijs JHJ. 1996. Primary staging of urinary bladder carcinoma: the role of MRI and a comparison with CT. Eur Radiol. 6(2):129-133.

[7] Paramasivam S, Proietto A, Puvaneswary M. 2006. Pelvic anatomy and MRI. Best Pract Res Cl Ob. 20(1):3-22.

[8] Ma Z, Jorge RNM, Mascarenhas T, Tavares JMRS. 2011. Novel approach to segment the inner and outer boundaries of the bladder wall in T2-weighted magnetic resonance images. Ann Biomed Eng. 39(8):2287-2297.

[9] Ma Z, Tavares JMRS, Jorge RNM, Mascarenhas T. 2010. A review of algorithms for medical image segmentation and their applications to the female pelvic cavity. Comput Method Biomec. 13(2):235-246.

[10] Ma Z, Jorge RNM, Mascarenhas T, Tavares JMRS. Segmentation of magnetic resonance images from female pelvic cavity. Proceedings of the 2nd international conference on computational & mathematical biomedical engineering, P. Nithiarasu, R. Löhner (Eds.), Washington D.C., USA, 2011.

[11] Ma Z, Jorge RNM, Tavares JMRS. 2010. A shape guided C-V model to segment the levator ani muscle in axial magnetic resonance images. Med Eng Phys. 32(7):766-774.

[12] Osher SJ, Sethian JA. 1998. Fronts propagating with curvature-dependent speed: algorithms based on Hamilton-Jacobi formulations. J Comput Phys. 79(1):12-49.

[13] Cremers D, Rousson M. 2007. A review of statistical approaches to level set segmentation: integrating color, texture, motion and shape. Int J Comput Vision. 72(2):195-215.

[14] Xie XH, Mirmehdi M. 2008. MAC: magnetostatic active contour model. IEEE T Pattern Anal. 30(4):632-646.

[15] Brox T, Weickert J. 2006. Level set segmentation with multiple regions. IEEE T Image Process. 15(10):3213-3218.

[16] Caselles V, Kimmel R, Sapiro G. 1997. Geodesic active contours. Int J Comput Vision. 22(1):61-79.

[17] Chan TF, Vese LA. 2001. Active contour without edges. IEEE T on Image Processing. 10(2):266-277.

[18] Adalsteinsson D, Sethian JA. 1995. A fast level set method for propagating interfaces. J Comput Phys. 118(2):269-277.

[19] Lorensen WE, Cline HE. Marching cubes: a high resolution 3D surface construction algorithm. Proceedings of the 14th annual conference on computer graphics and interactive techniques, 1987.

[20] Hakenberg OW, Ryall RL, Langlois SL, Marshall VR. 1983. The estimation of bladder volume by sonocystography. J Urology. 130(2):249-251.

[21] Pendergrass PB, Belovicz MW, Reeves CA. 2003. Surface area of the human vagina as measured from vinyl polysiloxane casts. Gynecol Obstet Inves. 55(2):110-113.

Part B – Article 6

A Comparison between Segmentation Algorithms for Urinary Bladder on T2-weighted MR Images

Zhen Ma, Renato Natal Jorge, João Manuel R. S. Tavares

Published in: Proceedings of the III ECCOMAS Thematic Conference on Computational Vision and Medical Image Processing.
CRC Press, Taylor & Francis, 371-376, 2011.

Abstract

The urinary bladder on T2-weighted MR images has a high signal intensity appearance, which can be clearly identified from the neighboring structures. However, due to the complex imaging background, the appearance of the bladder is frequently influenced by noise and partial volume effect. Different algorithms have been proposed to segment the bladder. Nevertheless, these algorithms are at their beginning phases, and considerable improvements are needed to obtain an effective automatic segmentation algorithm. In this paper, the performances of four algorithms are evaluated using a case study, from which the effectiveness and the differences between the algorithms are discussed. Quantitative analysis of the segmentation results are pre-sented to measure the deviations of the segmentation results and reflect the aspects that need to be improved.

1. Introduction

Magnetic resonance imaging (MRI) can provide a clear visualization of the urinary bladder [1]. However, the acquired image series are projections on two dimensional planes; therefore, the shape and geometry information of the bladder are not continuous. In order to study bladder-related conditions, critical indexes such as bladder wall thickness and bladder volume are needed. Accordingly, an accurate segmentation of the bladder on MR images is demanded.

T2-weighted MR images were chosen for this study because the bladder lumen has a high signal intensity appearance on these images and can be easily identified from the low-signal-intensity bladder wall and its neighboring structures. However, due to the influence of noise and partial volume effect, the intensity distribution of the bladder lumen is usually inhomogeneous. Various imaging clues have been adopted in different algorithms to segment this delicate organ. For example, the approach proposed in [2] can achieve good performances us-ing geometric deformable models with region-based external forces. Nevertheless, the current algorithms are in their incipient phases, and considerable works are needed to improve the aspects such as the reliability and automation of the algorithms. A comparison and discussion on the performances of these algorithms then become meaningful.

The algorithms to be evaluated in this study include a thresholding region growing algorithm, a C-means algorithm and two recent approaches pro-posed in [2, 3]. The four algorithms were selected because of their effectiveness to segment the bladder on T2-weighted MR images.

This paper is organized as follows: in Section 2, the segmentation algorithms are reviewed; then, in Section 3, the performances of the algorithms are evaluated and discussed; finally, in Section 4, the paper is concluded and the future works are indicated.

2. Segmentation Algorithms

2.1 Region growing algorithm

Region growing algorithms belong to the threshold-based algorithms [4], in which the threshold values play an important role for segmentation. The thresholds in the region growing algorithms can be defined empirically or by initial seeds; the latter way of definition was chosen in the first region growing algorithm proposed in [5]. Given the complex imaging background on T2-weighted MR images and the intensity distributions of the bladder lumen, we adopted the rule to group the pixels with similar intensities into one class using pre-defined intensity thresholds. Hence, after the selection of the initial seeds, the region starts to merge the neighboring pixels of which the intensities are within the range defined by the thresholds. The merging stops when all the neigh-boring pixels at the front of the region have intensities that are outside the normal range. Therefore, all the pixels inside the segmented region have intensities within the range $[I_{\min}, I_{\max}]$, where $I_{\min}$ and $I_{\max}$ are two pre-defined thresholds. The initial seeds of this algorithm are required to be inside the bladder lumen.

A prior knowledge of the intensity distribution of the bladder lumen is needed to define the thresholds. Because of the large contrast between the appearances of the bladder lumen and the bladder wall, the selection of thresholds is not difficult, and the algorithm works well when the images are not severely affected by noise. Besides, this algorithm has high computational efficiency because of the simple merging criterion. However, if the influence of noise is considerable or the appearance of the bladder lumen is appreciably blurred by the partial volume effect, the segmentation result may contain unwanted inner boundaries or leak to the perivesical fat. Figures 1a

and 1b illustrate two results obtained by using this algorithm, from which one can verify that its performance is sensitive to the threshold values.

2.2 *C*-means algorithm

C-means algorithm is an unsupervised classification technique, where C stands for the number of classes. The algorithm aims to minimize the intensity variation of each class. A pixel is assigned to the class of which the mean intensity has the minimal difference to the intensity of the pixel; then, the mean intensity of the class is updated and the pixels are re-assigned. The iteration stops when all the labels of the pixels remain unchanged. The initial assignments of the pixels affect the iteration times. To implement this algorithm, one only needs to define the value of *C*. A small value of *C* may cause over-segmentation, while a large one may cause many inner boundaries.

Nevertheless, in T2-weighted MR images, different structures may have similar appearances. The inhomogeneous intensity distribution can cause holes inside the segmented region. In order to eliminate the unwanted inner boundaries and make the algorithm more robust, spatial relationship between the pixels can be incorporated in the segmentation process. Hence, the Markov random field (MRF) [6] was applied to smooth and post-process the results of the C-means algorithm. Figures 1c and 1d illustrate the segmentation result of the C-means algorithm and the result after being smoothed by using the MRF, respectively. One can see that the *C*-means algorithm result was considerably improved after incorporating the influences from the neighboring pixels by the MRF.

2.3 Coupling approach

The algorithm proposed in [2] is a coupling system composed of three geometric deformable models. Segmentation of the bladder is based on the appearance comparisons with another two pelvic organs: the vagina and the rectum. The three models interact with each other through the intensity statistics of organs, and can segment the three organs simultaneously. The moving equation for the bladder was proposed as:

$$\frac{\partial \phi_1}{\partial t} = \delta(\phi_1)\left(p_1\left(e_1 - \max\left(e_2, e_3, e_1 - 1\right)\right) + \alpha \nabla p_1 \cdot \nabla \phi_1 + \gamma_1 \operatorname{div}\left(\frac{\nabla \phi_1}{|\nabla \phi_1|}\right)\right), \quad (1)$$

where $\phi_1(X,t)$ is the level set function with X the coordinates and t the time; δ is the Dirac function; $e_i = \log(p_i)$, with the probability p_1 of a pixel belonging to the bladder, p_2 to the vagina, and p_3 to the rectum; γ is a parameter and controls the influence of curvature that can smooth the moving contours. The initial level set function $\phi_1(X,0)$ is normally defined as the signed distance function to the initial contours.

In this approach, the intensity statistics of the vagina and rectum are involved in the segmentation of the bladder. The contour movement is based on the comparisons between the logarithms of the probabilities of a pixel to the three pelvic organs. On T2-weighted MR images, the bladder wall has a similar appearance as the muscular layers of the vagina and rectum. Therefore, when the contour arrives at the bladder wall, it will stop moving forward according to the speed function defined in Eq. (1).

To exclude the influence from neighboring pelvic structures, the initial contours are required to be inside the bladder lumen. Based on the appearance comparison, the algorithm is not sensitive to noise and partial volume effect. The coupling approach requires the simultaneous presences of the three pelvic organs. However, when the vagina or the rectum does not appear on the image, the intensity statistics of the two organs can be set to the values obtained from other images. Although this algorithm was proposed for axial T2-wegihted images, it can be applied to segment the bladder on sagittal and coronal MR images given the fix of the intensity statistics of the vagina and rectum.

2.4 Modified geodesic active model

The approach proposed in [3] contains two algorithms: one is a modified geodesic active contour to segment the inner boundary of the bladder wall; and the other is a shape guided model to segment the outer boundary of the bladder. The idea is to change the geodesic active contour [7] from gradient-based to region-based, so as to handle the influence of noise and intensity variations. The moving equation was proposed as:

$$\frac{\partial \phi}{\partial t} = p(I)(1+\kappa)|\nabla \phi| + \lambda \nabla p(I) \cdot \nabla \phi , \qquad (2)$$

where ϕ is the level set function; λ is the weight; κ is the curvature; I is the intensity; p is a Gaussian distribution function defined as:

$$p(I) = \frac{1}{\sqrt{2\pi}\sigma^*} \exp\left(-\frac{(I-\mu)^2}{2\sigma^{*2}} \right),$$

in which the mean intensity μ and the variance σ^* are calculated as:

$$\mu = \frac{\int_\Omega H(\phi(x,y)) I(x,y)\, dxdy}{\int_\Omega H(\phi(x,y))\, dxdy},\ \sigma^* = \max(\sigma, \sigma_0), \text{ with}$$

$$\sigma = \sqrt{\frac{\int_\Omega H(\phi(x,y)) (I(x,y)-\mu)^2\, dxdy}{\int_\Omega H(\phi(x,y))\, dxdy}}, \tag{3}$$

where H is the Heaviside function and σ_0 is a predefined parameter.

The initial contours are required to be inside the bladder lumen. Unlike the original geodesic active contour, the external force of this algorithm is the expanding speed multiplied by the probability density. When the contour moves to the boundary of the bladder, where the intensity is beyond the normal range, it will slow down and attaches to the bladder wall. The modified calculation of intensity variance extends the range of intensity variation, which makes the algorithms flexible. Like the approach in Section 2.3, this algorithm can be used to segment the bladder on sagittal and coronal MR images.

3. Segmentation & Evaluation

A case study was used to evaluate the performances of the four segmentation algorithms. The image data were acquired from a 26-year-old woman under a field strength of 1.5T (TE: 103 ms, TR: 5440 ms, bandwidth: 130 Hz/pixel, FOV: 220×220 mm^2, acquisition matrix: 272×320 and flip angle: 150°). The spatial resolution of the image series is equal to 0.69×0.69×5.40 mm^3. It contains 30 sagittal images, 26 axial images, and 25 coronal images; among them, the bladder can be clearly identified on 17 axial images, 23 sagittal images, and 7 coronal images.

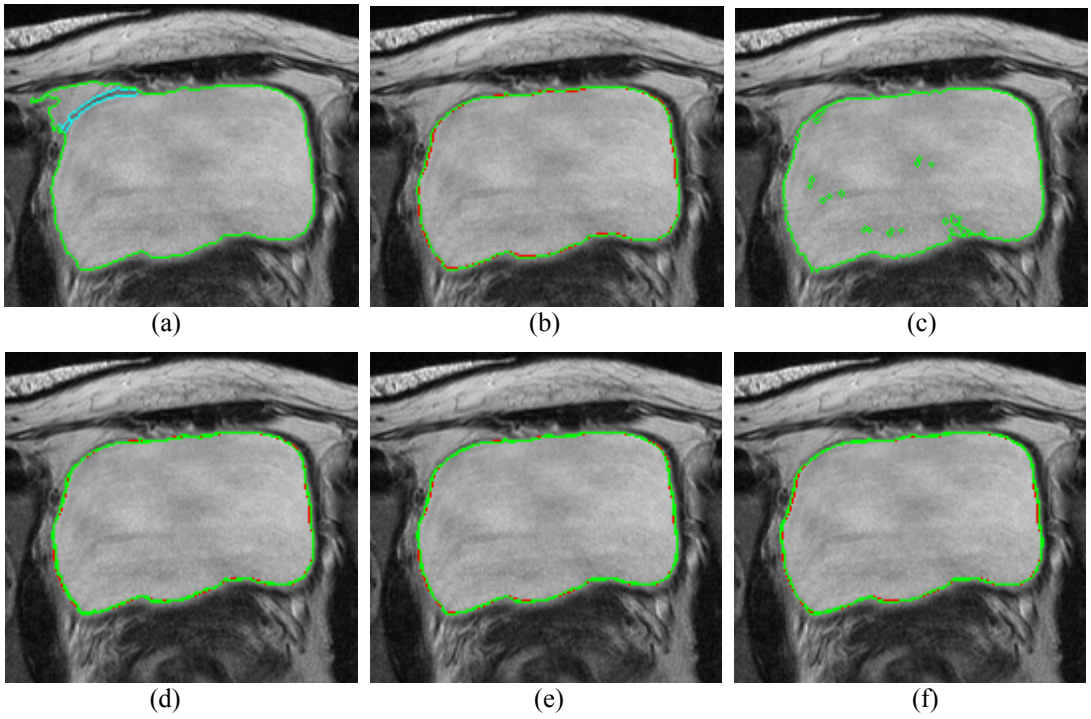

Figure 1: The segmentation results of the four algorithms under comparison: (a) Leakage with the parameters Imin = 130 and Imax = 255 using thresholding region growing algorithm; (b) with parameter Imin = 131 and Imax = 255, overlapped with the ground truth (red line); (c) the segmented boundary using C-means algorithm by classifying the image pixels as 4 clusters; (d) the segmented boundary using C-means algorithm after smoothed by the Markov random field and overlapped with the ground truth (red line); (e) the segmentation result of the coupling approach overlapped with the ground truth; (f) the segmentation result of the modified geodesic active contour overlapped with the ground truth.

3.1 Segmentation

For the thresholding region growing algorithm, the implementation is simple and the computation is efficient. The only requirement is to avoid defining the seeds as the pixels that have intensities beyond the normal range; then, the selections of the initial seeds have no influence to the final result. Given that the bladder wall has a large contrast appearance to the bladder lumen, the thresholding region growing algorithm can achieve good performance on most of the images, as illustrated in Figure 1(a). However, the threshold $I_{\min}$ needs to be adjusted frequently in order to obtain satisfied results. Additionally, when the appearance of the bladder wall is blurred, or the bladder lumen has large intensity variation, the boundary of the bladder cannot be correctly segmented by using this algorithm; an example is shown in Figure 2(a).

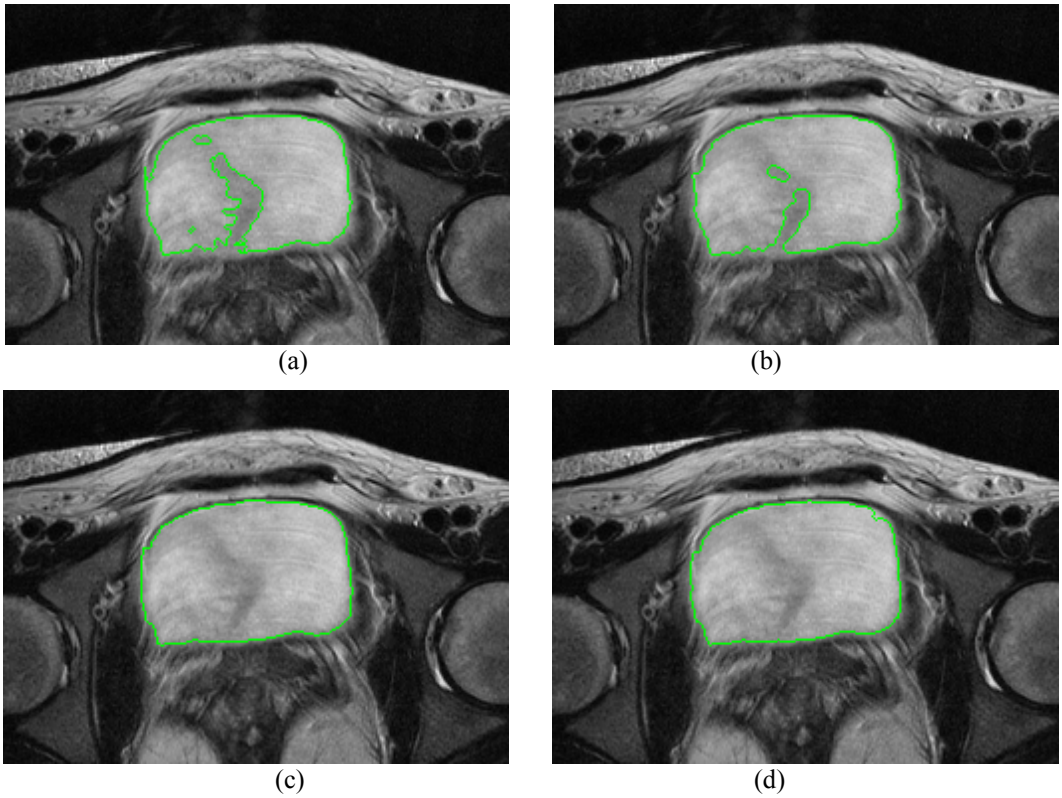

Figure 2: The segmentation results (green line) of the four algorithms on an image with large intensity variance in the center region of the bladder lumen (mean intensity of the bladder region: 168.4; intensity variance: 19.5): (a) thresholding region growing algorithm; (b) C-means algorithm with MRF; (c) the coupling approach; (d) the modified geodesic active contour.

For the C-means algorithm, the number of pixel classes was chosen as 4, so that the bladder lumen can be identified from the bladder wall, and the segmented region contains few inner boundaries. As can be seen from Figure 1, the incorporation of neighborhood information can eliminate the inner boundaries caused by the inhomogeneous intensities of the bladder lumen. The accuracy and robustness of the C-means algorithm are considerably improved. However, when the area of the inhomogeneous region is large, using the MRF the inner boundary cannot be removed without over-segmentation. A case in point can be seen in Figure 2(b).

Due to the coupling of the three deformable models, the coupling approach in Section 2.3 requires longer computation time than the other three algorithms. When the vagina and the rectum cannot be clearly identified, the mean intensities of the vagina were fixed as 40.93 and 37.86, and the variances as 13.23 and 14.22, respectively, which were obtained from an axial image that was correctly segmented by the algorithm. Also, the intensity statistics of the two pelvic organs were set as those values when segmenting the sagittal and axial images. Although on some images those statistical values were not accurate, the segmentation results were not

much influenced, due to the differences between the appearances of the pelvic organs. This strategy worked fine for the tested image series, as confirmed by the later quantitative analysis; however, the performance of this approach on some images was not as good as the modified geodesic active contour, especially when the bladder wall was blurred by the partial volume effect. The Gaussian functions were used as the intensity distribution functions of the pelvic organs, with the means and variances of the image intensity calculated as in Eq. (3). The region-based external forces make the algorithm less sensitive to the influence of noise and partial volume effect; hence, one can see the boundary of the bladder was segmented successfully in Figure 2(c). An example of segmentation on sagittal images is shown in Figure 3(c).

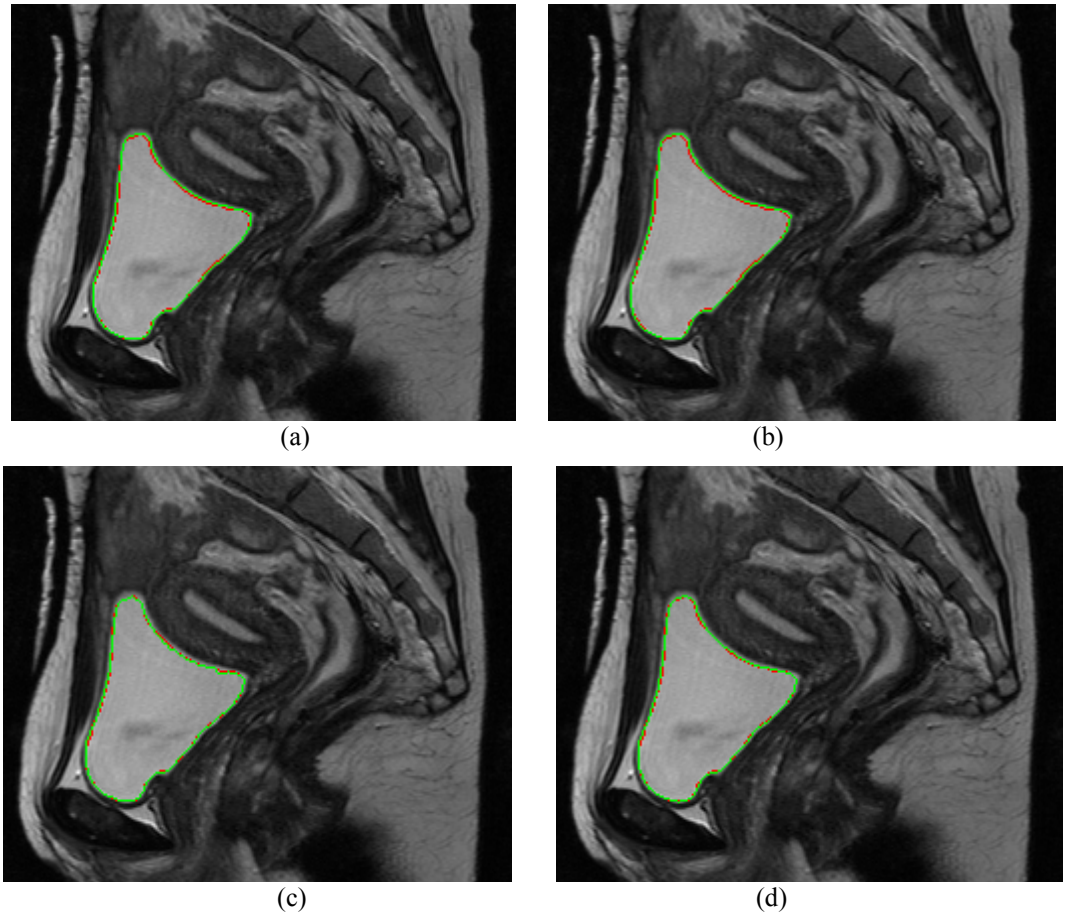

Figure 3: The segmentation results (green line) of the four algorithms on a sagittal image: (a) thresholding region growing algorithm; (b) C-means algorithm with MRF; (c) the coupling approach; (d) the modified geodesic active contour.

The modified geodesic active contour proposed in Section 2.4 achieved satisfied results on the tested images. The modified calculation of the intensity variance makes the algorithm more flexible. Similar to the coupling approach, the region-based external force makes the algorithm less sensitive to noise. Besides, this algorithm does

not rely on the information of other pelvic organs; and its computational time was less than the coupling approach, but higher than the first two algorithms. The overall performance of this algorithm was the best and most accurate among the four algorithms, as was verified in the later quantitative analysis.

3.2 Evaluation

If the influence of noise was moderate on the image, satisfied results could be obtained by the four algorithms; the obtained boundaries had little deviations from the ground truths. However, when the images suffered considerably influence of noise and partial volume effect, the approach proposed in [2, 3] had much better performances; a case in point can be seen in Figure 2.

To evaluate the results of the four algorithms, the images were manually segmented by experienced technicians. The manual segmentations were regarded as the ground truths. The following indices were adopted to measure the deviations of the segmentation results:

$$PD(C_0, C_1) = \underset{p_1 \in C_0}{\text{Mean}}\left(\min_{p_1 \in C_1} d(p, p_1)\right),$$

$$CR(C_0, C_1) = \frac{\text{Area}\left(inside(C_0) \cap inside(C_1)\right)}{\text{Area}\left(inside(C_0) \cup inside(C_1)\right)},$$

$$AD = \frac{\left|\text{Area}\left(inside(C_0)\right) - \text{Area}\left(inside(C_1)\right)\right|}{\text{Area}\left(inside(C_0)\right)}, \tag{4}$$

where C_0 is the ground truth and C_1 is the boundary segmented by algorithm.

The first index assesses the differences between C_0 and C_1 based on the mean distance of the points on C_0 to the points on C_1; it measures the average point-to-point matching between the two contours and indicates whether the segmented boundary matches the correct position. A satisfied segmentation should have a small value of this index. The second index reflects the region matching which checks the correctness of the segmented region. A satisfied segmentation should have a value near to 1.0. The first two indices are complementary and reflect different aspects on the deviations of the segmentation results. The third index is the error ratio of the cross-sectional area of the bladder, which can show the influence of the segmentation results to the quantitative analysis of the bladder lumen. A satisfied result should have a small error ratio.

Table 1 Quantitative analysis of the image illustrated in Figures 1 and 3 (1 – thresholding region growing algorithm; 2 – C-means algorithm with MRF; 3 – Coupling approach; 4 – Modified geodesic active contour; PD, CR, and AD are the indices defined in Eq. (4); a – Figure 1; b – Figure 3).

Methods	PD (mm)		CR		AD (%)	
	a	b	a	b	a	b
1	0.26	0.30	0.99	0.97	1.09	2.65
2	0.24	0.37	0.99	0.97	0.24	3.41
3	0.21	0.13	0.99	0.99	0.03	0.24
4	0.25	0.18	0.99	0.98	1.19	1.54

Accordingly, we present in Table 1 the indices of the four algorithms on Figures 1 and 3, from which one can see the performances of the four algorithms were not much different on the two images, and all the four results were satisfied. To show the overall comparisons among the image series, the mean and variance of the indices on the 23 sagittal images and 15 axial images are presented in Tables 2 and 3, respectively; the axial images did not include the one illustrated in Figure 2, on which using the thresholding region growing algorithm and the C-means algorithm could not obtain a satisfied boundary of the bladder. Therefore, the comparisons were based on the results on the images in which all the four algorithms obtained qualitatively successful results.

Table 2 Quantitative analysis of the sagittal images (1 – thresholding region growing algorithm; 2 – C-means algorithm with MRF; 3 – Coupling approach; 4 – Modified geodesic active contour; PD, CR, and AD are the indices defined in Eq. (4); Var. - variance).

Methods	PD (mm)		CR		AD (%)	
	Mean	Var.	Mean	Var.	Mean	Var.
1	0.36	0.17	0.96	0.03	3.43	3.79
2	0.44	0.19	0.95	0.04	4.79	5.93
3	0.21	0.16	0.98	0.03	2.29	3.73
4	0.17	0.19	0.98	0.02	1.31	1.96

Table 3 Quantitative analysis of the axial images (1 – thresholding region growing algorithm; 2 – C-means algorithm with MRF; 3 – Coupling approach; 4 – Modified geodesic active contour; PD, CR, and AD are the indices defined in Eq. (4); Var. - variance).

Methods	PD (mm)		CR		AD (%)	
	Mean	Var.	Mean	Var.	Mean	Var.
1	0.52	0.32	0.93	0.08	6.73	10.06
2	0.51	0.26	0.94	0.08	5.86	9.43
3	0.41	0.14	0.96	0.02	2.81	2.00
4	0.33	0.10	0.97	0.02	2.37	1.94

3.3 Discussion

The indices in Table 2 are better than the ones in Table 3. The reason is mainly due to the fact that the sagittal images in the image series are less influenced by noise than the axial images. In both cases, the overall performances of the coupling approach and the modified geodesic active contour were satisfied, and were superior to the ones of the thresholding region growing algorithm and the c-means algorithm with MRF.

If the images were not severely influenced by noise and the bladder lumen could be clearly identified from the bladder wall through intensity, the first two algorithms could achieve satisfied results with easy implementation. However, the first algorithm was sensitive to the thresholds; therefore, in order to obtain a satisfied result, the thresholds needed to be adjusted frequently. For the C-means algorithm, the parameters to apply the MRF also needed to be adjusted so as to eliminate the inner boundaries. When handling images with considerable noise and partial volume effect, the performances of the two algorithms were not stable; and sometimes, the boundary could not be segmented correctly by adjusting parameters when such influence was large, like in Figure 2. Another drawback is that the smoothness of the segmented boundary cannot be controlled in the two algorithms, which also contributed to the larger deviation from the ground truths.

On the other hand, due to the incorporation of various imaging clues, the performances of the last two algorithms were stable and less influenced by noise and partial volume effect. For the coupling approach, the appearance comparison assisted the segmentation of the bladder. The smoothing effect of the internal force and the modified variance enlarged its flexibility to handle intensity variations on T2-weighted MR images. The weakness of this algorithm is that the contour movement is related with the intensity statistics of the vagina and the rectum; hence, when the information of the two organs is unavailable or inaccurate, the performance of the algorithm is affected. Also, there are several parameters in the moving equations for segmenting the vagina and rectum, which need to be chosen carefully in order to obtain satisfied results, especially when the images are blurred appreciably by noise and partial volume effect. For the modified geodesic active contour, like the coupling approach, a smooth boundary of the bladder could be obtained; and the region-based external force made the algorithm less sensitive to noise and partial volume effect. The drawback of these two algorithms is that complicated computations are involved, which decreases their computational efficiency.

The differences between the four algorithms became larger when the level of noise and partial volume effect increased. The coupling approach and the modified geodesic active contour were more robust, and their performances were better than the ones of the thresholding region growing algorithm and the C-means algorithm. However, the implementations and the computational complexity of the latter two algorithms are simpler.

4. Conclusion

MR images of urinary bladder provide a clear visualization of this delicate organ. From this study, the current effective algorithms used to segment the bladder on T2-weighted MR images were discussed and compared.

With the quantitative analysis, one could confirm the effectiveness of each segmentation algorithm and identify the aspects that require further improvements. Three indices were used to quantitatively evaluate the performances of the four algorithms. From the experiments, we could verify that the segmentation algorithms could achieve satisfied results, but manual interventions were needed to achieve satisfied segmentations. For the tested image series, the coupling approach and the modified geodesic active contour proposed in [2, 3] obtained better performances than the other two algorithms. However, the four algorithms had common problems, such as the sensitivity to parameter selections and less robustness to process images with severe influence of noise or partial volume effect. Hence, further works are needed to improve these aspects in order to attain more robust and fully automatic segmentation algorithms on T2-weighted axial MR images.

Acknowledgements

This work was partially done in the scope of the projects “Methodologies to Analyze Organs from Complex Medical Images – Applications to Female Pelvic Cavity”, “Aberrant Crypt Foci and Human Colorectal Polyps: mathematical modeling and endoscopic image processing” and “Cardiovascular Imaging Modeling and Simulation - SIMCARD”, with references PTDC/EEA-CRO/103320/2008, UTAustin/MAT/0009/2008 and UTAustin/CA/0047/2008, respectively, financially supported by FCT - Fundação para a Ciência e a Tecnologia, in Portugal.

The first author would like to thank FCT for his PhD grant with reference SFRH/BD/43768/2008.

References

[1] Cheng D, Tempany CMC. 1998. MR imaging of the prostate and bladder. Semin Ultrasound CT. 19(1):67-89.

[2] Ma Z, Jorge RNM, Mascarenhas T, Tavares JMRS. Segmentation of magnetic resonance images from female pelvic cavity. Proceedings of the 2nd international conference on computational & mathematical biomedical engineering, P. Nithiarasu, R. Löhner (Eds.), Washington D.C., USA, 2011.

[3] Ma Z, Jorge RNM, Mascarenhas T, Tavares JMRS. 2011. Novel approach to segment the inner and outer boundaries of the bladder wall in T2-weighted magnetic resonance images. Ann Biomed Eng. 39(8):2287-2297.

[4] Ma Z, Tavares JMRS, Jorge RNM, Mascarenhas T. 2010. A review of algorithms for medical image segmentation and their applications to the female pelvic cavity. Comput Method Biomec. 13(2):235-246.

[5] Adams R, Bischof L. 1994. Seeded region growing. IEEE T Pattern Anal. 16(6):641-647.

[6] Kindermann R, Snell JL. 1980. Markov random fields and their applications. Rhode Island: American Mathematical Society.

[7] Caselles V, Kimmel R, Sapiro G. 1997. Geodesic active contours. Int J Comput Vision. 22(1):61-79.

Part B – Article 7

A Level Set Based Algorithm to Reconstruct the Urinary Bladder from Multiple Views

Zhen Ma, Renato Natal Jorge, T. Mascarenhas, João Manuel R. S. Tavares

Submitted to an international journal (Under review), 2012.

Abstract

The urinary bladder can be visualized from different views by imaging facilities such as Computerized Tomography (CT) and Magnetic Resonance Imaging (MRI). Multi-view imaging can present more details of this pelvic organ and contribute to a more reliable reconstruction. Based on the information from multi-view planes, a level set based algorithm is proposed to reconstruct the 3D shape of the bladder using the cross-sectional boundaries. The proposed algorithm provides a flexible solution to handle the discrepancies from different view planes and can obtain an accurate bladder surface with more geometric details. Influence of each boundary to the reconstruction is evaluated according to its reliability; and the surface is required to approach to these boundaries following its weighted distances. Procedures of the algorithm are explained using a MR image series and the influence of the main parameters are discussed.

Keywords: Biomedical Engineering; Medical Imaging; Image Analysis; Deformable Model; 3D Reconstruction.

1. Introduction

The urinary bladder is a hollow organ at the pelvic cavity and works as a reservoir of the urine propelled from the kidney. A normal bladder has a thin smooth muscular wall that is mainly composed of the detrusor muscle. Dysfunction of the urinary bladder can cause various urological conditions such as cystocele, urinary incontinence (UI), overactive bladder (OAB), and underactive bladder (UAB). Nowadays, the prevalence of these diseases affects a large number of populations; for example, it was estimated that in the United States 16.0% of men and 16.9% of women have OAB and overall 38% of women have symptoms of UI [1, 2]. The negative impacts of the bladder-related conditions can considerably influence the patients' physical and social lives, and need to be treated properly. The diagnosis requires an in-depth understanding of the functionalities of the urinary bladder and its relationship with the involved structures. The modern imaging modalities play an important role in this process and have achieved satisfied results in detecting

conditions [3-8]. For instance, computerized tomography (CT) and magnetic resonance imaging (MRI) have been used as the non-invasive ways to follow the extension of bladder tumors and to stage bladder cancer [3, 4]. Details of the urinary bladder on the cross-sectional plans can be presented clearly; however, information from these two-dimensional image slices is neither continuous nor intuitive due to the slice gaps. In order to carry on further analysis such as biomechanical simulation and quantitative analysis, the three-dimensional (3D) surface model of the urinary bladder needs to be reconstructed.

Usually, using the imaging facilities provided by modern CT and MRI systems, the urinary bladder can be visualized from three spatial views: axial, sagittal, and coronal. Unlike the multi-view stereo reconstruction, the medical image series contain little redundant information because the cross-sectional imaging planes are parallel in the same spatial view and intersectional (in many cases also orthogonal) between different spatial views. The joint information from different views can benefit the reconstruction of the urinary bladder and provide more details to the surface model. In this paper, a level set based algorithm is proposed that combines the information from the multiple views to reconstruct the urinary bladder. The level set method [9] is used to track the surface evolution, and the moving equation is defined based on the weighted distance to the cross-sectional boundaries. The proposed algorithm provides a flexible method for reconstruction and can obtain a reliable bladder surface with more geometric details.

The structure of the paper is as follows: in Section 2, the background and the problem addressed are described; in Section 3, the reconstruction algorithm is introduced and explained; in Section 4, the procedure of the algorithm is explained using a MR image series and the parameters are discussed along with the experimental results; in the last section, the paper is concluded and the future work is summarized.

2. Background

A common procedure for 3D reconstruction is to use the cross-sectional regions of the bladder segmented on the images: a rough profile of the bladder can be sketched through stacking the sequential boundaries from the same spatial view; then, the 3D surface model can be reconstructed using, for example, the marching cubes algorithm

[10]. Therefore, the reliability of a 3D model depends on two critical factors: the accuracy of the segmented regions and the spatial interpolation between neighbouring slices. Regarding the first factor, effective segmentation algorithms have been proposed [11-13] based on the appearances of the bladder in different imaging modalities. Although some aspects of these algorithms still need to be improved, in most cases correct results can be obtained under proper initial conditions; hence, segmentation accuracy is not the focus in this paper. For the second factor, the spatial interpolation is used to recover the missing information at the slice gap. The slice gap is a parameter determined at the imaging phase: the smaller this value is, the more information can be acquired. If the gaps between neighbouring images are small enough, a realistic 3D surface model can be obtained. However, the normal slice gap is much larger than the in-plane imaging resolution given the limitation of the hardware and the large size of the image data; hence, surface model built from a single view may not be accurate due to the lack of information at the gaps. Besides, the imaging appearance of the urinary bladder can be influenced by the neighbouring structures under a certain view so that some geometric properties of the bladder are hard to be observed from these view planes. Image series acquired from multiple views can considerably improve these situations, for the missing information in one view can be compensated by the contents from other views; accordingly, reconstruction based on multiple view planes can obtain a bladder surface model with more and comprehensive details.

If all the images are segmented accurately, the cross-sectional boundaries of the bladder from different views should intersect with each other. Nevertheless, in practical cases, this feature does not hold because the imaging appearance of the bladder can be easily distorted by noise or influenced by the neighbouring organs. A case in point can be seen in Figure 1: the posterior part of the bladder in the axial image is unclear due to the partial volume effect caused by the anterior parts of the vagina; and the bladder boundary in the sagittal image is blurry because the image is acquired at the lateral side of the bladder; consequently, the accuracy of segmentation at these parts cannot be assured. When the boundaries from different view planes are aligned, the correct positions at some parts of the bladder become confused. Figure 2 illustrates two surface models built by the marching cubes algorithm using the axial and sagittal boundaries respectively, from which the discrepancies at the lateral and upper sides of the urinary bladder can be clearly identified. Then, reconstruction with

the cross-sectional boundaries from multiple view planes becomes an ill-posed problem; if all the boundaries are treated equally in reconstruction, the 3D model built may approach to the wrong positions at the parts with discrepancies. Registration of the intersection points between two intersectional boundaries seems to be a proper way to eliminate the discrepancies and establish the correspondence; however, modification of the boundary points can change the local continuity and smoothness and lead to new discordance at other parts of the boundary. Given the number of cross-sectional boundaries, registration requires high computational complexity to find the correspondence matching among boundaries, and is not appropriate for this application. Therefore, the way to build a reliable surface of the urinary bladder based on the information from multi-view planes becomes an interesting topic to explore.

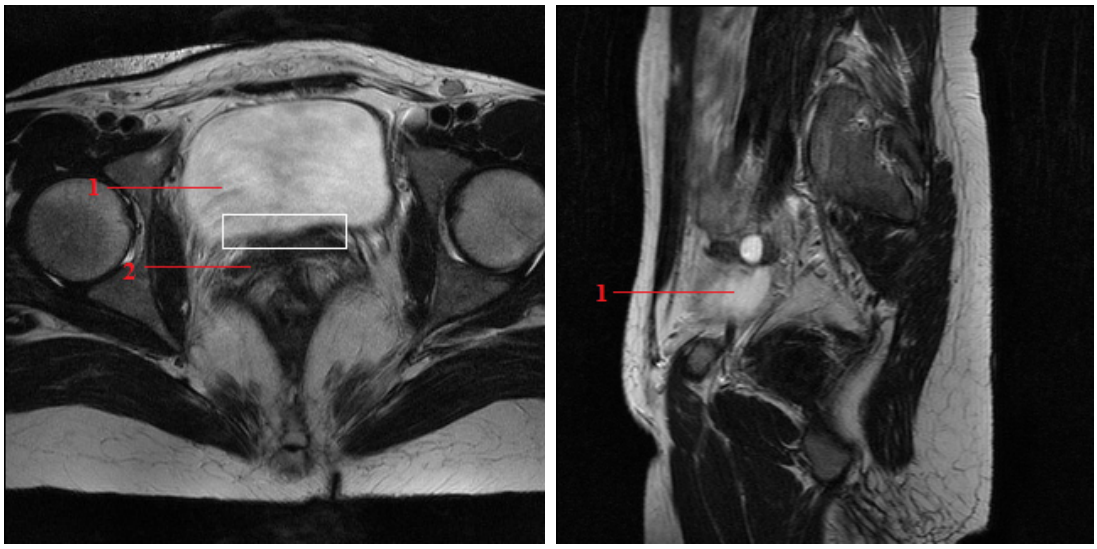

(a) (b)

Figure 1: T2-weighted MR images of the female pelvic cavity in which the boundary of the urinary bladder is unclear: (a) axial view, with the blurred posterior bladder region marked by the rectangle; (b) sagittal view (Labels: 1-bladder; 2-vagina).

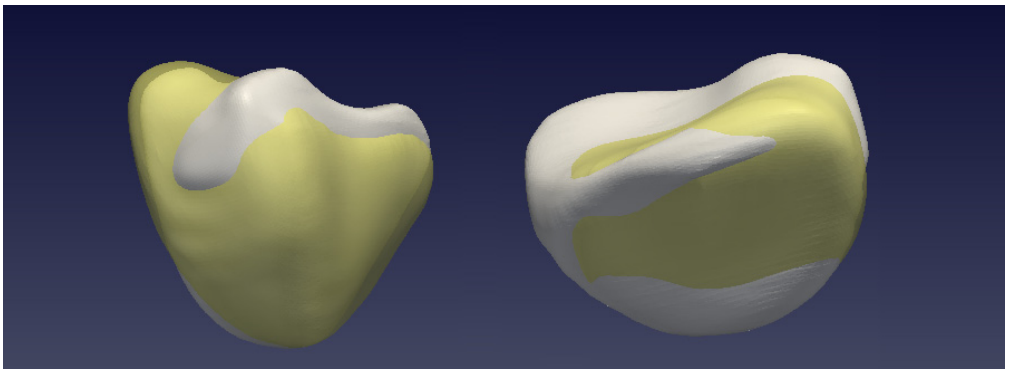

Figure 2: The bladder surfaces built by the marching cubes algorithm using the axial boundaries (with transparent yellow color) and sagittal boundaries (with solid white color).

For the urinary bladder, its lateral boundary can be better identified on axial plane while the dome and the base are more clearly observed on sagittal and coronal planes [14]. Hence, the positions defined by the upper and lower parts of the sagittal boundaries should be more reliable than the ones defined by the axial boundaries; the lateral sides of the bladder are more accurately defined by the axial boundaries. Though these conclusions are not definitive, the reliability of the segmented boundaries can be a useful criterion for handling the confusions in the reconstruction: the surface should approach to the positions defined by the parts with higher reliabilities. With these ideas, a 3D reconstruction algorithm is proposed that combines the complementary information from multi-view imaging planes and meanwhile solves the discrepancies using the different reliabilities of the cross-sectional boundaries. Even though the urinary bladder is concerned in this paper, the functionality of the algorithm can be used to reconstruct other organs with multi-view imaging planes.

3. Algorithm

According to the accuracy of segmentation, the boundary of the urinary bladder on each image can be divided into several parts with each one assigned with a confidence level; as such, the parts with a higher confidence level are more reliable to be used for reconstruction. The bladder surface should have the minimal distance to the cross-sectional boundaries. In the ideal case, this value is zero, which means all the boundaries are on the surface. Given the discrepancies of segmentation from multiple view planes, the distance should approach to zero. To facilitate the discussion, supposing there are $N \geq 1$ confidence levels and the parts of a boundary with *i*-th confidence level have higher reliability than the ones with the *j*-th confidence level when $i < j$; consequently, the energy functional for reconstruction is proposed as follows:

$$E(\Gamma) = \sum_{i=1}^{M} \omega_i \int_{\Gamma} d_i(\vec{x})\, ds + \left(1 - \sum_{i=1}^{M} \omega_i\right) \int_{\Gamma} d(\vec{x})\, ds\,, \tag{1}$$

where Γ is the surface, $d_i(\vec{x})$ is the distance of the surface segment to the parts of boundaries with the *i*-th confidence level, $d(\vec{x})$ is the distance of the surface segment

to all the boundaries, ds is the surface area, M is an integer that satisfies $1 \le M \le N$, and $\omega_i > 0$ is the weight of each distance with $0 \le \sum_{i=1}^{M} \omega_i \le 1$ and $\omega_i \ge \omega_j$ if $i > j$.

The first item at the right side of Eq. (1) emphasizes the importance of the parts with the fore *M*-highest confidence levels to the reconstruction; and the definition of the distance weights ω_i assures that the parts with high confidence levels have larger influences than the ones with low confidence levels. Thus, the surface obtained will be attracted to the positions defined by the boundaries that are more reliable when there are discrepancies. The second item is a distance measure of the surface to all parts of the boundaries and was used in applications such as the point cloud reconstruction [15]; it is added here so that the information from the parts with low confidence levels will not be discarded in reconstruction, and the surface has an overall small distance to all the segmented boundaries. Hence, the bladder surface defined by the proposed energy functional is the one that has the minimal weighted distance to the cross-sectional boundaries.

The Euler-Lagrange equation of Eq. (1) can be derived as:

$$\left(\sum_{i=1}^{M}\omega_i \nabla d_i(\vec{x}) + \left(1-\sum_{i=1}^{M}\omega_i\right)\nabla d(\vec{x})\right)\cdot \vec{N} + \left(\sum_{i=1}^{M}\omega_i d_i(\vec{x}) + \left(1-\sum_{i=1}^{M}\omega_i\right) d(\vec{x})\right)\kappa = 0, \qquad (2)$$

where $\vec{N}$ is the external normal vector and κ is the curvature of the surface. Correspondingly, the moving equation to find the minimal surface is proposed as:

$$\frac{\partial \phi}{\partial t} = \left(\left(\sum_{i=1}^{M}\omega_i \nabla d_i + \left(1-\sum_{i=1}^{M}\omega_i\right)\nabla d\right)\cdot \frac{\nabla \phi}{|\nabla \phi|} + \lambda\left(\sum_{i=1}^{M}\omega_i d_i + \left(1-\sum_{i=1}^{M}\omega_i\right) d\right)\nabla \cdot \frac{\nabla \phi}{|\nabla \phi|}\right)|\nabla \phi|, \qquad (3)$$

where ϕ is the level set function [9] that embeds the moving surface as its zero level set $\phi(x, y, z, t) = 0$. The implicit tracking of the surface by the level set method can facilitate the calculations of the surface changes and decrease the computational complexity. The values of the initial level set function $\phi(x, y, z, 0)$ are defined as the signed distance function to the initial surface, with positive (negative) signs inside (outside).

In the right side of Eq. (3), the first part acts as the external force that defines the direction of movement, following which the surface is attracted to the positions defined by the cross-sectional boundaries; the force is composed of two parts: the first one, $\sum_{i=1}^{M}\omega_i \nabla d_i$, is derived from the *M* subsets of the boundary parts that defines and

influences the moving direction of the surface when there are discrepancies; and the second item, $\left(1-\sum_{i=1}^{M}\omega_i\right)\nabla d(\vec{x})$, is derived from all the boundary parts that drives the surface approaching to the correct positions and assures that no information is missed. The second part, $\left(\sum_{i=1}^{M}\omega_i d_i+\left(1-\sum_{i=1}^{M}\omega_i\right)d\right)\kappa$, acts as an internal force to keep the smoothness of the surface through the influence of curvature; the smoothing effect is controlled by the parameter λ: a larger λ can lead to a smoother surface.

Furthermore, the distance between a surface segment *S* and a contour *L* is defined as:

$$D(S,L)=\min_{p\in S}\left(\min_{p'\in L}\left(d(p,p')\right)\right), \tag{4}$$

where $d(p,p')$ is the Euclidean distance between the points p and p'. As such, the distance between a surface and a contour is calculated as the distance between points. Meanwhile, the assignment of the confidence levels to different parts of the boundaries can be done through sampling the boundaries to discrete points and evaluating these points based on their positions and reliabilities. Accordingly, the calculation of $d(\vec{x})$ and $d_i(\vec{x})$ at a segment Γ' on the surface Γ can be easily carried out by finding the minimal Euclidean distances between the surface points and the sampled boundary points as:

$$d(\vec{x})=\min_{p\in\Gamma'}\left(\min_{p'\in P}\left(d(p,p')\right)\right),$$

$$d_i(\vec{x})=\min_{p\in\Gamma'}\left(\min_{p'\in P_i}\left(d(p,p')\right)\right), \tag{5}$$

where P is the point set composed by all the sampled boundary points and P_i stands for its subset in which the points have the *i*-th confidence level.

The proposed algorithm is based on the cross-sectional boundaries from the multi-view planes using the criterion that the surface should approach to the positions defined by the more reliable segmentations when discrepancy happens. Following Eq. (3), the bladder surface can be obtained through surface evolution, and the reconstruction process is flexible and naturally handles the multi-view discrepancies. The procedure of the proposed algorithm can be summarized as the following steps:

- Step 0: Segment the boundaries of the urinary bladder on the images acquired from each view; align them to the same coordinate system according to the orientation and imaging attributes of each image.
- Step 1: Sample the boundaries into discrete boundary points and assign these points with different confidence levels based on their reliabilities.
- Step 2: Define the initial surface and initialize the values of the level set function using the signed distance.
- Step 3: The initial surface evolves according to Eq. (3) until it becomes stable.

4. Results and Discussions

In order to better explain the procedures and show the influences of the weighted distance, the 3D reconstruction of the urinary bladder from a T2-weighted MR image series is addressed in this section. T2-weighted MRI is preferred in many studies because the bladder wall, urine, and perivesical fat have distinct appearances, which makes the segmentation easier and consequently reduces the possible discrepancies between intersectional boundaries. The image series used was acquired from a 26-year-old woman under a turbo-spin echo (TSE) sequence with the following parameters: patient position: head first-supine (HFS), field strength: 1.5 T, echo time (TE): 103 ms, repetition time (TR): 5440 ms, bandwidth: 130 Hz/pixel, FOV: 220×220 mm^2, acquisition matrix: 272×320, flip angle: 150°, and the spatial resolution is 0.69×0.69×5.40 mm^3 for the axial plane, 4.20×0.81×0.81 mm^3 for the sagittal plane, 0.69×5.40×0.69 mm^3 for the coronal plane. The coordinates of the upper left voxel on each image is recorded following the LPS (Left-Posterior-Superior) system, and the orientation of each view plane can be accessed from the DICOM (Digital Imaging and Communications in Medicine) tags contained in the image series.

4.1 Reconstruction process

Segmentation and alignment: in the image series, the bladder can be clearly identified in 16 axial images, 23 sagittal images, and 8 coronal images; correspondingly, the segmentation was carried out on these images. The segmented boundaries were aligned to the same coordinate system based on the positions and orientations of the imaging planes, as illustrated in Figure 3(a). As a comparison, the profile of the bladder from the sagittal view is shown in Figure 3(b). One can see that the lacking information at the slice gap in the sagittal view is compensated by the contents from

the axial and coronal planes; the sketched profile of the bladder from multiple views is more complete and its laterals can be identified clearly.

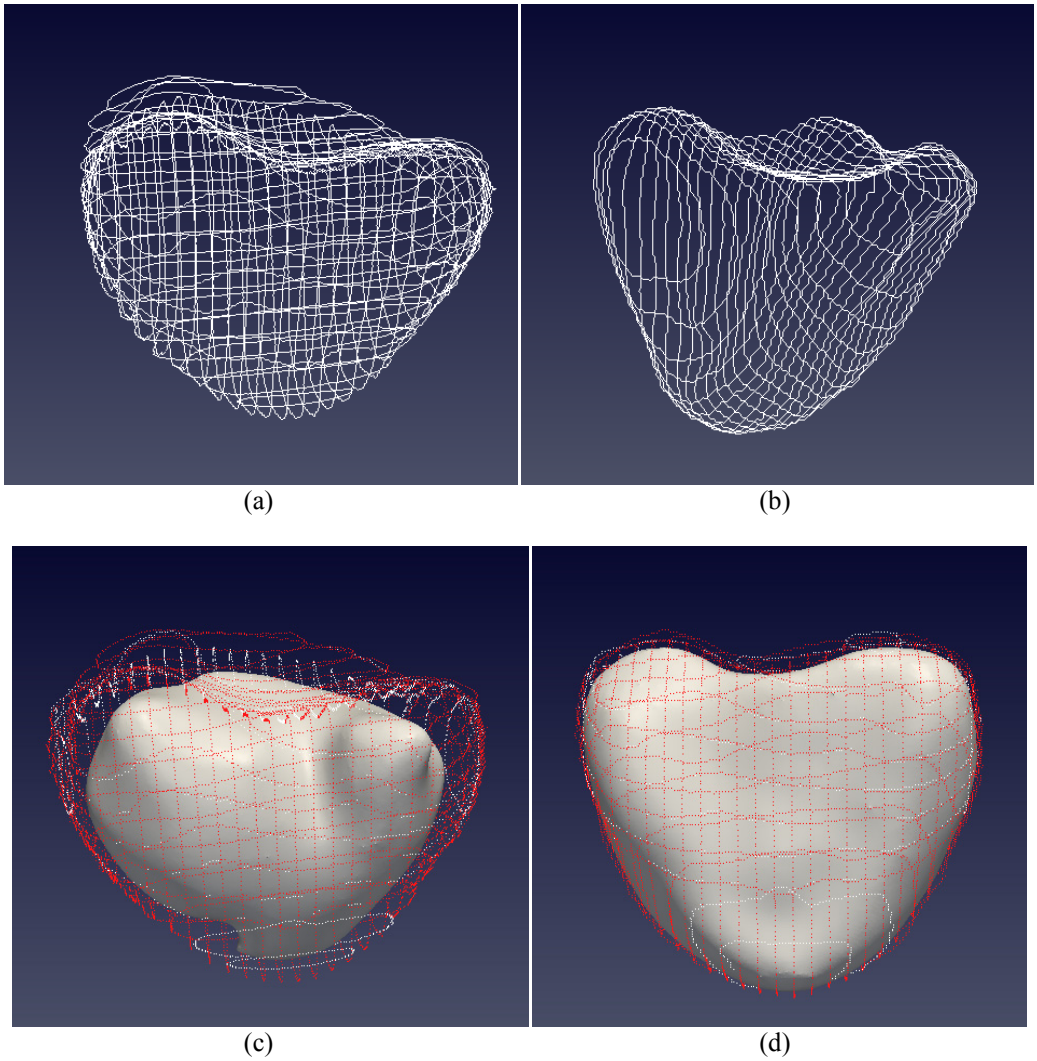

Figure 3: (a) Profiles of the urinary bladder through stacking the sagittal boundaries; (b) Profiles of the bladder by stacking the boundaries from multi-view planes; (c) Sampled boundary points with the initial surface, the ones with high confidence level are highlighted with red color; (d) The bladder surface reconstructed using the proposed algorithm with $\omega = 0.8$.

Sampling and assignment: the cross-sectional boundaries were sampled to discrete points, as shown in Figure 3(c); among them, 4673 points are from the axial boundaries, 4806 from the sagittal boundaries, and 2259 from the coronal boundaries. Only two confidence levels were considered in this example so that the influence of the distance weights can be shown in a clear way. Accordingly, the sampled points were classified into two groups, and the ones that are more reliable were assigned with high confidence level and highlighted with the red color in Figure 3(c) (among

them 4382 points are from the axial plane, 3309 from the sagittal plane, and 2206 from the coronal plane).

Initialization: The initial surface was placed completely in the bladder lumen, as is shown in Figure 3(c); hence, for this experiment, the final surface was obtained through expansion. The level set value $\phi(x, y, z, 0)$ was initialized as the signed distance to the initial surface; the distances of the initial surface to the cross-sectional boundaries and to the boundary parts with high confidence level were calculated using Eq. (5).

Evolution: since only two confidence levels were considered, according to Eq. (3), the moving equation becomes:

$$\frac{\partial \phi}{\partial t} = \left(\left(\omega \nabla d_1 + (1-\omega) \nabla d \right) \cdot \frac{\nabla \phi}{|\nabla \phi|} + \lambda \left(\omega d_1 + (1-\omega) d \right) \nabla \cdot \frac{\nabla \phi}{|\nabla \phi|} \right) |\nabla \phi|, \tag{6}$$

where ϕ is the level set function, d_1 is the distance function of the surface to the boundary points with high confidence level, d is the distance function of the surface to all the sampled boundary points, $0 \le \omega < 1$ is the weight that controls the influence of the points with high confidence level, and λ controls the smoothing effect. Following this equation, the surface evolves and the level set function is updated until it achieves a stable status. The reconstruction attained can be seen in Figure 3(d).

4.2 Discussions

The weighted distance to the cross-sectional boundaries makes the obtained surface no longer the one that has the minimal average distance to the boundaries; consequently, the value of ω in Eq. (6) can influence the appearance of the bladder surface: a larger ω gives higher priority to the points with high confidence level; as such, the surface is required to approach further to the positions defined by them. The changes of the surfaces are illustrated in Figure 4(a), in which the surfaces built with ω = 0.2, 0.4, 0.6, 0.8 were overlapped with the one built with ω = 0 to show their differences intuitively; for example, when ω increases the upper right side of the surface tends to expand further to the new position defined by the points with high confidence level. Meanwhile, the selection of a proper ω is also related to the spatial distribution of the points with high confidence level. In this example, if ω is too large, the information carried by the points with low confidence level tends to be discarded in reconstruction; this situation can be verified in Figure 4(b) that the upper

left parts of the bladder is disappearing when ω = 0.9 and 1.0 due to the lack of points with high confidence level at there. Therefore, if the points with high confidence level have an uneven spatial distribution, the weight of the distance to all the sampled boundary points should not be small in order to keep the integrity and correctness of the surface.

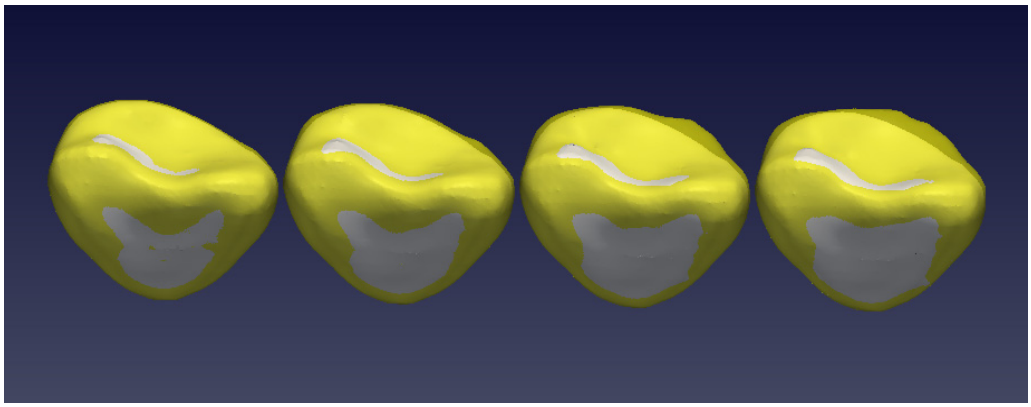

(a)

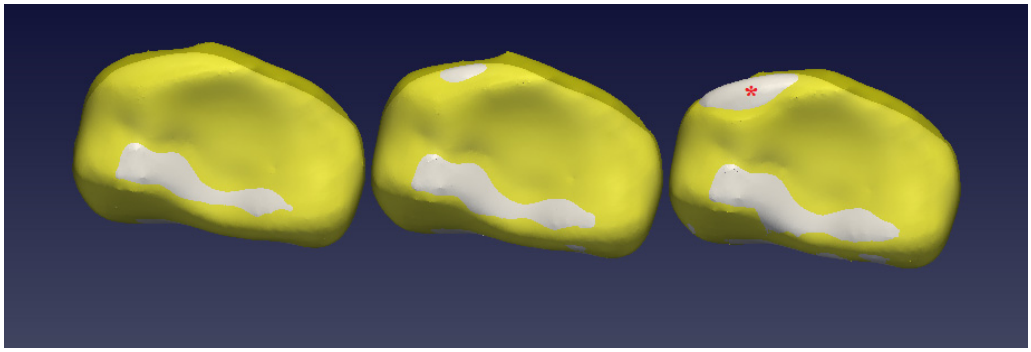

(b)

Figure 4: (a) The bladder surfaces using the proposed algorithm (transparent yellow color) built with ω = 0.2, 0.4, 0.6, 0.8 from left to right overlapped with the surface built with ω = 0 (solid white color, with all the points are treated equally); (b) The bladder surface built with ω = 0.8, 0.9, 1 (only based on the points with high confidence level) overlapped with the surface built with ω = 0, the disappearing region is marked by a red asterisk.

To quantitatively measure the differences among these surfaces, four indexes were used:

$$I_1 = \int_\Gamma d(\vec{x})\,ds,\ I_2 = \int_\Gamma d_1(\vec{x})\,ds,\ I_3 = \underset{p\in P}{Ave}\left(d(p,\Gamma)\right),\ I_4 = \underset{p\in P_1}{Ave}\left(d(p,\Gamma)\right), \tag{7}$$

where Γ is the surface, P is the point set composed by all the sampled boundary points, P_1 denotes its subset composed by the points with high confidence level, Ave stands for the average operator, and the point-to-surface distance is calculated as:

$$d(p,\Gamma) = \min_{p'\in\Gamma} d(p,p'), \tag{8}$$

where $d(p,p')$ is the Euclidean distance between the two points.

Table 1 Comparisons among the surfaces built with different distance weights using the four measures defined in Eq. (7)

ω	I_1 (mm)	I_2 (mm)	I_3 (mm)	I_4 (mm)
0	0.87	1.31	0.67	0.76
0.2	0.89	1.24	0.59	0.63
0.4	0.95	1.17	0.62	0.54
0.6	0.97	1.14	0.72	0.57
0.8	0.98	1.12	0.70	0.48

I_1 and I_2 are two measures defined in the proposed energy functional that calculate the distances of the surface to the sampled boundary points and to the points with high confidence level, which can indicate the overall approaching of the surface segments to the boundaries. I_3 is the average distance of the sampled boundary points to the built surface, and I_4 is the average distance of the points with high confidence level to the surface; these two measures show how close the boundary points are to the local surface segment. Hence, the four indexes can indicate different aspects of the built surfaces, and their values for the four surfaces in Figure 4 are indicated in Table 1. From Table 1, one can realize that when ω increases, the value of I_1 increases and I_2 decreases, which satisfies the tendency defined in the energy functional. However, the changes of I_3 and I_4 does not have an explicit trend, because the two measures can be influenced considerably by the local changes of surface; for example, when ω increases from 0.6 to 0.8 the upper right sides of the bladder extend further, and both measures decreased. Based on the appearances of these surfaces and the four distance measures, the surface built with ω = 0.8 was considered as a proper model; furthermore, Figure 5 shows its differences to the two surfaces built from the axial and sagittal view planes, respectively. One can confirm that the surface built from the multi-view planes has more geometric changes that cannot be captured on a single view; for example, in Figure 5(a) the concave region caused by the uterus at the upper side of the bladder can be clearly identified in the surfaces built from the sagittal and multi-view planes, while this region is much tenderly presented in the surface built from the axial view because the changes cannot be captured clearly due to gaps between the axial planes. Based on the similar reason, in Figure 5(b) the horizontal changes on the surface can be better seen on the surfaces built from the axial and multi-view planes than from the sagittal planes. Table 2 presents the surface area and

the volume of the three surfaces built to show their differences and influences to the quantitative analysis of the urinary bladder.

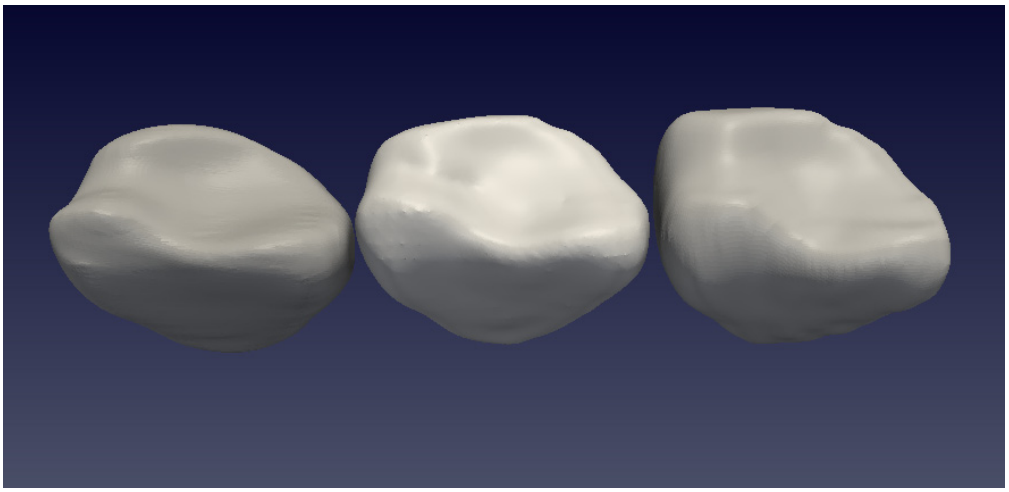

(a)

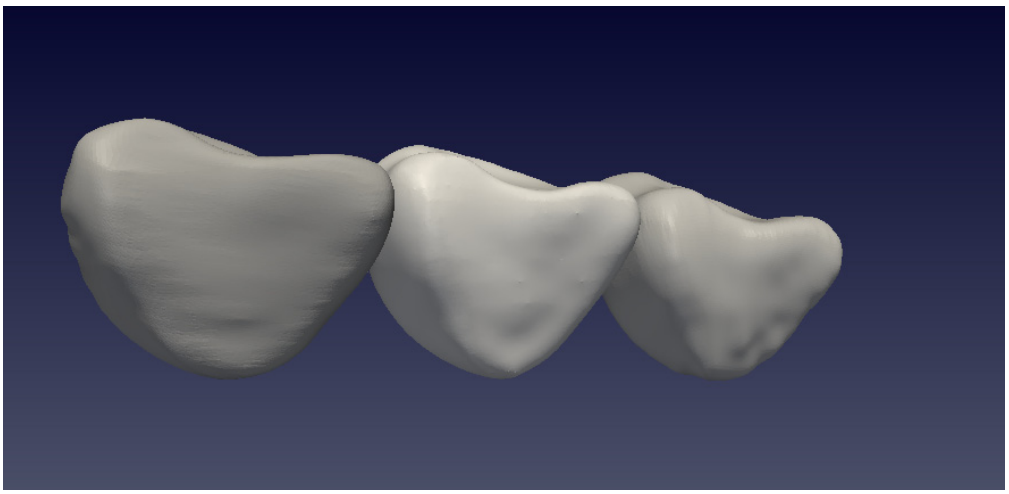

(b)

Figure 5: A comparison between the surfaces built from the multiple views (middle one with $\omega = 0.8$) and the ones from the axial (on the right) and sagittal views (on the left): (a) from the upper sides; (b) from the lateral sides.

Table 2 Volumes and surface areas of the surfaces built from multiple views and from the axial and sagittal views. (S - Surface built from multi-view planes, S_1 - Surface built from axial planes, S_2 - surface built from sagittal planes.)

	Volume (cm^3)	Area (cm^2)
S	225.11	208.94
S_1	245.60	217.98
S_2	210.24	201.42

5. Conclusion

The urinary bladder can be visualized from different views in an image series; information from multiple views can considerably improve the reliabilities of 3D

reconstruction. The algorithm proposed combines the multi-view information and provides a flexible and accurate method to build the 3D bladder surface model. The cross-sectional boundaries of the bladder are evaluated based on their reliabilities; and their influences to reconstruction are weighted according to the confidence levels. The distances of the surface to the positions defined by the boundaries with high confidence levels are added to the moving equation so that the reconstructed surface approaches to the more reliable positions when there are discrepancies. As such, the confusions caused by the inaccurate segmentation from multi-view imaging planes are naturally handled; the bladder surface is obtained through surface evolution based on its weighted distances to the cross-sectional boundaries under the smoothness constrain. Compared with the ones built from a single view plane, the surface built from multiple views contains more geometric details and changes.

The level set method is used for tracking the surface evolution. The procedures of the proposed algorithm are illustrated using a MR image series; the parameters in the algorithm are discussed and the variations of the reconstructed bladder surfaces with different distance weights are verified both qualitatively and quantitatively. The distance weights ω_i can influence the appearance of the bladder surface and need to be defined properly, especially when the boundary points with high confidence levels have uneven spatial distributions; otherwise, the built surface may become incomplete due to the missing information from the points with low confidence levels. In the procedures of the algorithm, the assignment of confidence levels requires manual interventions, and the distance weights need to be defined appropriately; the two aspects make the algorithm less automatic and these are the future work to be focused.

Acknowledgments

This work was partially done in the scope of the projects “Methodologies to Analyze Organs from Complex Medical Images – Applications to Female Pelvic Cavity”, “Aberrant Crypt Foci and Human Colorectal Polyps: mathematical modeling and endoscopic image processing” and “Cardiovascular Imaging Modeling and Simulation - SIMCARD”, with references PTDC/EEA-CRO/103320/2008, UTAustin/MAT/0009/2008 and UTAustin/CA/0047/2008, respectively, financially supported by Fundação para a Ciência e a Tecnologia (FCT) in Portugal.

The first author would like to thank FCT for his PhD grant with reference SFRH/BD/43768/2008.

Conflict of interest

The authors report no conflicts of interest.

References

[1] Stewart WF, Van Rooyen JB, Cundiff GW, Abrams P, Herzog AR, Corey R, Hunt TL, Wein AJ. 2003. Prevalence and burden of overactive bladder in the United States. World J Urol. 20(6):327-336.

[2] Anger JT, Saigal CS, Litwin MS. 2006. The prevalence of urinary incontinence among community dwelling adult women: results from the national health and nutrition examination survey. J Urology. 175(2):601-604.

[3] Barentsz JO, Jager GJ, Witjes JA, Ruijs JHJ. 1996. Primary staging of urinary bladder carcinoma: the role of MRI and a comparison with CT. Eur Radiol. 6(2):129-133.

[4] Lammle M, Beer A, Settles M, Hannig C, Schwaibold H, Drews C. 2002. Reliability of MR imaging-based virtual cystoscopy in the diagnosis of cancer of the urinary bladder. Am J Roentgenol. 178(6):1483-1488.

[5] Jaume S, Ferrant M, Macq B, Hoyte L, Fielding JR, Schreyer A, Kikinis R, Warfield SK. 2003. Tumor detection in the bladder wall with a measurement of abnormal thickness in CT scans. IEEE T Bio-med Eng. 50(3):383-390.

[6] Paramasivam S, Proietto A, Puvaneswary M. 2006. Pelvic anatomy and MRI. Best Pract Res Cl Ob. 20(1):3-22.

[7] Dimopoulos J, Schirl G, Baldinger A, Helbich TH, Pötter R. 2009. MRI assessment of cervical cancer for adaptive radiotherapy. Strahlenther Onkol. 185(5):282-287.

[8] Caruso G, Salvaggio G, Campisi A, Melloni D, Midiri M, Bertolotto M, Lagalla R. 2010. Bladder tumor staging: comparison of contrast-enhanced and gray-scale ultrasound. Am J Roentgenol. 194(1):151-156.

[9] Osher S, Sethian JA. 1988. Fronts propagating with curvature-dependent speed: algorithms based on Hamilton-Jacobi formulations. J Comput Phys. 79(1):12-49.

[10] Lorensen WE, Cline HE. Marching cubes: a high resolution 3D surface construction algorithm. Proceedings of the 14th annual conference on computer graphics and interactive techniques, 1987.

[11] Costa MJ, Delingette H, Novellas S, Ayache N. Automatic segmentation of bladder and prostate using coupled 3D deformable models, Proceedings of the medical image computing and computer-assisted intervention, 2007.

[12] Duan C, Liang Z, Bao S, Zhu H, Wang S, Zhang G, Chen JJ, Lu H. 2010. A coupled level set framework for bladder wall segmentation with application to MR cystography. IEEE T Med Imaging. 29(3):903-915.

[13] Ma Z, Jorge RNM, Mascarenhas T, Tavares JMRS. 2011. Novel approach to segment the inner and outer boundaries of the bladder wall in T2-weighted magnetic resonance images. Ann Biomed Eng. 39(8):2287-2297.

[14] Cheng D, Tempany CMC. 1998. MR imaging of the prostate and bladder. Semin Ultrasound CT. 19(1):67-89.

[15] Zhao HK, Osher S, Fedkiw R. Fast surface reconstruction using the level set method. Proceedings of the 1st IEEE workshop on variational and level set methods in computer vision, 2001.